2015

A computational framework for elliptic inverse problems with uncertain boundary conditions

BOSTON UNIVERSITY

COLLEGE OF ENGINEERING

Dissertation

A COMPUTATIONAL FRAMEWORK FOR ELLIPTIC INVERSE PROBLEMS WITH UNCERTAIN BOUNDARY CONDITIONS

by

DANIEL THOMAS SEIDL

B.S., University of Rochester, 2010
M.S., Boston University, 2012

Submitted in partial fulfillment of the

requirements for the degree of

Doctor of Philosophy

2015

Approved by

First Reader

Paul E. Barbone, Ph.D.
Professor of Mechanical Engineering

Second Reader

Assad A. Oberai, Ph.D.
Professor of Mechanical, Aerospace, and Nuclear Engineering
Rensselaer Polytechnic Institute

Third Reader

Harold S. Park, Ph.D.
Associate Professor of Mechanical Engineering

Fourth Reader

Emily M. Ryan, Ph.D.
Assistant Professor of Mechanical Engineering

Acknowledgments

The completion of this thesis marks the end of my time in Boston. I have often said to friends and family that my decision to attend BU was the best one I've ever made. I would like to thank some of those who helped me learn, laugh, and grow during this challenging and exciting period of my life.

First, my advisor Paul Barbone. He is one of the most patient, kind, and thoughtful people I've had the pleasure of knowing. I feel that our time together has made me not only a better engineer, but also a better person. Thank you Paul!

I would like to thank Assad Oberai for being my skype/email advisor. I was often amazed by how fast he would understand my problems and be able to offer well-reasoned potential solutions.

I am grateful to Harold Park and Emily Ryan for agreeing to serve on my thesis defense committee. Thank you both for your patience with the slow rate at which I finished the thesis.

I need to thank Lekan Babaniyi, my academic brother, for being a sounding board for ideas/listening to me rant, and serving as a much-needed voice of reason. Good luck with finishing the rest of your thesis. I am sure it will be great.

A few more past and present BMI group members deserve thanks. Sanjay Yengul, I can recall many long, interesting discussions with you that often started with a (seemingly) simple question. Also, thank you for constantly pushing for group lunches. They were fun. Brian Harvey, thank you for teaching me the ins-and-outs of displacement estimation and for finding so many of my bugs. I am forever in debt to Jean-Francois Dord for getting me up and running with the inversion code, providing his input file makers, and showing me all sorts of Linux tricks.

I must thank two professors from my undergraduate days. Laurel Carney gave me the opportunity to work in her research lab which lead to the realization that I needed

to abandon the idea that I would ever be a physician and accept that I was made to solve math problems on computers. David Blackstock taught a very memorable acoustics course during the summer between my junior and senior year, and gave me advice on applying to graduate schools that ultimately lead me to BU.

Finally, this thesis and everything leading up to it would not have been been possible without the love of my parents. Dad, thank you giving me the freedom to make my own mistakes and triumphs, and for always being there for me. Mom, I miss you and your enthusiasm for life. Thank you for encouraging me to use my imagination.

A COMPUTATIONAL FRAMEWORK FOR ELLIPTIC INVERSE PROBLEMS WITH UNCERTAIN BOUNDARY CONDITIONS

DANIEL THOMAS SEIDL

Boston University, College of Engineering, 2015

Major Professor: Paul E. Barbone, Ph.D.
Professor of Mechanical Engineering

ABSTRACT

This project concerns the computational solution of inverse problems formulated as partial differential equation (PDE)-constrained optimization problems with interior data. The areas addressed are twofold.

First, we present a novel software architecture designed to solve inverse problems constrained by an elliptic system of PDEs. These generally require the solution of forward and adjoint problems, evaluation of the objective function, and computation of its gradient, all of which are approximated numerically using finite elements. The creation of specialized "layered" elements to perform these tasks leads to a modular software structure that improves code maintainability and promotes functional interoperability between different software components.

Second, we address issues related to forward model definition in the presence of boundary condition (BC) uncertainty. We propose two variational formulations to accommodate that uncertainty: (a) a Bayesian formulation that assumes Gaussian measurement noise and a minimum strain energy prior, and (b) a Lagrangian formulation that is completely free of displacement and traction BCs.

This work is motivated by applications in the field of biomechanical imaging, where the mechanical properties within soft tissues are inferred from observations of tissue motion. In this context, the constraint PDE is well accepted, but considerable uncertainty exists in the BCs. The approaches developed here are demonstrated on a variety of applications, including simulated and experimental data. We present modulus reconstructions of individual cells, tissue-mimicking phantoms, and breast tumors.

Contents

List of Tables

List of Figures

List of Abbreviations

1D	.....	One Dimensional
2D	.....	Two Dimensional
3D	.....	Three Dimensional
AFM	.....	Atomic Force Microscopy
BFGS	.....	Broyden-Fletcher-Goldfarb-Shanno Method
BC	.....	Boundary Condition
BMI	.....	Biomechanical Imaging
BVP	.....	Boundary Value Problem
CASE	.....	Coupled Adjoint-State Equation
DOFS	.....	Degrees of Freedom
FEM	.....	Finite Element Method
GLS	.....	Galerkin Least Squares
FA	.....	Fibroadenoma
IDC	.....	Invasive Ductal Carcinoma
LHS	.....	Left Hand Side
MRI	.....	Magnetic Resonance Imaging
PDE	.....	Partial Differential Equation
PDF	.....	Probability Density Function
PDMS	.....	Polydimethylsiloxane
RF	.....	Radio Frequency
RHS	.....	Right Hand Side
SNR	.....	Signal to Noise Ratio
TV	.....	Total Variation
US	.....	Ultrasound
W.R.T.	.....	With Respect To

Nomenclature

$\boldsymbol{\sigma}$	Cauchy stress tensor
$\boldsymbol{\epsilon}$	Linear strain tensor
E	Young's modulus
μ	Shear modulus
$\boldsymbol{u}$	Displacement
$\boldsymbol{u}^m$	Measured displacement
p	Pressure
$\boldsymbol{w}$	Lagrange multiplier for the equilibrium constraint
q	Lagrange multiplier for the incompressibility constraint
Ω	Domain
Γ	Boundary
π	Objective function or probability density function
π^f	Constraint equation functional
$\mathcal{L}$	Lagrangian
h	Mesh parameter
α	Regularization constant
β	Total variation offset constant
$\boldsymbol{b}$	Body force
$\boldsymbol{t}$	Traction vector
$\boldsymbol{C}$	Covariance operator
$\boldsymbol{K}$	Spring tensor
$\boldsymbol{A}$	Plane stress strain operator
$\boldsymbol{n}$	Outward unit normal
$\boldsymbol{I}$	Identity tensor
∇^s	Symmetric gradient
$\boldsymbol{T}$, $\boldsymbol{D}$, $\boldsymbol{F}$	Symmetric weighting tensors

Chapter 1

Introduction and Background

1.1 Motivation

Biomechanical imaging (BMI) is used to visualize the mechanical properties of living structures. Physicians routinely use palpation to diagnose and characterize the health state of various tissues. BMI is an extension and quantitative refinement of this idea capable of reaching regions of the body and length scales that are impossible to touch, as well as determining mechanical properties other than linear elastic modulus.

The ingredients necessary for producing a biomechanical image are a measurement of tissue motion (displacement), a mechanical model of the tissue, and a means of inferring the parameters in the model from the observed tissue deformation. The parameter distribution may then be displayed as a two or three dimensional image.

A key component of BMI is the solution of an inverse boundary value problem. In such a problem, the effect (displacement) is used to determine the cause (the mechanical model parameters). Not surprisingly, a forward problem is one where the cause determines the effect. Forward problems are "well-posed", meaning that they satisfy Hadamard's conditions: a solution exists, the solution is unique, and small discrepancies in the input problem data have proportionate effects on error in the solution (Hadamard, 1902). Inverse problems are often deemed to be "ill-posed" as they violate some or all of these conditions. The introduction of additional assumptions not present in the forward problem is required to render a well-posed problem. Frequently, inverse problems can be thought of as partial differential equations where

the coefficients in the equation are the unknowns.

BMI has its roots in strain imaging, a technology invented over twenty years ago (Ophir et al., 1991). In its original form, a strain image or "elastogram" is acquired by quantifying tissue motion resulting from a quasi-static compression imposed through an ultrasound (US) transducer. Displacement is estimated by comparing an US image taken before deformation to another acquired afterwards.

B-mode US images are essentially the envelopes of a series of A-lines. Each A-line is a RF voltage signal of the echoes recorded from locations along the path of ultrasound pulse propagation. Figure (1·1) depicts an A-line before and after an applied compression. The peak of the cross-correlation of a segment of an undeformed A-line with its homologous deformed partner gives an estimate of how much that segment moved. Performing this cross-correlation for many segments in each A-line yields a two-dimensional image of tissue motion.

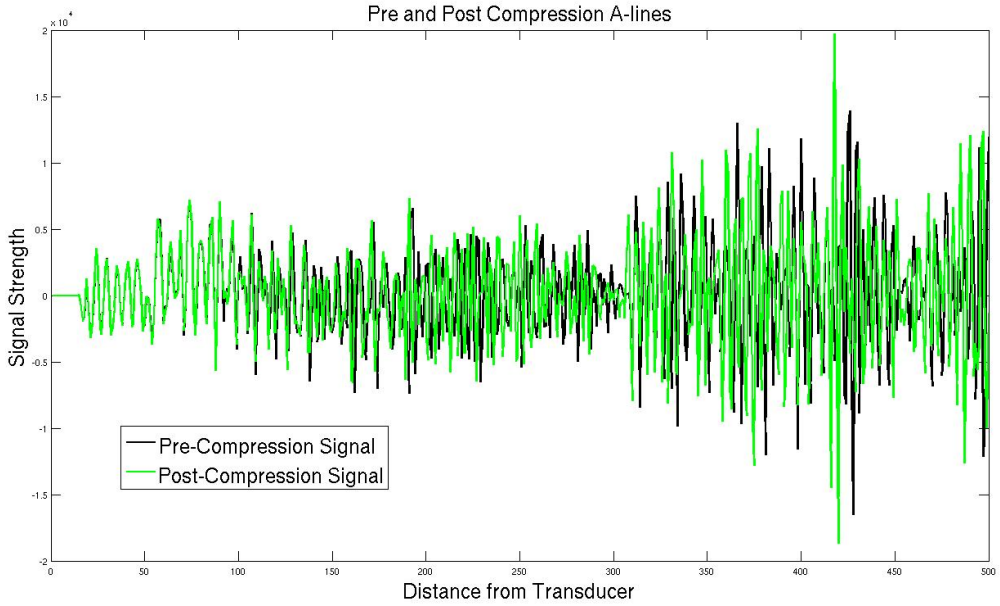

Figure 1·1: Deformation causes sections of the A-line to move non-uniformly

In current clinical practice (Barr, 2015), the tissue elastic modulus distribution is inferred from a strain image. This inference is based on the assuming a uniform, uniaxial stress field

$$\sigma_{ij} = 0, ij \neq yy \tag{1.1}$$

$$\sigma_{yy} = \sigma_0 = \text{constant} \tag{1.2}$$

$$\sigma_{yy} = E\epsilon_{yy} \Longrightarrow \tag{1.3}$$

$$E = \frac{\sigma_0}{\epsilon_{yy}} \tag{1.4}$$

Further,

$$\epsilon_{yy} = \frac{\partial u_y}{\partial y} \approx \frac{\Delta u_y}{\Delta L_y} \tag{1.5}$$

Thus, measuring u_y everywhere and assuming σ_{yy} is constant allows one to obtain an approximation of E. Here y is the coordinate in the "axial" direction, which is defined to be the direction of ultrasound pulse propagation.

A primary application to date of strain imaging has been detection and diagnosis of breast tumors in concert with B-mode US imaging, as they often can be clearly seen in the elastogram, the size and shape of which can sometimes relay useful information to the physician (Burnside et al., 2007)(Barr et al., 2012).

The assumptions of uniform stress and a one dimensional relationship between stress and strain are violated in complex three dimensional tissues. As a result strain images often contain artifacts that can obscure their interpretation, as shown in Figure (1·2). Their reproducibility (operator dependence) is also an issue (Barr et al., 2012), as different amounts of applied stress produce different images. These problems have

slowed clinical adoption of strain imaging and limit its ultimate clinical potential.

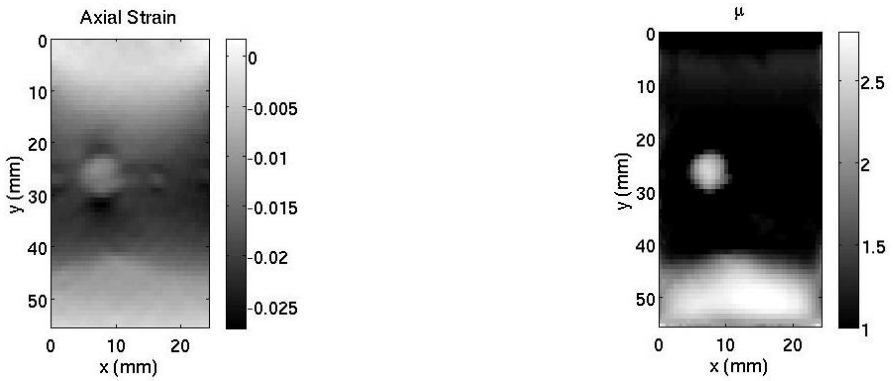

(a) (b)

Figure 1·2: (a) Axial strain, (b) Reconstructed modulus (Richards, 2007)

Two and three dimensional constitutive models are used in BMI, and as a result the inverse problem is more difficult to solve than the one posed in strain imaging. The extra work involved in using more advanced mechanical models yields several benefits, however, as BMI is capable of 1) producing images of elastic modulus that are superior to those obtained by strain imaging and 2) quantifying mechanical properties other than elastic modulus, such as viscosity, nonlinearity (Oberai et al., 2009)(Goenezen et al., 2011), anisotropy (Shore et al., 2011), and porosity (Berry et al., 2006) (which may contain more interesting information about the tissue than the elastic modulus.)

Direct (Albocher et al., 2009) and iterative (Oberai et al., 2004) computational methods for solving the BMI inverse problem exist. While direct methods take less time to produce a solution, they are less capable of dealing with noisy and incomplete data than iterative methods. In the context of US BMI, only the axial component of the measured displacement field is considered reliable, so the iterative approach is usually taken.

1.2 Iterative Inversion

In the iterative approach the inverse problem is formulated as an optimization problem constrained to satisfy the elasticity equations. The objective function consists of a displacement data matching piece $\mathcal{D}$ and a regularization term $\mathcal{R}$.

$$\pi[\mu(\boldsymbol{x}))] = \mathcal{D}[\boldsymbol{u}(\mu(\boldsymbol{x})) - \boldsymbol{u}^m] + \alpha\mathcal{R}[\mu(\boldsymbol{x})] \tag{1.6}$$

Here $\mu(\boldsymbol{x})$ represents the mechanical property of interest, usually the shear modulus. The data match term is a function of the mismatch between the measured displacement field, $\boldsymbol{u}^m$, and predicted displacement field, $\boldsymbol{u}$. The regularization term imposes an additional assumption(s) about the smoothness of the material parameters, and helps overcome the ill-posedness of the inverse problem. The constant α controls the regularization's contribution to the solution. Specific forms for $\mathcal{D}$ and $\mathcal{R}$ vary from application to application, and examples will be given later in the document. The implicit relationship between $\boldsymbol{u}$ and μ is captured in a mathematical model of the physical experiment, which can be formally expressed as the weak form of the governing elliptic boundary value problem:

$$\begin{aligned}
\mathcal{A}(\boldsymbol{w}, \boldsymbol{u}; \mu) &= l(\boldsymbol{w}) \;\forall\; \boldsymbol{w} \in \mathcal{V} && (1.7)\\
\boldsymbol{u} \in \mathcal{S} &\equiv \{\boldsymbol{u} \mid u_i \in H^1(\Omega), u_i = g_i \text{ on } \Gamma_u\} && (1.8)\\
\boldsymbol{w} \in \mathcal{V} &\equiv \{\boldsymbol{w} \mid w_i \in H^1(\Omega), w_i = 0 \text{ on } \Gamma_u\} && (1.9)\\
\mu \in \mathcal{M} &\equiv L^\infty(\Omega) && (1.10)
\end{aligned}$$

Iterative inversion begins with an initial guess of the material parameter distribution $\mu_0(\boldsymbol{x})$. In order to evaluate the value of the objective function for this choice of parameter, the displacement field $\boldsymbol{u}(\boldsymbol{x})$ resulting from these parameters is computed

by discretizing (1.7) with finite elements and solving the resultant system of equations using Newton's method. An optimization algorithm is used to find an update to $\mu(\boldsymbol{x})$ that will reduce the value of the objective function (1.6). Figure (1·3) provides a flowchart representation of this process.

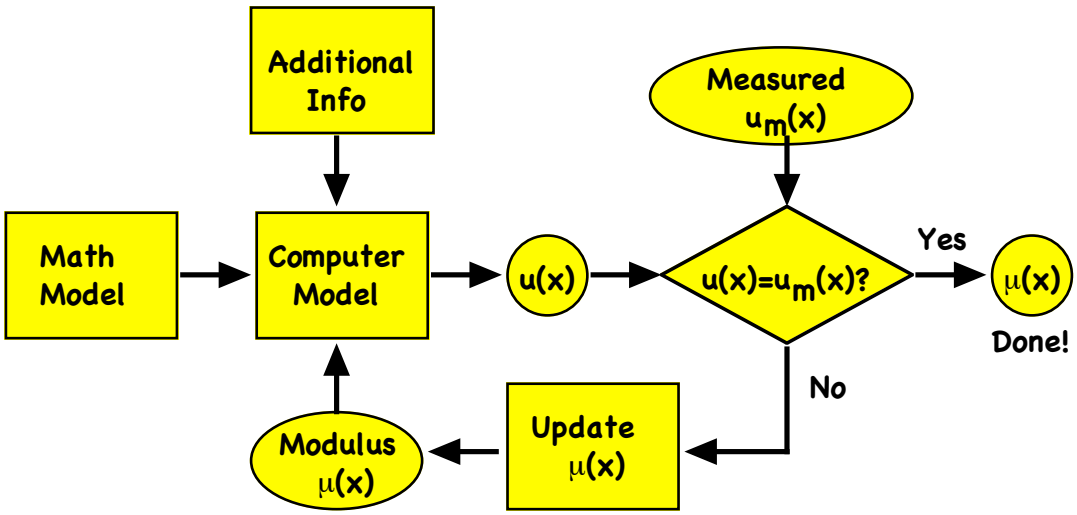

Figure 1·3: Iterative inversion flowchart

1.2.1 Optimization

One way in which optimization algorithms can be classified is by the amount of knowledge of the objective function and its derivatives they require. For example, brute force search, evolutionary algorithms, and simulated annealing require only evaluations of the objective function. Gradient methods, such as steepest descent and quasi-Newton methods, need both the value of the function and its gradient at each iteration. Finally, Newton's method requires evaluation of the function, its gradient, and its Hessian.

A straightforward approach to obtaining the gradient and Hessian is to use a finite difference approximation. If there are N discrete unknowns representing the discretized parameter μ, then finite difference computation of the gradient requires

N forward problem executions (beyond the first), while determination of the Hessian takes $O(N^2)$ forward solves (Nocedal and Wright, 2006). In the applications considered here, N is often between $10^2 - 10^6$, making the use of the finite difference approximation computationally intensive w.r.t. gradient methods and rendering the use of Newton's method intractable. Generally, Newton's method will converge in fewer iterations than a gradient method on a given problem, which in turn will converge in fewer iterations than a method that requires function evaluations only. There is, however, a technique known as the adjoint method (Oberai et al., 2003) that can be used to obtain the gradient with *one additional linear solve*. Adoption of this technique enables the use of gradient optimization methods on practical problems.

The derivation of the adjoint method often begins with the Lagrangian functional

$$\mathcal{L}[\boldsymbol{u}, \boldsymbol{w}, \mu] = \pi[\boldsymbol{u}, \mu] + \mathcal{A}(\boldsymbol{w}, \boldsymbol{u}; \mu) - l(\boldsymbol{w}) \ . \tag{1.11}$$

The function $\boldsymbol{w}$ here plays the role of a Lagrange multiplier. We take variations w.r.t. each of the Lagrangian's arguments. Here $\mathcal{V}$ is the space of variations containing $\delta\boldsymbol{u}$ and $\delta\boldsymbol{w}$, and the space $\mathcal{M}$ contains variations $\delta\mu$ of μ. Equations (1.12) and (1.13) are required to vanish for all variations in $\mathcal{V}$. The continuous equations (1.12) - (1.14) are discretized using the finite element method, but for simplicity of presentation we leave them as is in the following.

$$\begin{aligned}
D_{\boldsymbol{w}}\mathcal{L} \cdot \delta\boldsymbol{w} &= \mathcal{A}(\delta\boldsymbol{w}, \boldsymbol{u}; \mu) - l(\delta\boldsymbol{w}) \stackrel{set}{=} 0 \ \forall \ \delta\boldsymbol{w} \in \mathcal{V} && (1.12)\\
D_{\boldsymbol{u}}\mathcal{L} \cdot \delta\boldsymbol{u} &= D_{\boldsymbol{u}}\mathcal{D}[(\boldsymbol{u} - \boldsymbol{u}^m)] \cdot \delta\boldsymbol{u} + D_{\boldsymbol{u}}\mathcal{A}(\boldsymbol{w}, \boldsymbol{u}; \mu) \cdot \delta\boldsymbol{u} && (1.13)\\
&\stackrel{set}{=} 0 \ \forall \ \delta\boldsymbol{u} \in \mathcal{V} \\
D_{\mu}\mathcal{L} \cdot \delta\mu &= D_{\mu}\mathcal{A}(\boldsymbol{w}, \boldsymbol{u}; \mu) \cdot \delta\mu + \alpha D_{\mu}\mathcal{R}[\mu] \cdot \delta\mu && (1.14)
\end{aligned}$$

The adjoint approach to solving this coupled system of PDEs procedes as follows. Assume we know the value of the material parameter μ at the current iteration. In the first step, the state equation (1.12) is solved for $\boldsymbol{u}$. Note that on the constraint surface defined by (1.12), the objective function (1.6) and the Lagrangian (1.11) are equal.

Next the adjoint equation (1.13) is solved for $\boldsymbol{w}$. Application of equations (1.12) and (1.13) yields a simplified expression for the differential of the Lagrangian, which can be shown to be equal to the gradient of the objective function w.r.t. to the material parameter. (Strang, 2007).

$$\delta\mathcal{L} = \cancel{D_{\boldsymbol{u}}\mathcal{L}\cdot\delta\boldsymbol{u}} + \cancel{D_{\boldsymbol{w}}\mathcal{L}\cdot\delta\boldsymbol{w}} + D_{\mu}\mathcal{L}\cdot\delta\mu \tag{1.15}$$

$$D_{\mu}\pi\cdot\delta\mu = D_{\mu}\mathcal{L}\cdot\delta\mu \tag{1.16}$$

Thus, the control equation (1.14) provides a formula for the gradient of the objective function in the direction of an arbitrary test function $\delta\mu$.

A popular and efficient gradient-based optimization algorithm is the quasi-Newton method L-BFGS-B (Byrd et al., 1995). It stores (a limited number of) past values of updates to the objective function and gradient and uses them to construct an approximation to the inverse Hessian (which is never explicitly stored). This algorithm is also capable of enforcing box constraints L and U on μ. The use of such constraints is often necessary because some material parameters (e.g. shear modulus, thermal conductivity) are strictly positive quantities. The value of the objective function π and its gradient $D_{\mu}\pi$ are computed from the current $\boldsymbol{u}$, $\boldsymbol{w}$, and μ iterates and sent to the optimization routine, which returns an update to the material parameter. The process then begins again and continues until a convergence criterion is met, a specified number of iterations has passed, or the optimization algorithm is unable to find a suitable direction of descent. An example convergence plot is shown in Figure (1·4).

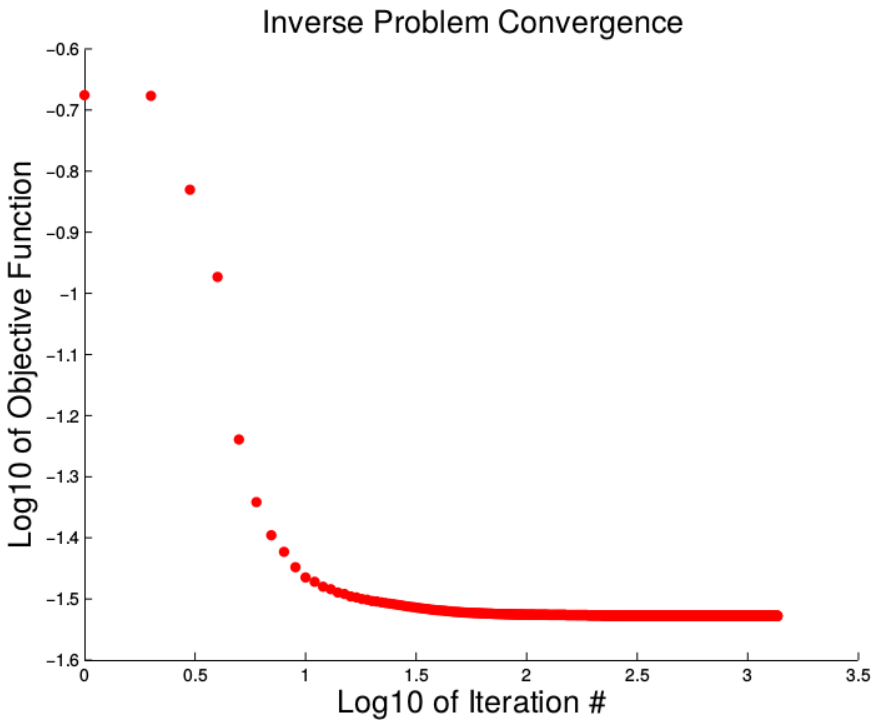

Figure 1·4: Objective function convergence example

1.3 Thesis Organization

In Chapter 2 we describe a modular software framework for the inversion algorithm discussed in this chapter. Chapters 3 and 4 focus on formulations of the constraint equation that do not require explicitly assumed BCs. Chapter 3 discusses a Bayesian formulation that assumes Gaussian measurement noise. In Chapter 4 we introduce a Lagrangian approach free of any displacement and traction BCs. Chapter 5 features applications of the products of Chapters 2-4 to simulated and experimental data. Chapter 6 contains some reflections on the findings in this thesis and a conclusion. Appendix A presents derivations of the linear incompressible elasticity models used throughout the document, and Appendix B contains simulated inverse problem examples that serve as test data for the formulations of Chapters 3 and 4.

Chapter 2

Software Framework

2.1 Introduction

This chapter describes the finite element method (FEM) implementation of the iterative inversion algorithm discussed in Chapter 1. It begins with an overview of the "layered" finite elements concept that defines the computational framework presented herein. Then a detailed description of the discrete subproblems that arise at each iteration is given and the definition and role of each element layer is specified.

2.2 Overview

The inverse problems under consideration in this thesis may all be characterized by the desire to find a stationary point of the following abstract Lagrangian:

$$\mathcal{L}[\boldsymbol{u}, \boldsymbol{w}, \mu] = \mathcal{D}[\boldsymbol{u} - \boldsymbol{u}^m] + \alpha \mathcal{R}[\mu] + \mathcal{A}(\boldsymbol{w}, \boldsymbol{u}; \mu) - l(\boldsymbol{w}) \tag{2.1}$$

In equation (2.1), the expressions $\mathcal{D}[\boldsymbol{u} - \boldsymbol{u}^m]$ and $\mathcal{R}[\mu]$ denote the data match and regularization pieces of the objective function, respectively. The $\mathcal{A}(\boldsymbol{w}, \boldsymbol{u}, \mu) - l(\boldsymbol{w})$ terms represents the weak form of a boundary value problem constraint. In this example we assume that $l(\boldsymbol{w}) = 0$.

To illustrate the layered FEM concept, we suppose that we wish to evaluate the Lagrangian for a specific choice of $(\boldsymbol{u}, \boldsymbol{w}, \mu)$.

2.2.1 Spatial Partitioning into Finite Elements

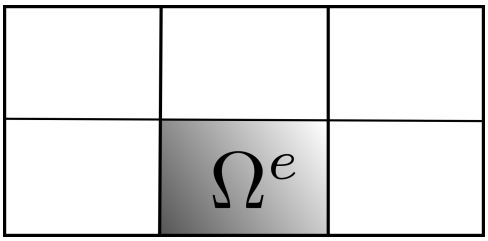

Figure 2·1: A 2D rectangular finite element

In the finite element method the domain Ω is divided into pieces (e.g. triangles, quadrangles, tetrahedra, hexahedra) Ω^e called finite elements. The superscript e is used to denote an elemental quantity. Each element has nodes located along its edges or vertices that are shared between neighboring elements. We define N_{el} to be the total number of elements, N_{no} the total number of nodes, and N_{sd} the number of spatial dimensions.

The continuous field variables (e.g. $\boldsymbol{u}$, $\boldsymbol{w}$, and μ) are approximated by linear combinations of a finite basis of interpolatory shape functions. A shape function N_A has the property of being equal to one at node A and zero at all other nodes. Given a field's values at the nodes, the shape functions can be used to interpolate the function over Ω, as shown in Figure (2·2).

$$\boldsymbol{w} \approx \boldsymbol{w}^h = \sum_{A=1}^{N_{no}} \sum_{i=1}^{N_{sd}} w_i^A N_A \hat{\boldsymbol{e}}_i \tag{2.2}$$

$$\boldsymbol{u} \approx \boldsymbol{u}^h = \sum_{B=1}^{N_{no}} \sum_{j=1}^{N_{sd}} u_j^B N_B \hat{\boldsymbol{e}}_j \tag{2.3}$$

$$\mu \approx \mu^h = \sum_{C=1}^{N_{no}} \mu^C N_C \tag{2.4}$$

The FEM approach to evaluating a the integral of a function f over the domain is to compute f^e (the specialization of f to Ω^e) over each element and sum, viz:

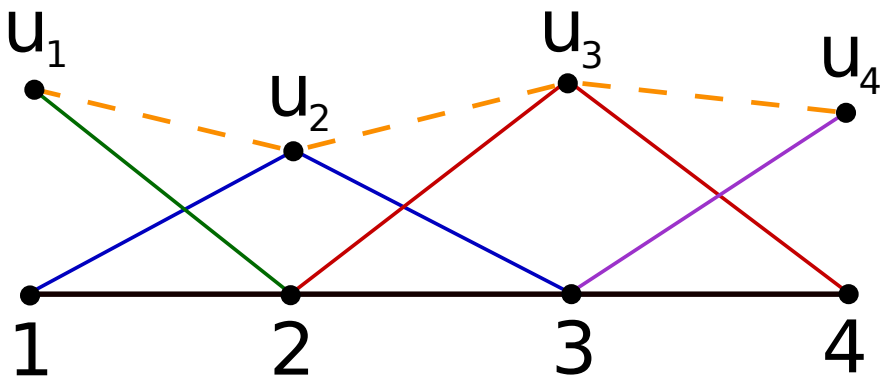

Figure 2·2: 1D example of u^h (dashed line) and its components in a piecewise linear basis

$$\int_{\Omega} f \; d\Omega = \sum_{e=1}^{N_{el}} \int_{\Omega^e} f^e \; d\Omega \tag{2.5}$$

Therefore, the Lagrangian can be evaluated according to equation (2.6).

$$\mathcal{L} = \sum_{e=1}^{N_{el}} \mathcal{L}^e[\boldsymbol{u}^h, \boldsymbol{w}^h, \mu^h] \tag{2.6}$$

A straightforward way to implement (2.6) is to write a subroutine/class (an "element routine") that will compute $\mathcal{L}^e$ given the geometrical information that defines Ω^e and $\boldsymbol{u}^h$, $\boldsymbol{w}^h$, and μ^h inside the element. This process is depicted in Figure (2·3).

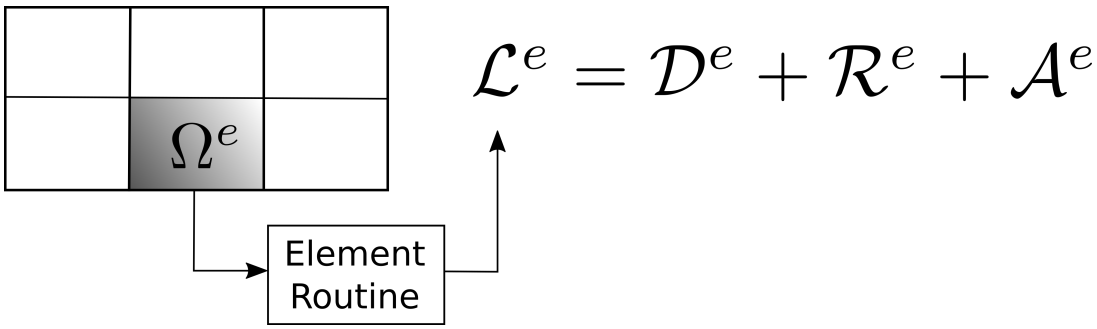

Figure 2·3: Straightforward approach to computing $\mathcal{L}^e$

2.2.2 Functional Partitioning into Layered Elements

An alternative approach to computing (2.6) is to create a separate software implementation for each operator that appears in (2.1). These elements share geometrical information that corresponds to the same region of space, but perform different functions as illustrated in Figure (2·4).

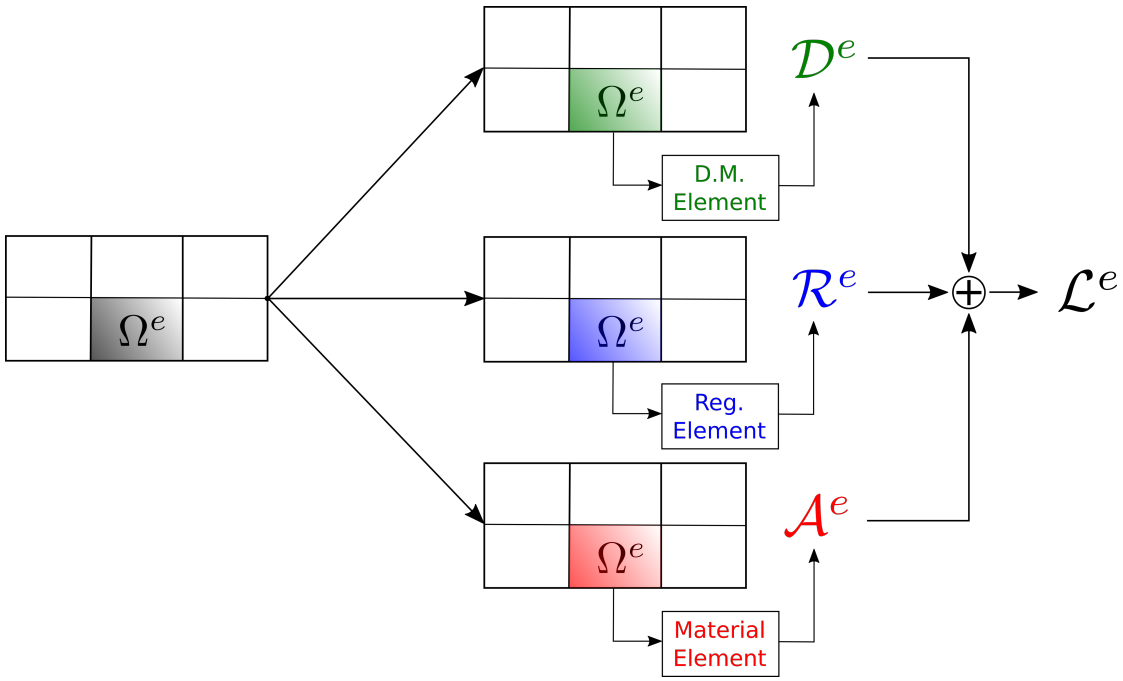

Figure 2·4: Layered approach to computing $\mathcal{L}^e$

The material model defined by $\mathcal{A}^e$ determines the type of inverse problem being solved (e.g. elasticity or heat conduction) and material parameter to be estimated (e.g. shear modulus or thermal conductivity). The data match $\mathcal{D}^e$ and regularization terms $\mathcal{R}^e$ are application dependent and their specific forms can vary even within a given class of inverse problems. Although zero in the example in this section, the remaining element layer l^e is associated with external forcing terms that may be present in the constraint equation. This partitioning scheme allows all material models to interface with all available data match, regularization, and forcing terms.

Thus, this modular software structure is more flexible than the straightforward "single element routine" approach in addition to being a more sustainable software design.

2.3 Discrete Subproblems

We now describe in detail the subproblems that arise at each iteration of the inverse algorithm. Each section begins with a problem statement and contains a derivation of the element-level quantities that pertain to each problem. We restate the function spaces for the field variables and their weights here for reference.

$$\boldsymbol{u} \in \mathcal{S} \equiv \{\boldsymbol{u} \mid u_i \in H^1(\Omega), u_i = g_i \text{ on } \Gamma_u\} \tag{2.7}$$

$$\boldsymbol{w}, \delta\boldsymbol{w}, \delta\boldsymbol{u} \in \mathcal{V} \equiv \{\boldsymbol{w} \mid w_i \in H^1(\Omega), w_i = 0 \text{ on } \Gamma_u\} \tag{2.8}$$

$$\mu, \delta\mu \in \mathcal{M} \equiv L^\infty(\Omega) \tag{2.9}$$

2.3.1 Step 1: Solve the State Equation

- Problem Statement: Given the current parameter distribution (e.g. shear modulus), compute the current state variable (e.g. predicted displacement).

$$\mathcal{A}(\delta\boldsymbol{w}, \boldsymbol{u}; \mu) = l(\delta\boldsymbol{w}) \;\forall\; \delta\boldsymbol{w} \in \mathcal{V} \tag{2.10}$$

The first (and most involved) step of the inversion algorithm is the solution of the discrete state equation (also called the constraint equation or forward problem) for $\boldsymbol{u}^h$.

Equation (2.10) states the continuous form of the problem. It is the weak form of the PDE constraint. The operator $\mathcal{A}(\cdot,\cdot)$ can in general be nonlinear its second argument, while the $l(\cdot)$ operator is linear.

Importantly, equation (2.10) holds when restricted to a finite dimensional subspace $\mathcal{V}^h \subset \mathcal{V}$.

$$\mathcal{A}(\delta \boldsymbol{w}^h, \boldsymbol{u}; \mu) = l(\delta \boldsymbol{w}^h) \ \forall \ \delta \boldsymbol{w}^h \in \mathcal{V}^h \tag{2.11}$$

Galerkin's method is to replace $\boldsymbol{u}$ and μ in (2.11) by finite dimensional approximations $\boldsymbol{u}^h \in \mathcal{S}^h$ and $\mu^h \in \mathcal{M}^h$ to obtain a discrete system of equations

$$\mathcal{A}(\delta \boldsymbol{w}^h, \boldsymbol{u}^h; \mu^h) = l(\delta \boldsymbol{w}^h) \ \forall \ \delta \boldsymbol{w}^h \in \mathcal{V}^h. \tag{2.12}$$

Generally, equation (2.12) represents a nonlinear system of equations. Newton's method can be used to solve a sequence of linear problems that converges to the solution of the nonlinear problem.

Application of Newton's method produces a new bilinear operator $a(\cdot, \cdot)$ defined by (2.14). Obviously, if $\mathcal{A}(\cdot, \cdot)$ is bilinear then it is equal to $a(\cdot, \cdot)$. Even in the linear case, however, a Newton approach is useful in the computational implementation because it handles the essential boundary conditions $\boldsymbol{g}^h$ in a convenient manner. While the increment $\Delta \boldsymbol{u}^h$ is zero for fixed dofs, $\boldsymbol{g}^h$ can be accounted for through the $\mathcal{A}$ term on the rhs of (2.14).

$$\begin{aligned} \mathcal{D}_{\boldsymbol{u}} \mathcal{A}(\delta \boldsymbol{w}^h, \boldsymbol{u}^h; \mu^h) \cdot \Delta \boldsymbol{u}^h &= \lim_{\alpha \to 0} \left(\frac{d}{d\alpha} \mathcal{A}(\delta \boldsymbol{w}^h, \boldsymbol{u}^h + \alpha \Delta \boldsymbol{u}^h; \mu^h) \right) \\ &= a(\delta \boldsymbol{w}^h, \Delta \boldsymbol{u}^h, ; \mu^h, \boldsymbol{u}^h) \end{aligned} \tag{2.13}$$

$$a(\delta \boldsymbol{w}^h, \Delta \boldsymbol{u}^h; \mu^h, \boldsymbol{u}^h) = l(\delta \boldsymbol{w}^h) - \mathcal{A}(\delta \boldsymbol{w}^h, \boldsymbol{u}^h; \mu^h) \ \forall \ \delta \boldsymbol{w}^h \in \mathcal{V}^h \tag{2.14}$$

The linear system (2.15) is the matrix representation of the global Newton equation (2.14). The symbol $[\cdot]$ denotes a matrix and $\{\cdot\}$ a vector. The operators in equation (2.14) are defined over Ω and possibly Γ as well. Recall that in FEM, integrals over Ω and Γ are broken into a sum of integrals over finite elements Ω^e and Γ^e. These elemental integrals (lowercase letters) are numerically integrated using Gauss

quadrature, and the resulting terms are assembled into their correct locations in the global linear system (uppercase letters). This computation is performed entirely using only the material and forcing elements.

$$
\begin{aligned}
[S]_{ij}^{AB}\{\Delta U\}_j^B &= \{F_{\text{ext}}\}_i^A - \{F_{\text{mat}}\}_i^A && (2.15)\\
[S]_{ij}^{AB} &= \mathbb{A}_{e=1}^{Nel}\left([s^e]_{ij}^{ab}\right) && (2.16)\\
\{F_{\text{ext}}\}_i^A &= \mathbb{A}_{e=1}^{Nel}\left(\{f_{\text{ext}}^e\}_i^a\right) && (2.17)\\
\{F_{\text{mat}}\}_i^A &= \mathbb{A}_{e=1}^{Nel}\left(\{f_{\text{mat}}^e\}_i^a\right) && (2.18)
\end{aligned}
$$

The matrix $[S]$ is called the tangent stiffness matrix. It represents a linearization of the stiffness matrix $[K](\boldsymbol{u})$ about the current displacement iterate. It is extremely sparse due to the compact support of the shape functions. Several efficient storage schemes (e.g. CSR, CSC) exist for such matrices. The rhs of (2.15) is known as the residual. The convergence of the nonlinear problem can be assessed by computing its norm.

When assembling (via the assembly operator $\mathbb{A}$) the global linear system, if a given entry is to be placed in a column/row of the global tangent stiffness matrix or a row of the global residual vector that corresponds to a fixed degree of freedom (dof) then it is ignored. Consequently, only dofs which are unknown are represented in the global system.

The Newton iterations must begin with an initial guess. Zero is usually used except for those dofs which are fixed in the definition of the function space. Thus computing the residual at the element level accounts for the essential BCs through the f_{mat}^e term.

2.3.2 Step 2: Evaluate the Objective Function

- Problem Statement: Given the current parameter distribution and state variable, compute the data match and regularization pieces of the objective function.

$$\pi = \mathcal{D}[(\boldsymbol{u} - \boldsymbol{u}^m)] + \alpha \mathcal{R}[\mu] \tag{2.19}$$

The finite element approximation of the objective function is computed by placing the solution of the state equation $\boldsymbol{u}^h$, the measured displacement field $(\boldsymbol{u}^m)^h$, and current modulus iterate μ^h into (2.19). The objective function is computed at the element level by the data match and regularization elements and accumulated.

$$\begin{aligned} \pi &= \mathcal{D}[\boldsymbol{u}^h - (\boldsymbol{u}^m)^h] + \alpha \mathcal{R}[\mu^h] \\ &= \sum_{e=1}^{Nel} \pi^e_{\text{data}} + \pi^e_{\text{reg}} \end{aligned} \tag{2.20}$$

If a point-evaluation optimization method is being used rather than a gradient approach then one skips to step 5. Otherwise, one procedes to the next step.

2.3.3 Step 3: Solve the Adjoint Equation

- Problem Statement: Given the current parameter distribution and state variable, solve for the Lagrange multiplier.

$$D_{\boldsymbol{u}} \mathcal{A}(\boldsymbol{w}, \delta \boldsymbol{u}; \mu) \cdot \delta \boldsymbol{u} = -D_{\boldsymbol{u}} \mathcal{D}[(\boldsymbol{u} - \boldsymbol{u}^m)] \cdot \delta \boldsymbol{u} \; \forall \; \delta \boldsymbol{u} \in \mathcal{V} \tag{2.21}$$

This problem is always linear as the operator $\mathcal{A}$ is linear in its first argument and is linearized about the solution of the discrete state equation.

As in the previous section, we focus our attention on a restriction of (2.21) to the subspace $\mathcal{V}^h \subset \mathcal{V}$,

$$\mathcal{D}_{\boldsymbol{u}}\mathcal{A}(\boldsymbol{w},\boldsymbol{u};\mu)\cdot\delta\boldsymbol{u}^h \;=\; -D_{\boldsymbol{u}}\mathcal{D}[(\boldsymbol{u}-(\boldsymbol{u}^m))]\cdot\delta\boldsymbol{u}^h\;\forall\;\delta\boldsymbol{u}^h\in\mathcal{V}^h. \tag{2.22}$$

We obtain the Galerkin approximation of adjoint equation by substituting $\boldsymbol{w}^h \in \mathcal{V}^h$, $\boldsymbol{u}^h \in \mathcal{S}^h$, and $\mu^h \in \mathcal{M}^h$ into (2.22) and recalling the directional derivative of a functional.

$$\begin{aligned}\mathcal{D}_{\boldsymbol{u}}\mathcal{A}(\boldsymbol{w}^h,\boldsymbol{u}^h;\mu^h)\cdot\delta\boldsymbol{u}^h &= \lim_{\alpha\to 0}\left(\frac{d}{d\alpha}\mathcal{A}(\boldsymbol{w}^h,\boldsymbol{u}^h+\alpha\delta\boldsymbol{u}^h;\mu^h)\right) \\ &= a(\boldsymbol{w}^h,\delta\boldsymbol{u}^h,\mu^h,\boldsymbol{u}^h)\end{aligned} \tag{2.23}$$

The matrix form of equation (2.24) is stated in (2.25). We take the transpose of both sides of (2.25) and observe that the transpose of the tangent stiffness matrix from the final Newton iteration of the state equation appears in (2.26).

$$a(\boldsymbol{w}^h,\delta\boldsymbol{u}^h;\mu^h,\boldsymbol{u}^h) \;=\; -D_{\boldsymbol{u}}\mathcal{D}[(\boldsymbol{u}^h-(\boldsymbol{u}^m)^h)]\cdot\delta\boldsymbol{u}^h\;\forall\;\delta\boldsymbol{u}^h\in\mathcal{V}^h \tag{2.24}$$

$$\{W\}_i^A\,[S]_{ij}^{AB} \;=\; \{F_{\text{data}}\}_j^B \tag{2.25}$$

$$\left([S]_{ij}^{AB}\right)^T\{W\}_j^B \;=\; \{F_{\text{data}}\}_i^A \tag{2.26}$$

$$\{F_{\text{data}}\}_i^A \;=\; \mathbb{A}_{e=1}^{Nel}\left(\{f_{\text{data}}^e\}_i^a\right) \tag{2.27}$$

Since the lhs of (2.26) has been computed previously, the only additional work required to build the linear system (besides transposing $[S]$ if it is not symmetric) is to form the rhs F_{data}. We note that the data match elements are responsible for computing this quantity.

2.3.4 Step 4: Evaluate the Gradient

- Problem Statement: Given the current parameter distribution, state variable, and Lagrange multiplier, compute the material and regularization contributions to the gradient.

$$D_\mu \pi = D_\mu \mathcal{A}(\boldsymbol{w}, \boldsymbol{u}; \mu) + \alpha D_\mu \mathcal{R}[\mu] \tag{2.28}$$

The discrete formula for the gradient is obtained by substituting the finite element functions $\boldsymbol{u}^h$, $\boldsymbol{w}^h$, and μ^h (all known at this point) into (2.28).

$$D_\mu \pi \cdot \delta\mu^h = D_\mu \mathcal{A}(\boldsymbol{w}^h, \boldsymbol{u}^h; \mu^h) \cdot \delta\mu^h + \alpha D_\mu \mathcal{R}[\mu^h] \cdot \delta\mu^h \tag{2.29}$$

Equation (2.29) can be written in vector form as

$$\{G\}_C \delta\mu^C = \{G_{\text{mat}}\}_C \delta\mu^C + \{G_{\text{reg}}\}_C \delta\mu^C. \tag{2.30}$$

The gradient is computed at the element level and assembled into a global vector.

$$\{G\}_C = \mathbb{A}_{e=1}^{N_{el}} \left(\{g^e_{\text{mat}}\}_c + \{g^e_{\text{reg}}\}_c \right) \tag{2.31}$$

This step requires contributions from the material and regularization elements.

2.3.5 Step 5: Material Parameter Update

An optimization algorithm is used to update the desired material property distribution, based on the objective function value, and possibly its gradient, and their histories. This calculation is independent of the method by which the objective function's value and its gradient are computed.

2.4 Finite Element Layers

There are four operators present in the inverse problem, and consequently there are four finite element layers:

- $\mathcal{A}(\cdot,\cdot) \rightarrow$ Material elements
- $l(\cdot) \rightarrow$ Forcing elements
- $\mathcal{D}[\cdot] \rightarrow$ Data match elements
- $\mathcal{R}[\cdot] \rightarrow$ Regularization elements

2.4.1 Material Elements

The material element contributes three terms to the discrete inverse problem.

- The tangent stiffness matrix $[s^e]$
- The Newton iteration rhs contribution $\{f^e_{\text{mat}}\}$ present in the state equation
- The material component of the gradient $\{g^e_{\text{mat}}\}$

The material element is part of the specification of the constraint equation. In the context of BMI it represents a mechanical model of the measured system, but more generally the material element provides information about the physical response of a material. Important considerations include the spatial dimension of the problem, kinds of field variables (displacements, pressures, stresses) that interact with the material, simplifying modeling assumptions (e.g. plane stress or strain), and constitutive model. A library of material elements allows for the solution of forward and inverse problems for a diverse array of modeling scenarios. Multiphysics problems could be approached using an appropriate combination of material elements.

2.4.1.1 Log Optimization

In BMI, the material property most commonly sought is the shear modulus $\mu(\boldsymbol{x})$. Alternatively, the problem can formulated in terms of the shear compliance $s(\boldsymbol{x})$, which is defined to be the reciprocal of μ. Tarantola argues convincingly that such problems should be constructed in terms of the log of either quantity (Tarantola, 2002). We introduce a new optimization variable ψ defined to be

$$\psi = \log(\frac{\mu}{\mu_{\text{ref}}}) \tag{2.32}$$

There are several benefits to formulating the problem in terms of ψ. First, the solution is not biased towards a stiffness or compliance interpretation. Second, in principle the inverse problem no longer requires box constraints as ψ can be positive or negative. In practice, although box constraints on ψ are not required they can nevertheless be useful to have. Finally, results obtained using this formulation tend to show more accurate inclusion to background contrast than those obtained using a conventional stiffness formulation.

Computational implementation of the ψ formulation is relatively straightforward. It can be accomplished by modifying existing material elements and replacing μ with ψ in the regularization terms. The parts of the material element that pertain to the state equation must be altered so that μ is computed according to equation (2.33). The material component of the gradient can be related to its μ derivative (already implemented in the material elements) using the chain rule as shown in (2.34).

$$\mu = \mu_{\text{ref}} \exp(\psi) \tag{2.33}$$

$$\frac{D}{D\psi} = \frac{D\mu}{D\psi}\frac{D}{D\mu} = \mu\frac{D}{D\mu} \tag{2.34}$$

2.4.2 Forcing Elements

Forcing elements drive the state equation in the absence of or in addition to Dirichlet BCs through the rhs vector $\{f^e_{\text{ext}}\}$.

The two types of continuous forcing elements are flux (per unit area) and body (per unit volume) forces. The physical interpretation of these is problem dependent. For example in elasticity, the flux force is a traction and a typical example of a body force would be that due to a gravitational field. In a heat conduction problem the analogous quantities are heat flux and heat source.

The discrete form of these forces can be obtained through a lumped or distributed representation. The decision to use one or the other is often related to how a measurement of the force was obtained or approximated.

In the case of distributed forces, the shape functions are used to determine elemental forms of the traction $\boldsymbol{t}$ and body force $\boldsymbol{b}$ vectors.

$$\{f^e_{\text{ext}}\}^a_i = \int_{\Gamma^e} t^d_i N_a N_d \; d\Gamma + \int_{\Omega^e} b^d_i N_a N_d \; d\Omega \tag{2.35}$$

Lumped forces are essentially distributed forces that have by some means been "integrated-out" such that the forcing vector is a sum of nodal contributions.

2.4.3 Data Match Elements

The data match element is responsible for computing two quantities:

- The data match piece of the objective function π^e_{data}
- The rhs of the adjoint problem $\{f^e_{\text{data}}\}$

The justification for the use of a given form of data match term can be explained by viewing the inverse problem as a statistical estimation problem. For example, the use of a weighted ($\boldsymbol{T}$ in equation (2.36) is a positive semi-definite weighting tensor) least

squares term data match term corresponds to the assumption that the measurement noise is distributed as a Gaussian random field with inverse covariance matrix $\boldsymbol{T}^T\boldsymbol{T}$.

$$\mathcal{D}[\boldsymbol{u}-\boldsymbol{u}^m] = \frac{1}{2}\int_\Omega \boldsymbol{T}(\boldsymbol{u}-\boldsymbol{u}^m)\cdot\boldsymbol{T}(\boldsymbol{u}-\boldsymbol{u}^m)\;d\Omega \tag{2.36}$$

$$D_{\boldsymbol{u}}\mathcal{D}[\boldsymbol{u}-\boldsymbol{u}^m]\cdot\delta\boldsymbol{u} = \int_\Omega \boldsymbol{T}^T\boldsymbol{T}(\boldsymbol{u}-\boldsymbol{u}^m)\cdot\delta\boldsymbol{u}\;d\Omega \tag{2.37}$$

$$\pi^e_{\text{data}} = \int_{\Omega^e} T^c_{ij}N_c(u^a_j-(u^m)^a_j)N_aT^d_{ik}N_d(u^b_k-(u^m)^b_k)N_b\;d\Omega \tag{2.38}$$

$$\{f^e_{\text{data}}\}^a_i = \int_{\Omega^e}(T_{ki}T_{kj})^dN_d(u^b_j-(u^m)^b_j)N_aN_b\;d\Omega \tag{2.39}$$

A data match term based on the L^1 norm is useful when the measurements contain a multitude of outliers, the presence of which is not consistent with an assumption of normally distributed noise. Such a term with equal weights can be associated with a Laplace distribution, but it is not clear what the distribution associated with a weighted L^1 term (as would be used in ultrasound BMI) is.

The continuous form of a weighted L^1 data match term is given below. It is more difficult to implement computationally because of its nonlinearity and the unboundedness of its derivative at points where $\boldsymbol{u}=\boldsymbol{u}^m$.

$$\pi_{\text{data}} = \int_\Omega |\boldsymbol{T}(\boldsymbol{u}-\boldsymbol{u}^m)|\;d\Omega \tag{2.40}$$

$$= \int_\Omega \sqrt{\boldsymbol{T}(\boldsymbol{u}-\boldsymbol{u}^m)\cdot\boldsymbol{T}(\boldsymbol{u}-\boldsymbol{u}^m)}\;d\Omega \tag{2.41}$$

$$D_{\boldsymbol{u}}\mathcal{D}[\boldsymbol{u}-\boldsymbol{u}^m]\cdot\delta\boldsymbol{u} = \int_\Omega \frac{\boldsymbol{T}^T\boldsymbol{T}(\boldsymbol{u}-\boldsymbol{u}^m)\cdot\delta\boldsymbol{u}}{\boldsymbol{T}(\boldsymbol{u}-\boldsymbol{u}^m)\cdot\boldsymbol{T}(\boldsymbol{u}-\boldsymbol{u}^m)}\;d\Omega \tag{2.42}$$

In some inverse problems measurements are available at only isolated points in the domain. A discrete objective function is useful in such cases. Equation (2.43) is an example of a least squares version of such a term.

$$\mathcal{D}[\boldsymbol{u} - \boldsymbol{u}^m] = \sum_{i=1}^{N} (\boldsymbol{u}_i - (\boldsymbol{u}^m)_i)^2 \tag{2.43}$$

2.4.4 Regularization Elements

The regularization element calculates the following two quantities:

- The regularization piece of the objective function π^e_{reg}
- The regularization component of the gradient $\{g^e_{\text{reg}}\}$

Regularization is added to ill-posed problems to enable the solution of a "nearby" well-posed problem. The regularization term represents the prior distribution in a Bayesian formulation. It smooths the solution of the inverse problem, prevents overfitting of the data, and "fills in gaps" where there is insufficient data to determine μ.

TV regularization biases the solution of the inverse problem towards piecewise-constant material property distributions. This type of solution is expected when looking for stiff tumors within a soft background, or for soft lipid-filled plaques in a stiffer background in cardiovascular imaging.

$$\mathcal{R}[\mu] = \alpha_{\text{TV}} \int_{\Omega} \sqrt{(\nabla\mu)^2 + \beta^2}\, d\Omega \tag{2.44}$$

$$\pi^e_{\text{reg}} = \alpha_{\text{TV}} \int_{\Omega^e} \sqrt{\mu^c N_{c,i} \mu^d N_{d,i} + \beta^2}\, d\Omega \tag{2.45}$$

$$\{g^e_{\text{reg}}\}_c = \alpha_{\text{TV}} \int_{\Omega^e} \frac{N_{c,j}\mu^d N_{d,j}}{\sqrt{\mu^a N_{a,i} \mu^b N_{b,i} + \beta^2}}\, d\Omega \tag{2.46}$$

The utilization of a regularization term based on the H^1 semi-norm is appropriate when the material parameter is expected to vary smoothly (e.g. is of a Gaussian or exponential functional form). This kind of regularization penalizes both local oscillations due to noise and jumps due to material property discontinuities.

$$\mathcal{R}[\mu] = \frac{\alpha_{H^1}}{2} \int_\Omega \nabla\mu \cdot \nabla\mu \; d\Omega \tag{2.47}$$

$$\pi^e_{\text{reg}} = \frac{\alpha_{H^1}}{2} \int_\Omega \mu^c N_{c,i} \mu^d N_{d,i} \; d\Omega \tag{2.48}$$

$$\{g^e_{\text{reg}}\}_c = \alpha_{H^1} \int_\Omega N_{c,i} \mu^d N_{d,i} \; d\Omega \tag{2.49}$$

Regularization based on a penalty of the L^2 norm of the solution is simple to implement and can produce reasonable results when used on relatively noise-free data. Material property fields with "small" L^2 norms can still be highly oscillatory, so solutions obtained using this type of regularization tend to be considerably less smooth than those obtained with H^1 semi-norm or TV terms.

$$\mathcal{R}[\mu] = \frac{\alpha_{L^2}}{2} \int_\Omega \mu^2 \; d\Omega \tag{2.50}$$

$$\pi^e_{\text{reg}} = \frac{\alpha_{L^2}}{2} \int_\Omega \mu^c N_c \mu^d N_d \; d\Omega \tag{2.51}$$

$$\{g^e_{\text{reg}}\}_c = \alpha_{L^2} \int_\Omega N_c \mu^d N_d \; d\Omega \tag{2.52}$$

The regularization element implemented in our inversion code uses a linear combination of TV, H^1 semi-norm, and L^2 regularizations. One can in principle use all of these forms of regularization simultaneously on an inverse problem, but determining the "right" regularization constant α can be difficult even when one form of

regularization is used.

We briefly discuss two strategies for determining α. In the "L-curve" method, the inverse problem is solved for several values of α and a log-log scatter plot of the size of the data match vs regularization pieces of the objective function is created. One then attempts to use the value of regularization that lies in the bend of the "L-curve", as this represents a point where the regularization and data match terms are appropriately balanced. Another method used to determine α is Morozov's discrepancy principle, where one uses a knowledge of the noise present in the measurements to choose α (Vogel, 2002).

In practice, the choice of which form(s) of regularization to use and how to determine their weights depends on expected features of the inverse problem solution and information/assumptions related to the measurement process. The strategies discussed above provide useful guidelines for finding α, but in many situations its determination often comes down to informed trial and error.

2.5 Discussion

In this chapter we introduced a software architecture for solving inverse problems based on operators that appear in the algorithm subproblems. We explained the concept of finite element layers and then described the purpose of each layer. This approach to solving the inverse problem was used to obtain all of the results in the rest of the document. Although this thesis is focused on the solution of elliptic inverse problems, a similar structure exists in other classes of PDE-constrained optimization problems. For example, variations of this framework could be applied to inverse problems where robin BCs or forcing terms are the parameters of interest.

Chapter 3

Spring Penalty Elements

3.1 Introduction

In this chapter we consider a reformulation of the elasticity constraint equation that contains a weighted least squares penalty on the mismatch between measured and predicted displacement fields. This approach is applied to simulated data, and the results are compared to those obtained with explicitly enforced assumed boundary conditions. We observe that the success of this formulation depends on appropriately choosing the weighting operator in the penalty term.

3.2 Motivation

3.2.1 Uncertain BCs

In elasticity BVPs one must prescribe some data (displacement (Dirichlet BC) or traction (Neumann BC)) at each point for each component on the boundary for the problem to be well-posed. One is free, for example, to fix a x component of displacement at a point and a y component of traction at that same point. The measured displacement field provides a potential source of Dirichlet boundary conditions for the forward problem. The uncertainty in the measured data field is sometimes high. Unfortunately, there is rarely a measurement of traction available.

As a result, there are essentially two options traditionally assumed for a BC: impose Dirichlet conditions using from the measured data, or assume some Neumann

BC based on *a priori* knowledge of the experimental conditions. The most common approach taken in US BMI is to apply the axial (the most accurate) component of displacement as a Dirichlet BC, and assume all other BCs to be homogeneous Neumann. The effectiveness of this approach varies depending on how well the mechanical model and measured data satisfy the experimental conditions implied by the BCs.

The alternative explored in this chapter offers a more flexible approach. Rather than rigidly assuming the BCs to be Dirchlet or homogeneous Neumann, the weights in the penalty term determine the degree to which a given boundary measurement is enforced. Ideally, these weights are determined by the statistics of the noise present in the measurements, so that well-characterized measurements are given more emphasis than poorly characterized ones.

We also describe a formulation where the penalty term acts over the domain rather than the boundary. Interestingly, the results from this formulation are of considerably poorer quality than those obtained using only information from boundary measurements, the reasons for which will be explained herein.

3.2.2 Constraining Rigid Body Motion

An additional application of this penalty approach arises in problems where the deformation is driven purely by tractions or body forces. In such problems the forward problem is unsolvable without the presence of information regarding the displacement field sufficient to constrain its rigid body component.

To motivate the importance of properly constraining rigid body motion, consider the following 1D example: a bar of length L with constant E and A and applied force P . The general solution of this problem (where b is a constant determined by the position at which the bar is fixed), along with the solutions for the scenarios depicted in Figure 3·1, are:

$$u(x) = \frac{PL}{EA}x + b = mx + b \tag{3.1}$$

$$u^a(x) = mx \tag{3.2}$$

$$u^b(x) = m(x-p) \tag{3.3}$$

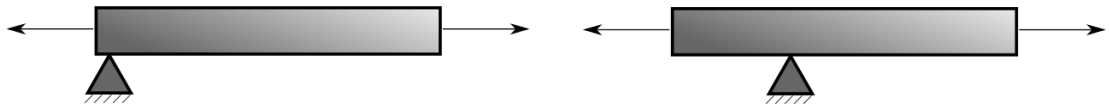

a) Fixed at $x = 0$ b) Fixed at $x = p$

Figure 3·1: Same loading, different computed displacement

Now assume that a displacement field $u^m(x)$ was measured in an experiment where the bar was constrained as depicted in Figure 3·1 b). Suppose P,L,E, and A are known exactly and the incorrect rigid body motion shown in Figure 3·1 a) is imposed when solving the forward problem. The data match norm $\|u - u^m\|^2$ will not be at a minimum. The optimization algorithm will subsequently change $E(x)$ even though it is correct! Thus, care must be taken to ensure that the rigid body component of displacement is the same for both the measured and predicted field.

3.3 Bayesian Formulation

We consider the forward problem as a Bayesian (point) estimation of a state given a noisy measurement, namely

$$\text{Given} \quad \boldsymbol{u}^m(\boldsymbol{x}) = \boldsymbol{u}_{\text{exact}}(\boldsymbol{x}) + \boldsymbol{n}(\boldsymbol{x}) \tag{3.4}$$

$$\text{with} \quad \boldsymbol{n} \sim N(0, \boldsymbol{C}) \tag{3.5}$$

$$\text{Find} \quad \boldsymbol{u}(\boldsymbol{x}) \text{ where } \nabla \cdot \boldsymbol{\sigma}(\boldsymbol{x}) + \boldsymbol{b}(\boldsymbol{x}) = \boldsymbol{0} \tag{3.6}$$

$$\text{and} \quad \mu(\boldsymbol{x}) = \text{known} \tag{3.7}$$

3.3.1 Boundary Springs Formulation

According to (3.5), the likelihood of the boundary values of the displacement field $\boldsymbol{u}$ is given by

$$\pi_{\text{data}} \propto \exp\left(-\frac{1}{2}\int_{\Gamma}(\boldsymbol{u}-\boldsymbol{u}^m)\cdot\boldsymbol{C}^{-1}(\boldsymbol{u}-\boldsymbol{u}^m)\ d\Gamma\right) \tag{3.8}$$

$$\propto \exp\left(-\frac{1}{2}||\boldsymbol{C}^{-\frac{1}{2}}(\boldsymbol{u}-\boldsymbol{u}^m)||^2_{\Gamma}\right) \tag{3.9}$$

Our prior assumption on $\boldsymbol{u}$ is that it is the displacement field in a heterogeneous, isotropic, linear elastic solid. As such, it tends to minimize the strain energy. That is, fields with lower strain energy are assumed to be much more likely than fields with higher strain energy. Therefore, we take a prior probability density function (PDF) on $\boldsymbol{u}$ of the form

$$\pi_{\text{prior}} \propto \exp\left(-||\boldsymbol{u}||^2_{\text{SE}}\right) \tag{3.10}$$

where

$$||\boldsymbol{u}||^2_{\text{SE}} = \frac{1}{2}\int_{\Omega}\boldsymbol{\sigma}(\boldsymbol{u}):\boldsymbol{\epsilon}(\boldsymbol{u})\ d\Omega - \int_{\Omega}\boldsymbol{b}\cdot\boldsymbol{u}\ d\Omega \tag{3.11}$$

The posterior PDF is, therefore,

$$\pi_{\text{post}} \propto \pi_{\text{data}} * \pi_{\text{prior}} \propto \exp\left(-\frac{1}{2}||\boldsymbol{u}||^2_{\text{SE}} - \frac{1}{2}||\boldsymbol{C}^{-\frac{1}{2}}(\boldsymbol{u}-\boldsymbol{u}^m)||^2_{\Gamma}\right) \tag{3.12}$$

We define $\pi^f[\boldsymbol{u}]$ to be $-\log(\pi_{\text{post}})$, and denote $\boldsymbol{C}^{-1}$ by $\boldsymbol{K}$. The data-match term now looks like the energy of springs located along Γ:

$$\pi^f[\boldsymbol{u}] = \underbrace{\frac{1}{2}\int_\Omega \boldsymbol{\sigma}(\boldsymbol{u}) : \boldsymbol{\epsilon}(\boldsymbol{u})\ d\Omega - \int_\Omega \boldsymbol{b}\cdot\boldsymbol{u}\ d\Omega}_{\text{strain-energy}} + \underbrace{\frac{1}{2}\int_\Gamma (\boldsymbol{u}-\boldsymbol{u}^m)\cdot\boldsymbol{K}(\boldsymbol{u}-\boldsymbol{u}^m)\ d\Gamma}_{\text{boundary spring penalty}} \quad (3.13)$$

The minimizer of (3.13) is the maximizer of (3.12), the M.A.P. (maximum *a posteriori*) estimate of the displacement field $\boldsymbol{u}$ given the boundary values of $\boldsymbol{u}^m$ and the symmetric spring tensor $\boldsymbol{K}$.

The entries of $\boldsymbol{K}$ control how much the functional increases if the predicted displacement $\boldsymbol{u}$ deviates from $\boldsymbol{u}^m$. As shown above, $\boldsymbol{K}$ may be interpreted as an inverse covariance operator acting on $\boldsymbol{u}-\boldsymbol{u}^m$ evaluated on the boundary. An appropriate $\boldsymbol{K}$ for use with US displacement data would have its eigenvector with the largest eigenvalue oriented along the direction of sound propagation, and considerably smaller eigenvalues for the other directions.

The Euler-Lagrange equations that arise from (3.13) are

$$\nabla\cdot\boldsymbol{\sigma} + \boldsymbol{b} = \boldsymbol{0},\ \boldsymbol{x}\in\Omega \quad (3.14)$$

$$\boldsymbol{t} = -\boldsymbol{K}(\boldsymbol{u}-\boldsymbol{u}^m),\ \boldsymbol{x}\in\Gamma \quad (3.15)$$

We note that $\boldsymbol{K}\approx 0$ in the directions in which we have little confidence in the measured displacements. In those cases, the BCs in (3.15) predict zero traction, which may or may not be appropriate.

3.3.2 Domain Springs Formulation

Alternatively, the data-match term could act over all of Ω instead of only the boundary Γ, yielding a functional with springs in the domain instead of only on the boundary. This leads to

$$\pi^f[\boldsymbol{u}] = \underbrace{\frac{1}{2}\int_\Omega \boldsymbol{\sigma}(\boldsymbol{u}) : \boldsymbol{\epsilon}(\boldsymbol{u})\ d\Omega - \int_\Omega \boldsymbol{b}\cdot\boldsymbol{u}\ d\Omega}_{\text{strain-energy}} + \underbrace{\frac{1}{2}\int_\Omega (\boldsymbol{u}-\boldsymbol{u}^m)\cdot\boldsymbol{K}(\boldsymbol{u}-\boldsymbol{u}^m)\ d\Omega}_{\text{domain spring penalty}} \quad (3.16)$$

The Euler-Lagrange equations for this approach are

$$\nabla\cdot\boldsymbol{\sigma} + \boldsymbol{b} = \boldsymbol{K}(\boldsymbol{u}-\boldsymbol{u}^m),\ \boldsymbol{x}\in\Omega \quad (3.17)$$

$$\boldsymbol{t} = \boldsymbol{0},\ \boldsymbol{x}\in\Gamma \quad (3.18)$$

We note that the boundary springs approach enforces the equilibrium equation (3.6) exactly in the domain, while the domain springs approach enforces the equilibrium equation augmented with forcing terms from the springs.

3.3.2.1 Weak Springs

The addition of a scaled spring-like energy term to the forward problem functional weighted by a "small" spring tensor can be used to constrain the rigid body motion using the measured displacements. The purpose of the scaling is to reduce the strength of the springs such that they do not overly influence the deformation but are still strong enough to adequately constrain rigid body motion. The weak springs functional can be viewed as a special case of the domain springs approach where the springs are "concentrated" at points as shown in (3.19). They provide a means of addressing this subtle but important computational issue.

$$\pi^{ws}[\boldsymbol{u}] = \frac{1}{2}\sum_{i=1}^{N}(\boldsymbol{u}_i - (\boldsymbol{u}^m)_i)\cdot\boldsymbol{K}(\boldsymbol{u}_i - (\boldsymbol{u}^m)_i) \quad (3.19)$$

3.4 Results

3.4.1 Forward Problem Results

Figure 3·2: Springy bar simulation

The simulated experiment in Figure (3·2) illustrates how the presence of springs affects the forward problem's solution. A 10 by 1 units bar is attached to rollers at the bottom and pulled at the top by springs whose strengths increase logarithmically from left to right. The end of the springs not attached to the bar are fixed to a displacement of 0.01 units. On the left, the springs are too weak to produce any noticeable displacement, while on the right side of the bar the springs are practically imposing the value they are tied to as a Dirichlet BC. Thus, the size of the spring constant (which can vary spatially) determines the degree to which $\boldsymbol{u}$ can be different from $\boldsymbol{u}^m$.

We now discuss the use of springs elements on the simulated data presented in Appendix B. The entries of the spring tensor are as shown in equation (3.20). This choice reflects the knowledge that the u_x^m is less precise than u_y^m. The scaling constant κ can be varied to control the strength of the springs.

$$K_{ij} = \kappa \begin{pmatrix} .25 & 0 \\ 0 & 1 \end{pmatrix} \tag{3.20}$$

The y components of the noiseless displacement field and noise-corrupted measurement that serves as the input to the forward problem are shown in Figure (3·3). The results in Figure (3·4) show that as κ increases in the boundary springs for-

mulation, the boundary values of the predicted displacement field become closer to those of the measured displacement field. The displacement field in the interior of the domain remains smooth. Increasing κ in the domain springs formulation causes the entire displacement field to approach the measurement, as depicted in Figure (3·5).

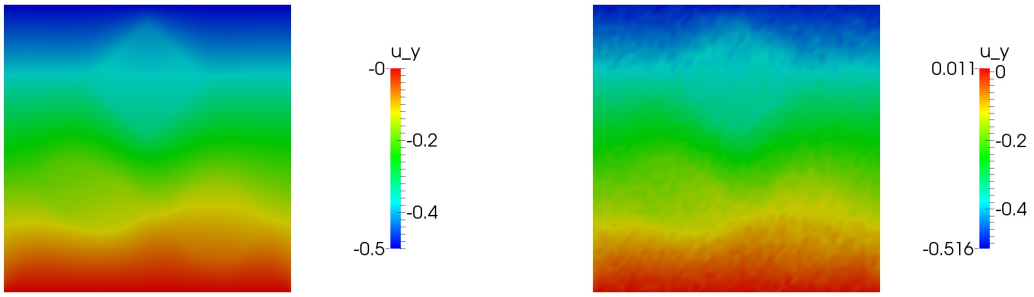

Noiseless Noisy

Figure 3·3: Plane stress target u_y and input u_y^m

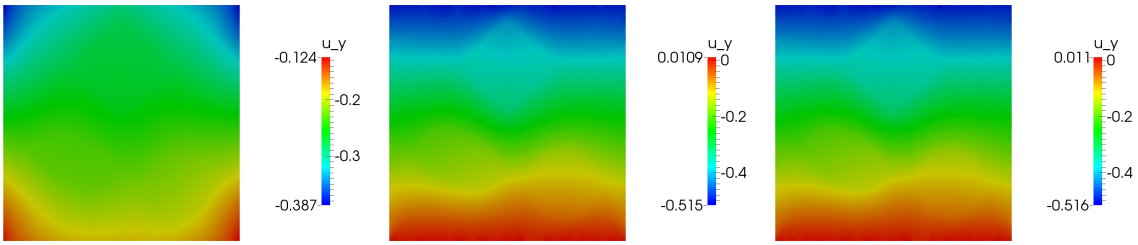

Small κ Medium κ Large κ

Figure 3·4: Plane stress boundary springs forward problem u_y with exact μ

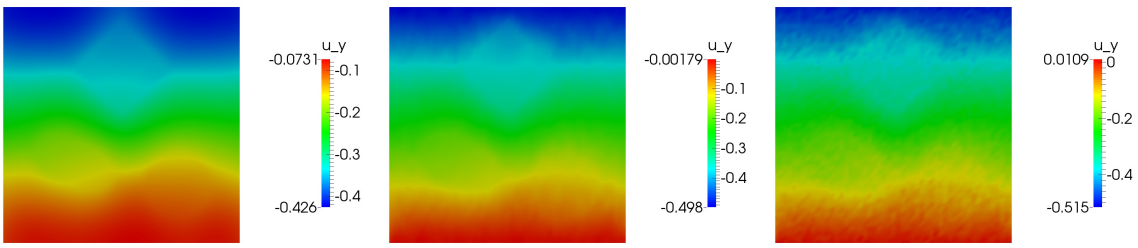

Small κ Medium κ Large κ

Figure 3·5: Plane stress domain springs forward problem u_y with exact μ

3.4.2 Inverse Problem Results

Next we used the springs formulation as the constraint equation in a plane stress inverse problem. We see in Figure (3·6) that the larger κ is in the boundary springs approach, the more accurate the inverse problem solution.

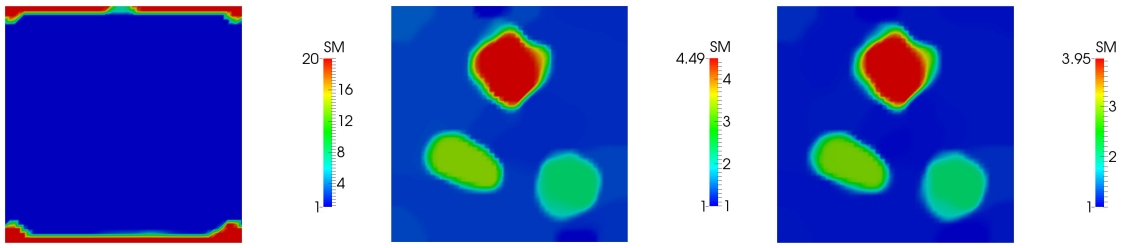

Small κ Medium κ Large κ

Figure 3·6: Plane stress boundary springs inverse problem results

The domain springs approach, however, failed to provide reasonable modulus reconstructions for any κ. Results from the application of domain springs to the plane stress simulated data are shown in Figure (3·7). The use of domain springs with large spring constants produced a reconstruction that failed to move off the initial guess. A spring constant size somewhere between too large and too small to cause any displacement produced results with incorrect inclusion shapes and contrasts.

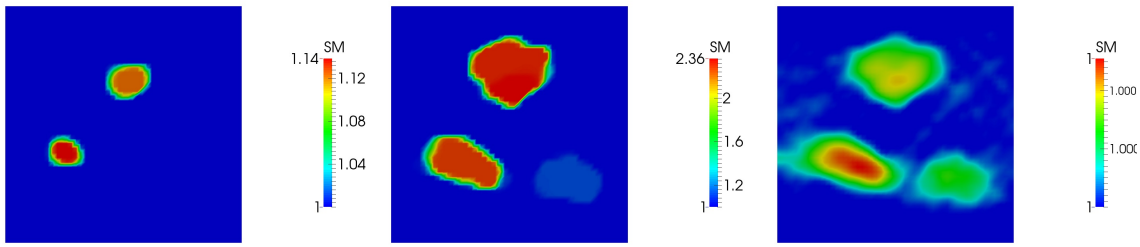

Small κ Medium κ Large κ

Figure 3·7: Plane stress domain springs forward problem with exact μ

Figure (3·8) shows modulus inversions obtained using the boundary and domain springs approaches in plane strain. The boundary springs reconstruction is consider-

ably more accurate than the assumed BCs results. Considering the sensitivity of the plane strain inverse problem to BCs, it is surprising that spring boundary conditions were able to perform so well. The domain springs approach performed poorly in plane strain as well.

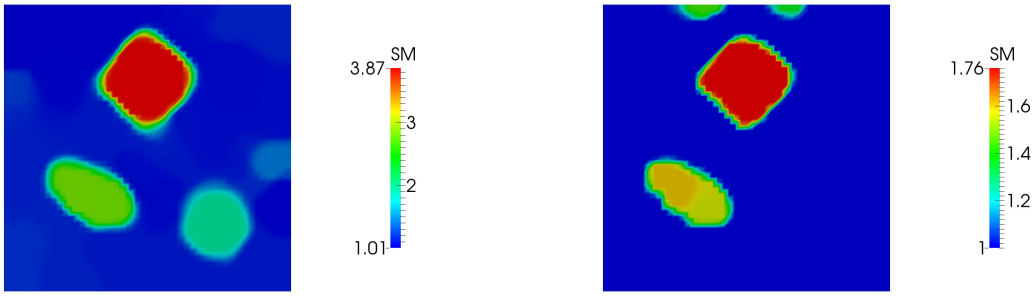

Boundary Springs Reconstruction Domain Springs Reconstruction

Figure 3·8: Plane strain springs results

3.5 Discussion

The 2D simulated results show that boundary springs can be used to add information about the deformation that leads to better modulus reconstructions. The assumed BCs prescribe zero lateral traction at the bottom of the domain, inconsistent with the zero lateral displacement BC used to generate the problem data. As a result, an artificially stiff layer is present in both assumed BCs reconstructions, although it is much more prominent in plane strain (see Appendix B).

Boundary springs can impose the assumed BCs case using a specific choice of spring tensor K_{ij}. In 2D this can be achieved by setting K_{11} and K_{12} to zero while making K_{22} infinite (in practice, a large number). If we interpret $\boldsymbol{K}$ as $\boldsymbol{C}^{-1}$, this case corresponds the use of a diagonal covariance matrix where the lateral component of the measurement noise is significantly greater than the axial component.

Techniques for improving estimates of the lateral and elevational components of displacement in BMI have been and are still being researched. We expect spring

boundary elements to be useful on such data. First, they allow for "weighted" enforcement of displacement boundary conditions, where the weights are based on the relative noise in each component of measured displacement. Second, if one uses all the components of the measurement displacement field as a Dirichlet BC (a conceivable choice if the noise in each component is comparable), they will run into issues associated with the use of an incompressible material model (specifically in plane strain and 3D). The prescribed Dirichlet BCs must satisfy incompressibility, which will almost certainly be impossible to achieve due to measurement noise. The use of spring elements circumvents this issue as the displacements of the springs have no such requirement.

Recently, the modified error in the constitutive relation inverse problem formulation has been adapted to address uncertainty in displacement boundary conditions (Bonnet and Aquino, 2015), (Diaz et al., 2015). They include a data-match term that weights the displacement mismatch over the "unreliable" portion of the boundary, where the displacement BC is not known exactly, in addition to the normal data-match term in the domain. In their approach, the forward and adjoint problems are coupled, and the uncertain boundary terms reside in the equation containing the adjoint operator. This contrasts with our spring boundary element approach, where the forward and adjoint problems are decoupled and the springs term shows up in the forward PDE. A final difference is our use of tensors to weight data mismatch terms (because measurement noise often varies component-wise) while they use constants.

Finally, we discuss possible reasons for the dramatic failure of the domain springs approach. First, equation (3.17) shows that the equilibrium is not being enforced in the domain. Second, a large spring constant will force $\boldsymbol{u}$ to be equal to $\boldsymbol{u}^m$ inside the domain, which will cause the right hand side of the adjoint problem to be small. Additionally, the domain springs contribute a term to each entry of the stiffness

matrix of the forward and adjoint problem. These combined effects diminish the size of the adjoint variables, which in turn causes the gradient to be small, making the objective function less sensitive to changes in modulus.

Chapter 4

CASE Formulation

4.1 Introduction

The adjoint method requires a well-posed forward problem, hence there is a need for sufficient boundary data to render it so. Measured displacements prescribed on the boundary are given special status over those measured in the domain, while Neumann BCs must be assumed as no measurements of traction are typically available. Treating the BCs in this manner introduces a bias in the solution of the inverse problem.

The formulation discussed in this chapter is designed with the goal of solving the forward problem without using any displacement and/or traction BCs.

4.2 Incompressible Plane Stress Formulation

We start with a Lagrangian that contains a plane stress elasticity equilibrium constraint and a weighted least squares data match term. The measured displacement field $\boldsymbol{u}^m$ and shear modulus μ are assumed to be known.

$$\mathcal{L}[\boldsymbol{u}, \boldsymbol{w}] = \frac{1}{2} \int_\Omega \boldsymbol{T}(\boldsymbol{u} - \boldsymbol{u}^m) \cdot \boldsymbol{T}(\boldsymbol{u} - \boldsymbol{u}^m) \; d\Omega - \int_\Omega \boldsymbol{w} \cdot (\nabla \cdot (\mu \boldsymbol{A}(\boldsymbol{u}))) \; d\Omega \qquad (4.1)$$

4.2.1 Weak Form

Integration by parts is performed on the constraint term. The function spaces for the forward and adjoint variables and their variations are identical in this approach, as

there are no essential boundary conditions.

$$-\int_{\Omega} \boldsymbol{w} \cdot (\nabla \cdot (\mu \boldsymbol{A}(\boldsymbol{u}))) \; d\Omega = \int_{\Omega} \nabla \boldsymbol{w} : \mu \boldsymbol{A}(\boldsymbol{u}) \; d\Omega - \int_{\Gamma} \boldsymbol{w} \cdot \mu \boldsymbol{A}(\boldsymbol{u}) \cdot \boldsymbol{n} \; d\Gamma \tag{4.2}$$

$$\boldsymbol{u}, \delta \boldsymbol{u} \in \mathcal{S} \;\; \equiv \;\; \{\boldsymbol{u} \mid u_i \in H^1(\Omega)\} \tag{4.3}$$

$$\boldsymbol{w}, \delta \boldsymbol{w} \in \mathcal{V} \;\; \equiv \;\; \{\boldsymbol{w} \mid w_i \in H^1(\Omega)\} \tag{4.4}$$

The weak form is obtained by taking variations w.r.t $\boldsymbol{u}$ and $\boldsymbol{w}$. For convenience, we define $\boldsymbol{D} = \boldsymbol{T}^T \boldsymbol{T}$.

$$D_{\boldsymbol{u}} \mathcal{L} \cdot \delta \boldsymbol{u} = \int_{\Omega} \delta \boldsymbol{u} \cdot \boldsymbol{D}(\boldsymbol{u} - \boldsymbol{u}^m) \; d\Omega + \int_{\Omega} \nabla \boldsymbol{w} : \mu \boldsymbol{A}(\delta \boldsymbol{u}) \; d\Omega - \int_{\Gamma} \boldsymbol{w} \cdot \mu \boldsymbol{A}(\delta \boldsymbol{u}) \cdot \boldsymbol{n} \; d\Gamma \stackrel{set}{=} 0 \; \forall \; \delta \boldsymbol{u} \in \mathcal{V} \tag{4.5}$$

$$D_{\boldsymbol{w}} \mathcal{L} \cdot \delta \boldsymbol{w} = \int_{\Omega} \nabla \delta \boldsymbol{w} : \mu \boldsymbol{A}(\boldsymbol{u}) \; d\Omega - \int_{\Gamma} \delta \boldsymbol{w} \cdot \mu \boldsymbol{A}(\boldsymbol{u}) \cdot \boldsymbol{n} \; d\Gamma \stackrel{set}{=} 0 \; \forall \; \delta \boldsymbol{w} \in \mathcal{V} \tag{4.6}$$

Equations (4.5) and (4.6) are the weak forms that serve as the basis for the computational solution.

4.2.2 Euler-Lagrange Equations

We integrate equations (4.5) and (4.6) by parts to determine their Euler-Lagrange equations and natural BCs.

$$\int_\Omega \delta\boldsymbol{u}\cdot(\boldsymbol{D}(\boldsymbol{u}-\boldsymbol{u}^m)-\nabla\cdot(\mu\boldsymbol{A}(\boldsymbol{w})))\ d\Omega+\int_\Gamma \delta\boldsymbol{u}\cdot(\mu\boldsymbol{A}(\boldsymbol{w})\cdot\boldsymbol{n})\ d\Gamma \tag{4.7}$$

$$-\int_\Gamma \boldsymbol{w}\cdot(\mu\boldsymbol{A}(\delta\boldsymbol{u})\cdot\boldsymbol{n})\ d\Gamma=0\ \forall\ \delta\boldsymbol{u}\in\mathcal{V}$$

$$-\int_\Omega \delta\boldsymbol{w}\cdot(\nabla\cdot(\mu\boldsymbol{A}(\boldsymbol{u})))\ d\Omega=0\ \forall\ \delta\boldsymbol{w}\in\mathcal{V} \tag{4.8}$$

The last term in (4.7) is not of standard form, and it is not immediately obvious what BC is implied therefrom. To obtain the natural BC implied by the last term in (4.7) we introduce an arbitrary smooth vector field $a_i(\boldsymbol{x})$ and a scalar field $\phi(\boldsymbol{x})$ that is greater than zero for all $\boldsymbol{x}\in\Omega$ and equal to zero for all $\boldsymbol{x}\in\Gamma$. We then define δu_i in terms of them:

$$\delta u_i = \phi(\boldsymbol{x})a_i(\boldsymbol{x}) \tag{4.9}$$

$$\delta u_{i,j}|_{\boldsymbol{x}\in\Gamma} = \phi_{,j}(\boldsymbol{x})a_i(\boldsymbol{x})|_{\boldsymbol{x}\in\Gamma}+\cancel{\phi(\boldsymbol{x})a_{i,j}(\boldsymbol{x})|_{\boldsymbol{x}\in\Gamma}}=\phi_{,j}(\boldsymbol{x})a_i(\boldsymbol{x})|_{\boldsymbol{x}\in\Gamma} \tag{4.10}$$

Substitution into the term of interest yields the expression

$$-\int_\Gamma \boldsymbol{w}_i(\mu A_{ij}(\phi\boldsymbol{a})n_j)\ d\Gamma=0\ \forall\ \phi\boldsymbol{a}\in\mathcal{V} \tag{4.11}$$

Note that the definition of ϕ implies

$$\nabla\phi(\boldsymbol{x})|\boldsymbol{x}\in\Gamma=-\|\nabla\phi\|\boldsymbol{n} \tag{4.12}$$

Therefore $A_{ij}(\phi\boldsymbol{a})n_j$ for $\boldsymbol{x} \in \Gamma$ is

$$\begin{aligned} A_{ij}(\phi\boldsymbol{a})n_j &= \big[2\phi_{,k}a_k\delta_{ij} + \phi_{,i}a_j + \phi_{,j}a_i\big]n_j \\ &= \big[-2\|\nabla\phi(\boldsymbol{x})\|n_k a_k\delta_{ij} - \|\nabla\phi(\boldsymbol{x})\|n_i a_j - \|\nabla\phi(\boldsymbol{x})\|n_j a_i\big]n_j \\ &= -3\|\nabla\phi(\boldsymbol{x})\|n_i a_n - \|\nabla\phi(\boldsymbol{x})\|a_i \\ &= -4\|\nabla\phi(\boldsymbol{x})\|n_i a_n - \|\nabla\phi(\boldsymbol{x})\|a_j\tau_{ij} \end{aligned} \tag{4.13}$$

In (4.13), we introduced $\tau_{ij} = \delta_{ij} - n_i n_j$, which gives the tangential component of any vector and $a_n = a_i n_i$. Therefore, if we choose $a_i = w_i$ on Γ in (4.13) we find:

$$\begin{aligned} &-\int_\Gamma \mu w_i\left(-4\|\nabla\phi(\boldsymbol{x})\|n_i w_n - \|\nabla\phi(\boldsymbol{x})\|w_j\tau_{ij}\right)\, d\Gamma \\ = \;& 4\int_\Gamma \mu w_n\|\nabla\phi(\boldsymbol{x})\|w_n\, d\Gamma + \int_\Gamma \mu w_\tau\|\nabla\phi(\boldsymbol{x})\|w_\tau\, d\Gamma = 0 \end{aligned} \tag{4.14}$$

The integrand in (4.14) is clearly non-negative for any $\boldsymbol{w}$, so we conclude that $\boldsymbol{w}$ must vanish on the boundary. Using this result and equations (4.7) and (4.8) we state the Euler-Lagrange equations and natural BCs

$$\nabla\cdot(\mu\boldsymbol{A}(\boldsymbol{u})) = \boldsymbol{0}\ ,\ \boldsymbol{x}\in\Omega \tag{4.15}$$

$$\nabla\cdot(\mu\boldsymbol{A}(\boldsymbol{w})) = \boldsymbol{D}(\boldsymbol{u}-\boldsymbol{u}^m)\ ,\ \boldsymbol{x}\in\Omega \tag{4.16}$$

$$\boldsymbol{w} = \boldsymbol{0}\ ,\ \boldsymbol{x}\in\Gamma \tag{4.17}$$

$$\mu\boldsymbol{A}(\boldsymbol{w})\cdot\boldsymbol{n} = \boldsymbol{0}\ ,\ \boldsymbol{x}\in\Gamma \tag{4.18}$$

This system of coupled equations has no BCs specified on the displacement field, however, the Lagrange multiplier has two BCs.

4.2.3 Discretization

We now assign symbols to pieces of the discretized version of the weak forms (4.5) and (4.6). We avoid writing closed form expressions for the components for which such is not straightforward.

$$\{\delta u\}^T[M_D]\{u\} \longleftrightarrow \int_\Omega \delta u_i^a N_a D_{ij}^c N_c N_b u_j^b \; d\Omega \tag{4.19}$$

$$\{\delta w\}^T[K]\{u\} \longleftrightarrow \int_\Omega \delta w_i^a N_{a,j} \mu^c N_c A(\boldsymbol{u}^b N_b)_{ij} \; d\Omega \tag{4.20}$$

$$\{\delta w\}^T[B]\{u\} \longleftrightarrow \int_\Gamma \delta w_i^a N_a \mu^c N_c A(\boldsymbol{u}^b N_b)_{ij} n_j \; d\Gamma \tag{4.21}$$

$$\begin{aligned} \{w\}^T[K]\{\delta u\} &\longleftrightarrow \int_\Omega w_i^a N_{a,j} \mu^c N_c A(\delta \boldsymbol{u}^b N_b)_{ij} \; d\Omega \\ &= \{\delta u\}^T[K]^T\{w\} \end{aligned} \tag{4.22}$$

$$\begin{aligned} \{w\}^T[B]\{\delta u\} &\longleftrightarrow \int_\Gamma w_i^a N_a \mu^c N_c A(\delta \boldsymbol{u}^b N_b)_{ij} n_j \; d\Gamma \\ &= \{\delta u\}^T[B]^T\{w\} \end{aligned} \tag{4.23}$$

Putting it all together, we arrive at the symmetric block linear system (4.24). Note that the symmetry of this system is solely due to $[M_D]$ being a symmetric matrix. We call this a Coupled Adjoint-State Equation (CASE) system because the the adjoint and state problems are coupled due to the formulation's lack of displacement and traction BCs.

$$\begin{bmatrix} [M_D] & ([K]^T - [B]^T) \\ ([K] - [B]) & \mathbf{0} \end{bmatrix} \begin{Bmatrix} u \\ w \end{Bmatrix} = \begin{Bmatrix} [M_D]u^m \\ \mathbf{0} \end{Bmatrix} \tag{4.24}$$

This indefinite system is singular when linear shape functions are employed for $\boldsymbol{u}^h$ and $\boldsymbol{w}^h$. We present two approaches to stabilize the system.

4.2.4 Stabilization

4.2.4.1 Weak Stabilization

First we use residual-based stabilization. A GLS term based on equation (4.17) is appended to the Lagrangian functional. A constant h is present to scale the stabilization by the mesh size. For triangle elements, h can be defined to be the length of the longest edge.

$$\mathcal{L}_1[\boldsymbol{u}, \boldsymbol{w}] = \mathcal{L}[\boldsymbol{u}, \boldsymbol{w}] - \frac{1}{2h^2} \int_\Gamma \boldsymbol{w} \cdot \boldsymbol{w} \; d\Gamma \tag{4.25}$$

The weak form (4.6) becomes

$$D_{\boldsymbol{w}} \mathcal{L}_1 \cdot \delta \boldsymbol{w} = D_{\boldsymbol{w}} \mathcal{L} \cdot \delta \boldsymbol{w} - \frac{1}{h^2} \int_\Gamma \boldsymbol{w} \cdot \delta \boldsymbol{w} \; d\Gamma \stackrel{set}{=} 0 \; \forall \; \delta \boldsymbol{w} \in \mathcal{V} \tag{4.26}$$

In this formulation, a negative semi-definite mass matrix appears in the lower right part of the saddle point system.

$$\begin{bmatrix} [M_D] & ([K]^T - [B]^T) \\ ([K] - [B]) & [D] \end{bmatrix} \begin{Bmatrix} u \\ w \end{Bmatrix} = \begin{Bmatrix} [M_D^*] u^m \\ \mathbf{0} \end{Bmatrix} \tag{4.27}$$

$$\{\delta w\}^T [D] \{w\} \longleftrightarrow -\frac{1}{h^2} \int_\Gamma \delta w_i^a \delta_{ij} N_a N_b w_j^b \; d\Gamma \tag{4.28}$$

4.2.4.2 Weak Stabilization Results

In this section we used the plane stress simulated measured displacement fields (see Appendix B) as inputs to the CASE formulation. The noiseless displacement field is given in Figure (4·1) for reference. The results shown in Figure (4·2) were computed using the exact μ and a noiseless displacement field as input. Figure (4·3) shows results obtained using the exact μ and the noisy displacement field from Appendix B

as input. Finally, Figure (4·4) contains results computed with a $\mu = 1$ and the noisy displacement field as input.

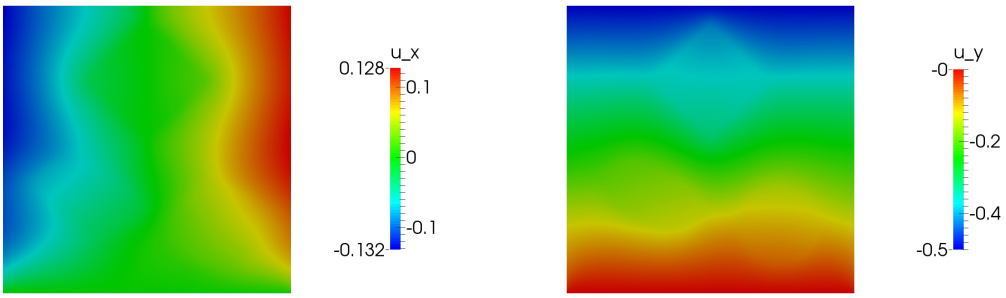

Figure 4·1: Plane stress noiseless $\boldsymbol{u}^m$

The displacements fields shown in Figures (4·2) and (4·3) look like the exact displacement fields. Interestingly, the magnitude of the errors between the exact and predicted displacement fields in these results are of comparable size. We note that this inverse problem was solved on a different mesh than was used to generate the noiseless data, and is a possible source of the error observed in Figure (4·2). These results demonstrate that the CASE formulation can successfully estimate the correct displacement field given the correct μ without prescribing any BCs on $\boldsymbol{u}$.

Figure (4·4) demonstrates what happens when the formulation is not given the exact μ. A displacement field that satisfies equilibrium is produced, but it is clearly not a smoothed version of the measurements. This demonstrates that the method is not merely reproducing the input displacement fields, but rather is sensitive to the modulus distribution as well.

4.2.4.3 Strong Stabilization

Our second approach to stabilizing the discrete saddle point system involves enforcing the natural boundary condition (4.17) strongly. This is achieved by changing the

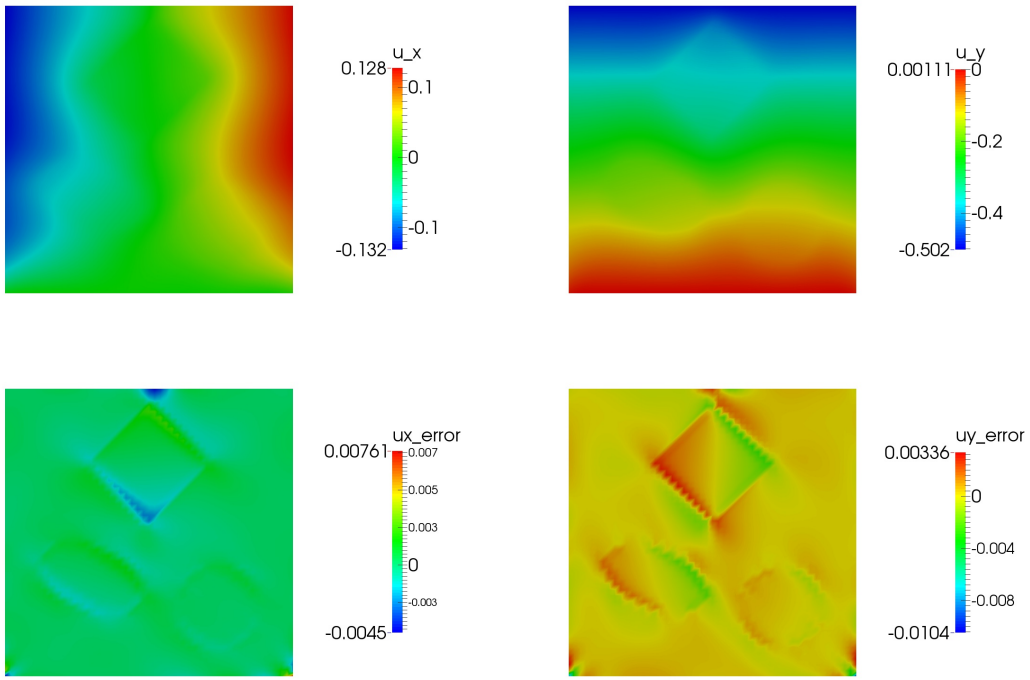

Figure 4·2: Forward plane stress CASE with weak stabilization, exact μ, and noiseless $\boldsymbol{u}^m$ results

function space for the Lagrange multiplier $\boldsymbol{w}$ and its weight to be

$$\boldsymbol{w}, \delta\boldsymbol{w} \in \mathcal{V} \equiv \{\boldsymbol{w} \mid w_i \in H^1(\Omega), w_i = 0 \text{ on } \Gamma\}. \tag{4.29}$$

$$D_{\boldsymbol{u}}\mathcal{L} \cdot \delta\boldsymbol{u} = \int_\Omega \delta\boldsymbol{u} \cdot \boldsymbol{D}(\boldsymbol{u} - \boldsymbol{u}^m)\, d\Omega + \int_\Omega \nabla\boldsymbol{w} : \mu\boldsymbol{A}(\delta\boldsymbol{u})\, d\Omega \overset{set}{=} 0 \;\forall\; \delta\boldsymbol{u} \in \mathcal{V} \tag{4.30}$$

$$D_{\boldsymbol{w}}\mathcal{L} \cdot \delta\boldsymbol{w} = \int_\Omega \nabla\delta\boldsymbol{w} : \mu\boldsymbol{A}(\boldsymbol{u})\, d\Omega \overset{set}{=} 0 \;\forall\; \delta\boldsymbol{w} \in \mathcal{V} \tag{4.31}$$

Note that the weak form (4.30) and (4.31) is significantly simpler in this case. Upon discretization, this leads to a system similar to (4.24), except that the $[B]$ matrices disappear, and the overall size of the linear system is reduced by the number of boundary nodes times two, viz:

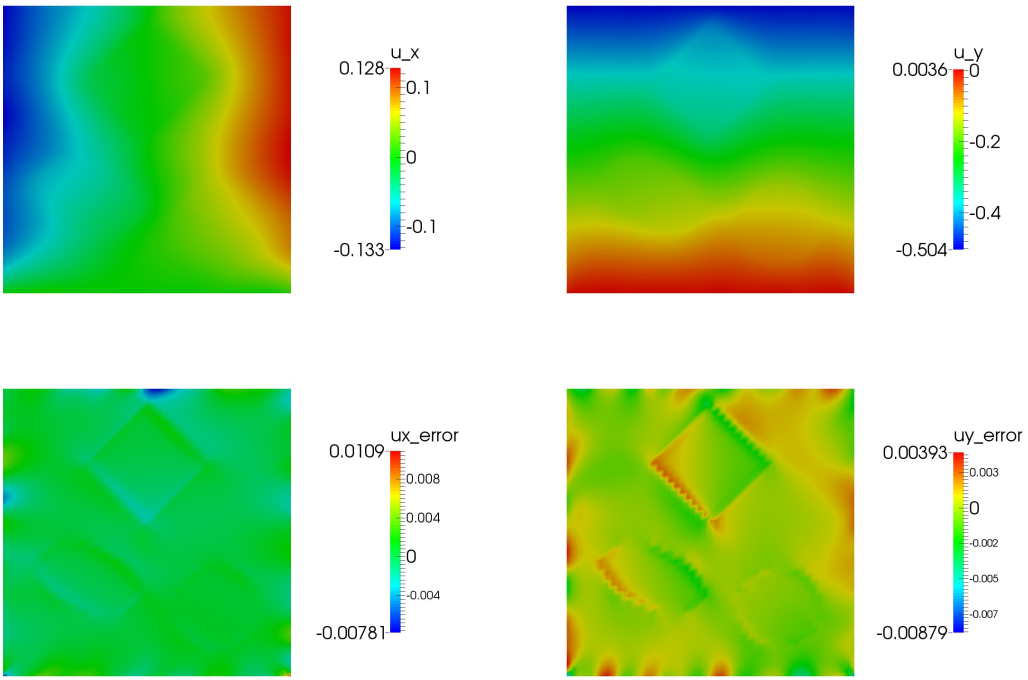

Figure 4·3: Forward plane stress CASE with weak stabilization, exact μ, and noisy $\boldsymbol{u}^m$ results

$$\begin{bmatrix} [M_D] & [K]^T \\ [K] & \mathbf{0} \end{bmatrix} \begin{Bmatrix} u \\ w \end{Bmatrix} = \begin{Bmatrix} [M_D]u^m \\ \mathbf{0} \end{Bmatrix} \tag{4.32}$$

4.2.4.4 Strong Stabilization Results

The results obtained using the second stabilization approach are shown in Figures (4·5), (4·6), and (4·7). They are similar to the results obtained using the first formulation except along the boundary in Figures (4·6) and (4·7) where there are fluctuations in the displacement fields, most noticeably in the (more uncertain) lateral component. We hypothesize that the origin of these variations is the roughness of the measured displacement field due to their absence from Figure (4·5).

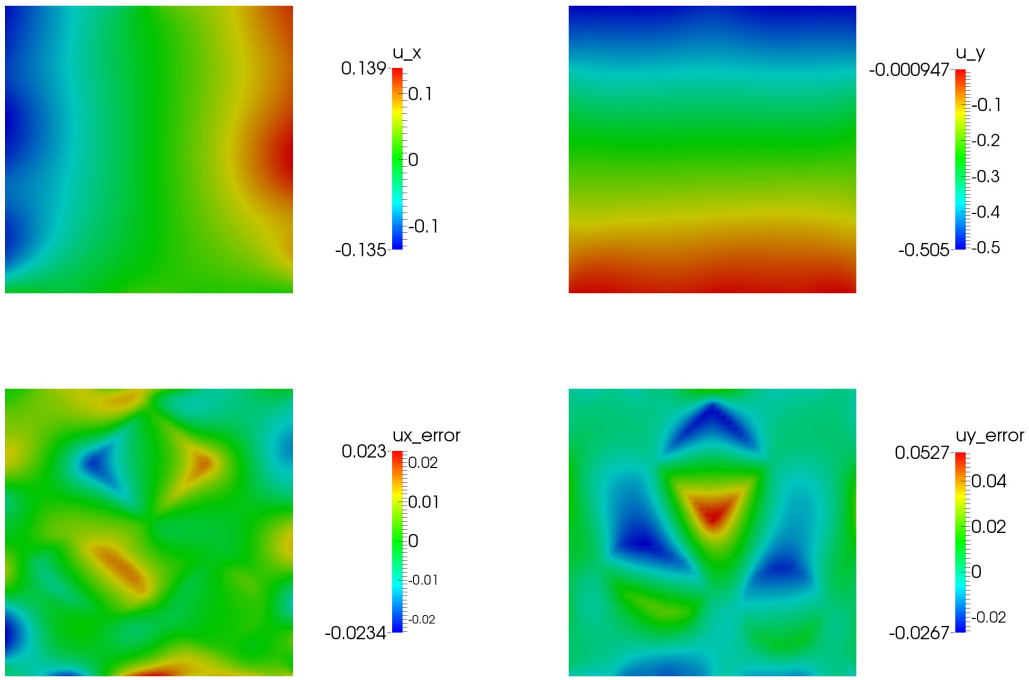

Figure 4·4: Forward plane stress CASE with weak stabilization, $\mu = 1$, and noisy $\boldsymbol{u}^m$ results

4.2.5 Inverse Problem Formulation

Now we consider using the CASE formulation to solve a plane stress inverse problem. Note that the Lagrangian for the inverse problem is (4.1) with the addition of a regularization term.

$$\mathcal{L}[\boldsymbol{u}, \boldsymbol{w}, \mu] = \frac{1}{2} \int_\Omega \boldsymbol{T}(\boldsymbol{u}-\boldsymbol{u}^m)\cdot\boldsymbol{T}(\boldsymbol{u}-\boldsymbol{u}^m)\, d\Omega - \int_\Omega \boldsymbol{w}\cdot(\nabla\cdot(\mu\boldsymbol{A}(\boldsymbol{u})))\, d\Omega + \alpha\mathcal{R}[\mu] \quad (4.33)$$

The formula for the gradient is obtained by taking variations w.r.t each of the Lagrangian's arguments as described in the Chapter 1. The solution of the CASE system causes the first two terms in (4.34) to vanish.

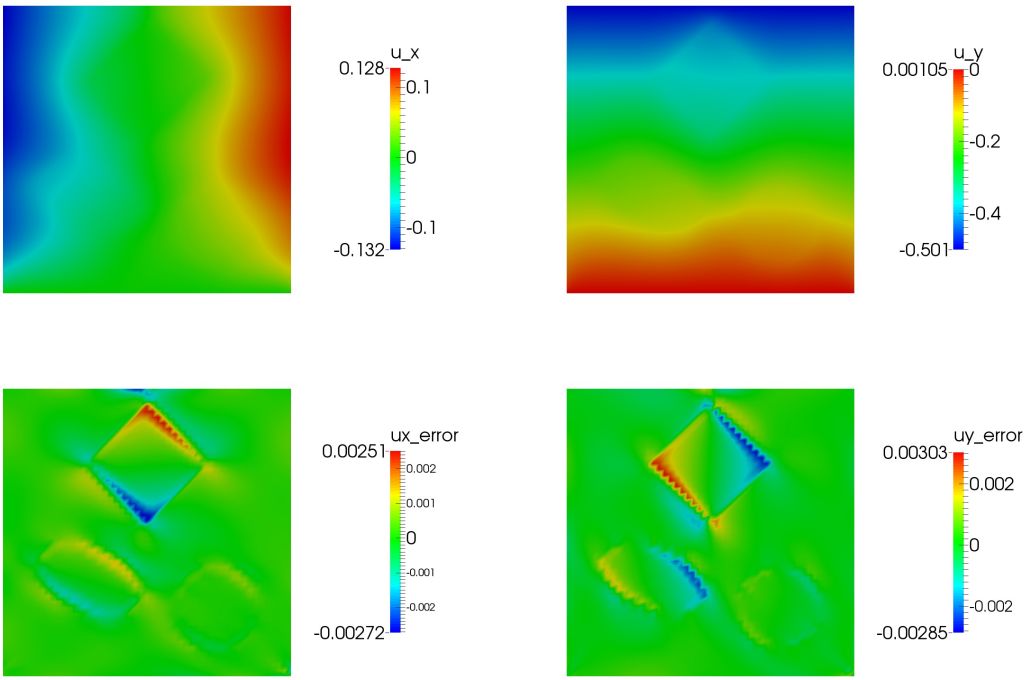

Figure 4·5: Forward plane stress CASE with strong stabilization, exact μ, and noiseless $\boldsymbol{u}^m$ results

$$\delta\mathcal{L} = \cancel{D_{\boldsymbol{u}}\mathcal{L}\cdot\delta\boldsymbol{u}} + \cancel{D_{\boldsymbol{w}}\mathcal{L}\cdot\delta\boldsymbol{w}} + D_\mu\mathcal{L}\cdot\delta\mu \tag{4.34}$$

$$= \int_\Omega \nabla\boldsymbol{w} : \delta\mu\boldsymbol{A}(\boldsymbol{u})\ d\Omega - \int_\Gamma \boldsymbol{w}\cdot\delta\mu\boldsymbol{A}(\boldsymbol{u})\cdot\boldsymbol{n}\ d\Gamma + D_\mu\mathcal{R}\cdot\delta\mu \tag{4.35}$$

The elemental form of the material component of the gradient is

$$\{g^c_{\text{mat}}\}_c = \int_\Omega w^a_i N_{a,j} N_c A(\boldsymbol{u}^b N_b)_{ij}\ d\Omega - \int_\Gamma w^a_i N_a N_c A(\boldsymbol{u}^b N_b)_{ij} n_j\ d\Gamma \tag{4.36}$$

Figure (4·8) contains inverse problem solutions obtained using the two CASE formulations described in this section. The reconstructions are remarkably similar, and are much closer to the exact modulus distribution than results obtained using

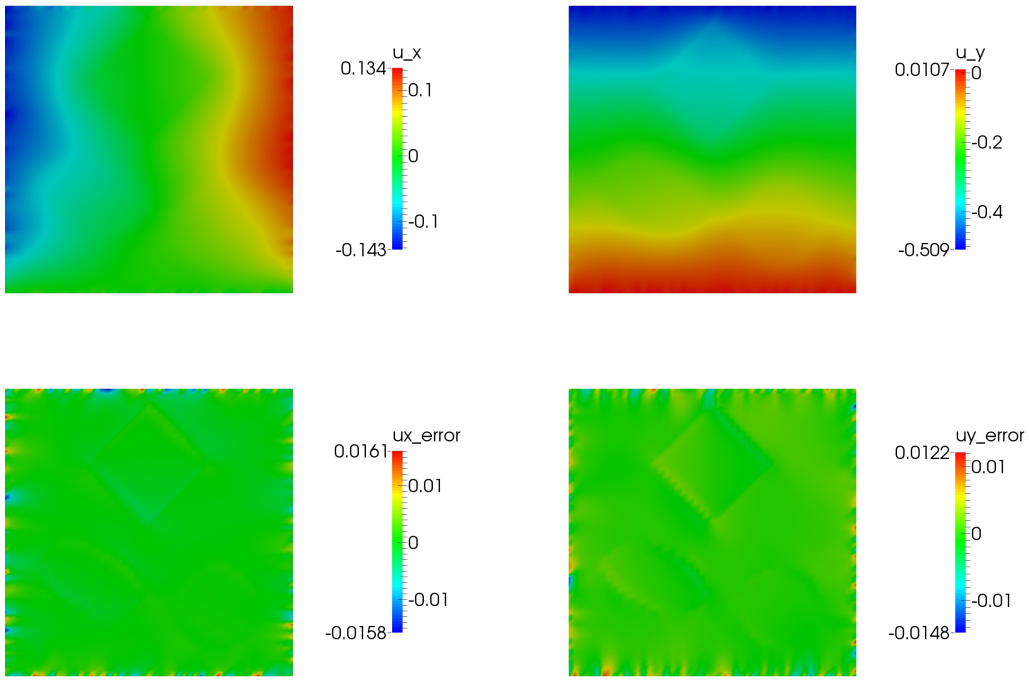

Figure 4·6: Forward plane stress CASE with strong stabilization, exact μ, and noisy $\boldsymbol{u}^m$ results

assumed BCs. Interestingly, the fluctuations in the boundary displacements present in the strong stabilization approach do not appear to have a deleterious effect on the inverse problem solution.

4.3 Incompressible Plane Strain and 3D Formulation

As shown in appendix A, in incompressible plane stress one can use the incompressiblilty constraint to eliminate the pressure field variable. Unfortunately, one must treat the pressure as an unknown in incompressible plane strain and 3D. We present the CASE formulation in these contexts. The presentation is identical for both modeling cases; all that changes is the range of indices.

The Lagrangian for this CASE system is

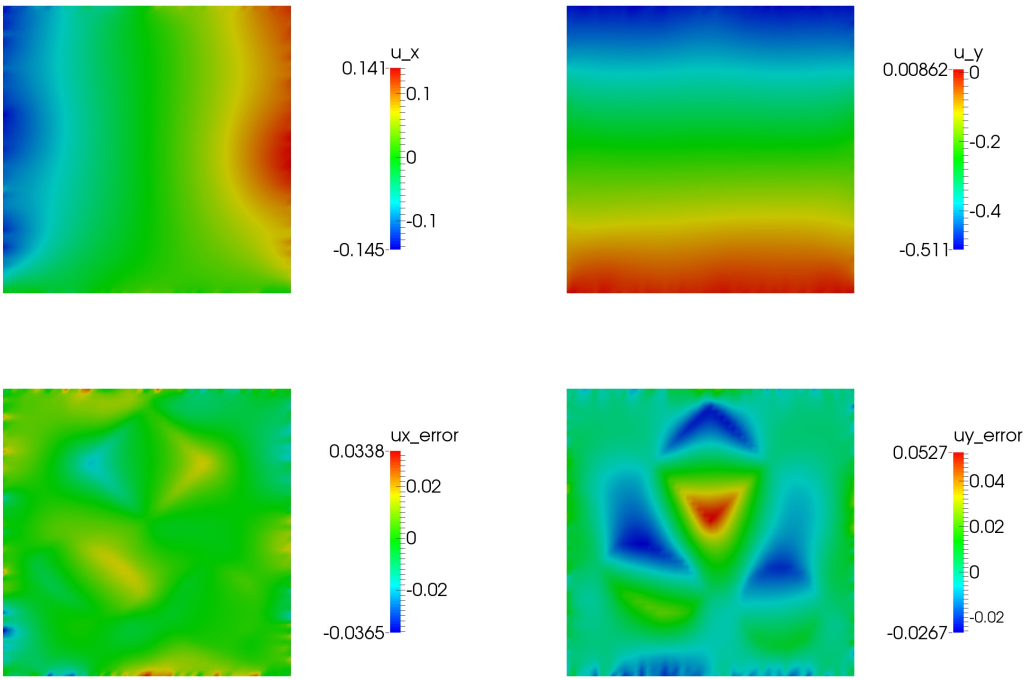

Figure 4·7: Forward plane stress CASE with strong stabilization, $\mu = 1$, and noisy $\boldsymbol{u}^m$ results

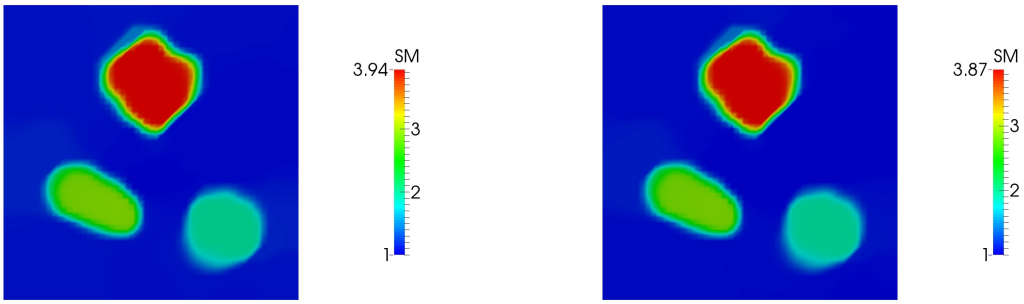

Weak stabilization Strong stabilization

Figure 4·8: Reconstructed μ for each plane stress CASE formulation

$$\begin{aligned} \mathcal{L}[\boldsymbol{u}, \boldsymbol{w}, p, q] &= \frac{1}{2}\int_\Omega \boldsymbol{T}(\boldsymbol{u}-\boldsymbol{u}^m)\cdot\boldsymbol{T}(\boldsymbol{u}-\boldsymbol{u}^m)\,d\Omega - \int_\Omega q\nabla\cdot\boldsymbol{u}\,d\Omega \qquad (4.37) \\ &- \int_\Omega \boldsymbol{w}\cdot(\nabla\cdot\boldsymbol{\sigma}(\boldsymbol{u},p))\;d\Omega \end{aligned}$$

4.3.1 Weak Form

The constitutive relation is substituted into the equilibrium constraint and is integrated by parts

$$\int_{\Omega} \boldsymbol{w} \cdot (\nabla \cdot \boldsymbol{\sigma}(\boldsymbol{u}, p)) \; d\Omega = \int_{\Omega} \nabla \boldsymbol{w} : (-p\boldsymbol{I} + 2\mu \nabla^s \boldsymbol{u}) \; d\Omega \tag{4.38}$$

$$- \int_{\Gamma} \boldsymbol{w} \cdot (-p\boldsymbol{I} + 2\mu \nabla^s \boldsymbol{u}) \; d\Gamma \tag{4.39}$$

The function spaces are

$$\boldsymbol{u}, \delta\boldsymbol{u} \in \mathcal{S} \equiv \{\boldsymbol{u} \mid u_i \in H^1(\Omega)\} \tag{4.40}$$

$$\boldsymbol{w}, \delta\boldsymbol{w} \in \mathcal{V} \equiv \{\boldsymbol{w} \mid w_i \in H^1(\Omega)\} \tag{4.41}$$

$$p, \delta p, q, \delta q \in \mathcal{P} \equiv \{p \mid p \in L^2(\Omega), \int_{\Omega} p \; d\Omega = 0\} \tag{4.42}$$

We take derivatives w.r.t each of the Lagrangian's arguments to derive the coupled weak form.

$$D_{\boldsymbol{u}}\mathcal{L} \cdot \delta\boldsymbol{u} + D_p\mathcal{L} \cdot \delta p = \int_{\Omega} \delta\boldsymbol{u} \cdot \boldsymbol{D}(\boldsymbol{u} - \boldsymbol{u}^m) \; d\Omega - \int_{\Omega} q \cdot \nabla\delta\boldsymbol{u} \; d\Omega \tag{4.43}$$

$$+ \int_{\Omega} \nabla \boldsymbol{w} : (-\delta p\boldsymbol{I} + 2\mu \nabla^s \delta\boldsymbol{u}) \; d\Omega - \int_{\Gamma} \boldsymbol{w} \cdot (-\delta p\boldsymbol{I} + 2\mu \nabla^s \delta\boldsymbol{u}) \cdot \boldsymbol{n} \; d\Gamma$$

$$\stackrel{set}{=} 0 \; \forall \; (\delta\boldsymbol{u}, \delta p) \in \mathcal{V} \times \mathcal{P}$$

$$D_{\boldsymbol{w}}\mathcal{L}\cdot\delta\boldsymbol{w}+D_q\mathcal{L}\cdot\delta q=-\int_\Omega \delta q\nabla\cdot\boldsymbol{u}\;d\Omega \tag{4.44}$$

$$+\int_\Omega \nabla\delta\boldsymbol{w}:(-p\boldsymbol{I}+2\mu\nabla^s\boldsymbol{u})\;d\Omega-\int_\Gamma \delta\boldsymbol{w}\cdot(-p\boldsymbol{I}+2\mu\nabla^s\boldsymbol{u})\cdot\boldsymbol{n}\;d\Gamma$$

$$\stackrel{set}{=}\;0\;\forall\;(\delta\boldsymbol{w},\delta q)\in\mathcal{V}\times\mathcal{P}$$

4.3.2 Euler-Lagrange Equations

The derivation of the E-L equations and natural BCs from the weak form is similar to the one seen in the previous section. They end up being:

$$\nabla\cdot\boldsymbol{\sigma}(\boldsymbol{u},p) = \boldsymbol{0}\;,\;\boldsymbol{x}\in\Omega \tag{4.45}$$

$$\nabla\cdot\boldsymbol{\sigma}(\boldsymbol{w},q) = \boldsymbol{D}(\boldsymbol{u}-\boldsymbol{u}^m)\;,\;\boldsymbol{x}\in\Omega \tag{4.46}$$

$$\nabla\cdot\boldsymbol{u} = \boldsymbol{0} \tag{4.47}$$

$$\nabla\cdot\boldsymbol{w} = \boldsymbol{0} \tag{4.48}$$

$$\boldsymbol{w} = \boldsymbol{0}\;,\;\boldsymbol{x}\in\Gamma \tag{4.49}$$

$$\boldsymbol{\sigma}(\boldsymbol{w},q)\cdot\boldsymbol{n} = \boldsymbol{0}\;,\;\boldsymbol{x}\in\Gamma \tag{4.50}$$

4.3.3 Discretization

We now discretize the weak form

$$\{\delta u, \delta p\}^T [M_D] \{u, p\} \longleftrightarrow \int_\Omega \delta u_i^a N_a D_{ij}^c N_c N_b u_j^b \; d\Omega \tag{4.51}$$

$$\{\delta w, \delta q\}^T [K] \{u, p\} \longleftrightarrow \int_\Omega -\delta w_i^a N_{a,j} p^b N_b \delta_{ij} \; d\Omega \tag{4.52}$$

$$+ \int_\Omega 2 w_i^a N_{a,j} \mu^c N_c \nabla^s (\boldsymbol{u}^b N_b)_{ij} \; d\Omega - \int_\Omega \delta q^a N_a u_j^b N_{b,j} \; d\Omega$$

$$\{\delta w, \delta q\}^T [B] \{u, p\} \longleftrightarrow \int_\Gamma \delta w_i^a N_a (-p^b N_b \delta_{ij} + 2\mu^c N_c \nabla^s (\boldsymbol{u}^b N_b)_{ij}) \cdot n_j \; d\Gamma \tag{4.53}$$

$$\{w, q\}^T [K] \{\delta u, \delta p\} \longleftrightarrow \int_\Omega -w_i^a N_{a,j} \delta p^b N_b \delta_{ij} \; d\Omega \tag{4.54}$$

$$+ \int_\Omega 2 w_i^a N_{a,j} \mu^c N_c \nabla^s (\delta \boldsymbol{u}^b N_b)_{ij} \; d\Omega - \int_\Omega q^a N_a \delta u_j^b N_{b,j} \; d\Omega$$

$$= \{\delta u, \delta p\}^T [K]^T \{w, q\}$$

$$\{w, q\}^T [B] \{\delta u, \delta p\} \longleftrightarrow \int_\Gamma w_i^a N_a (-\delta p^b N_b \delta_{ij} + 2\mu^c N_c \nabla^s (\delta \boldsymbol{u}^b N_b)_{ij}) \cdot n_j \; d\Gamma \tag{4.55}$$

$$= \{\delta u, \delta p\}^T [B]^T \{w, q\}$$

The result is the following linear system:

$$\begin{bmatrix} [M_D] & ([K]^T - [B]^T) \\ ([K] - [B]) & \mathbf{0} \end{bmatrix} \begin{Bmatrix} u, p \\ w, q \end{Bmatrix} = \begin{Bmatrix} [M_D] u^m \\ \mathbf{0} \end{Bmatrix} \tag{4.56}$$

4.3.4 Stabilization

The matrix $[M_D]$ (due to the lack of pressure measurements) is singular. The $[K]$ matrix is also singular (due to the incompressibility constraint and the use of linear shape functions). Therefore we add residual-based stabilization similar to that in (Hughes et al., 1986) in the form of H^1 semi-norm penalties. These terms are scaled by a mesh dependent constant τ to maintain consistency. The notation Ω' denotes the union of element interiors.

$$\begin{aligned} \text{SUPG stabilization} &\Rightarrow (-\nabla \cdot \boldsymbol{\sigma}(\boldsymbol{u}, p), \tau(\nabla p - 2\nabla q))_{\Omega'} \\ &= (\nabla p - \underbrace{\nabla \cdot (2\mu \nabla^s \boldsymbol{u})}_{\text{neglect}}, \tau(\nabla p - 2\nabla q))_{\Omega'} \\ &\approx (\nabla p, \tau(\nabla p - 2\nabla q))_{\Omega'} \end{aligned} \tag{4.57}$$

$$\mathcal{L}_{stab} = \frac{1}{2} (\nabla p, \tau(\nabla p - 2\nabla q))_{\Omega'} \tag{4.58}$$

$$\tau = \frac{h^2}{2\mu} \tag{4.59}$$

$$[K_{\text{stab}}] \longleftrightarrow -\int_{\Omega'} \tau N_{a,i} N_{b,i} \, d\Omega \tag{4.60}$$

$$[M_{\text{stab}}] \longleftrightarrow \int_{\Omega'} \tau N_{a,i} N_{b,i} \, d\Omega \tag{4.61}$$

Even though the block matrices in (4.56) are now stabilized, the entire saddle point system remains singular. To address this we use both weak and strong stabilization methods applied in the last section.

4.3.4.1 Forward Problem Results

Weak stabilization Figures (4·10), (4·11), and (4·12) shows results from the weak-stabilized CASE plane strain formulation. Interestingly, these results show considerable error when the exact/noisy displacement fields and the correct modulus are given as input. We suspect that this effect is related to the $[B]$ matrix term. We note that while incorrect, the displacement fields are smooth along the boundary.

Strong stabilization Figures (4·13), (4·14), and (4·15) show the results obtained with the use of strong stabilization. As in plane stress, this approach produced

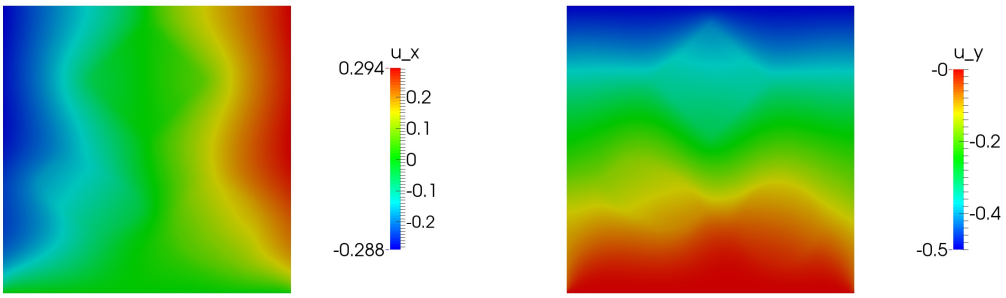

Figure 4·9: Plane strain noiseless $\boldsymbol{u}^m$

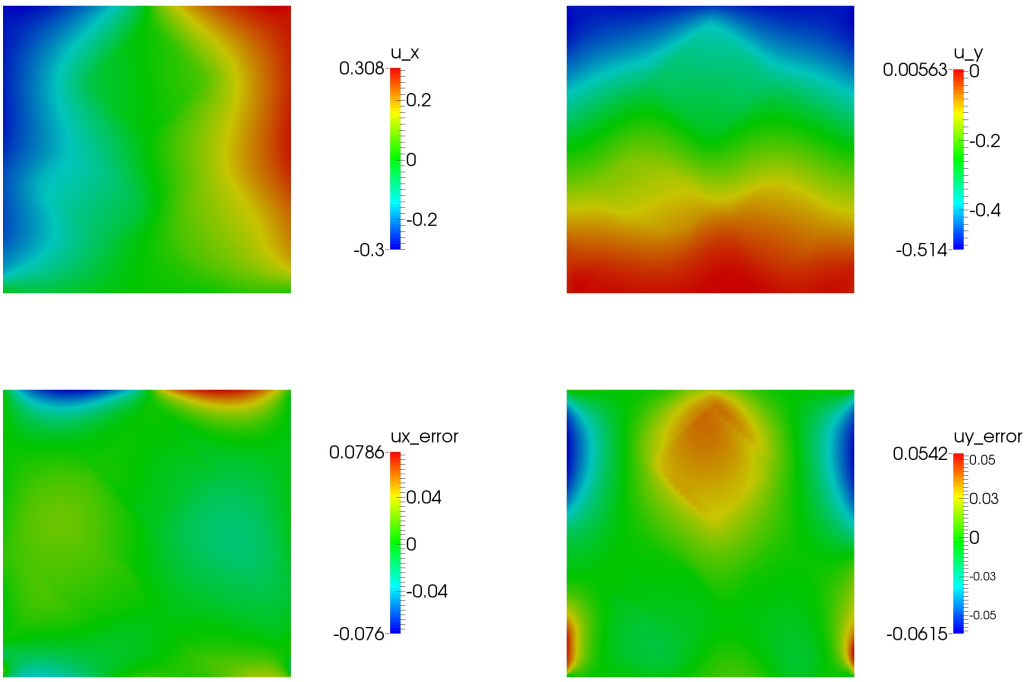

Figure 4·10: Forward plane strain CASE with weak stabilization, exact μ, and noiseless $\boldsymbol{u}^m$ results

displacement estimates that fluctuate on the boundary when the input displacement fields contained noise. Importantly, it can be seen in Figures (4·13) and (4·14) that this approach produced a more accurate estimate of the target displacement field when given the exact modulus than did weak stabilization.

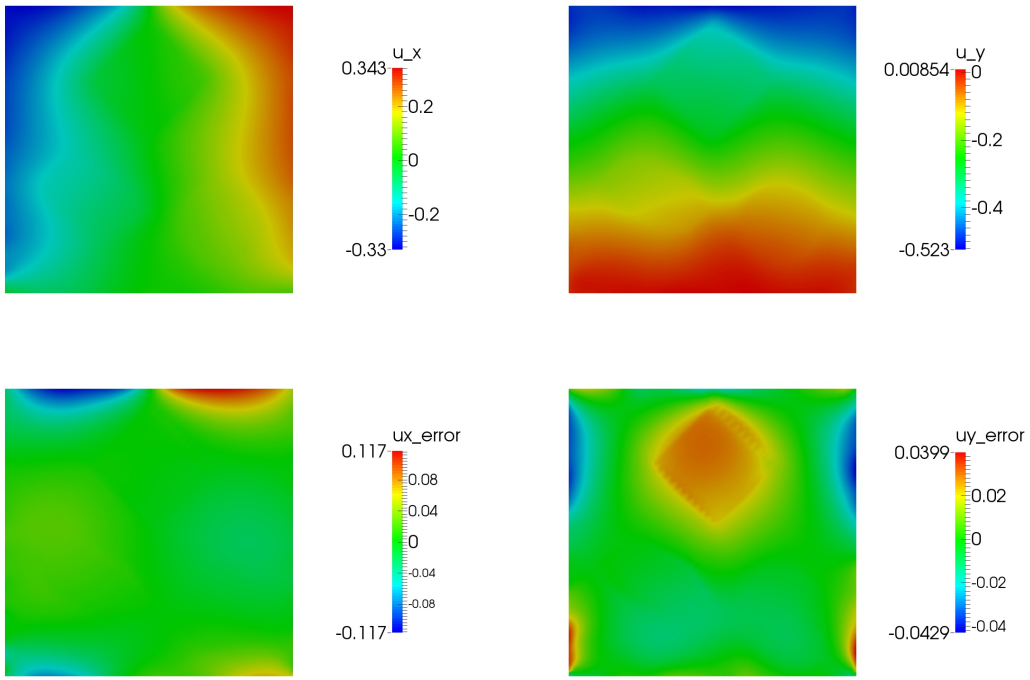

Figure 4·11: Forward plane strain CASE with weak stabilization, exact μ, and noisy $\boldsymbol{u}^m$ results

4.3.5 Inverse Problem Formulation

The material component of the objective function's gradient is given by

$$\{g^e_{\text{mat}}\}_c = \int_\Omega 2w_i^a N_{a,j} N_c \nabla^s(\boldsymbol{u}^b N_b)_{ij}\, d\Omega - \int_\Gamma 2w_i^a N_a N_c \nabla^s(\boldsymbol{u}^b N_b)_{ij} n_j\, d\Gamma. \tag{4.62}$$

One of the terms in the stabilization (4.58) is not multiplied by a Lagrange multiplier ($\boldsymbol{w}$ or q), which implies that it is not associated with the constraint equation. Rather, this term must instead be viewed as a modification of the objective function. Surprisingly, the CASE formulation will produce the same result ($\boldsymbol{u}, \boldsymbol{w}, \mu$, etc.) whether it is included in the evaluation of the objective function or not.

$$\pi[\mu, p] = \pi[\mu] + \frac{1}{2}(\nabla p, \tau \nabla p)_{\Omega'} \tag{4.63}$$

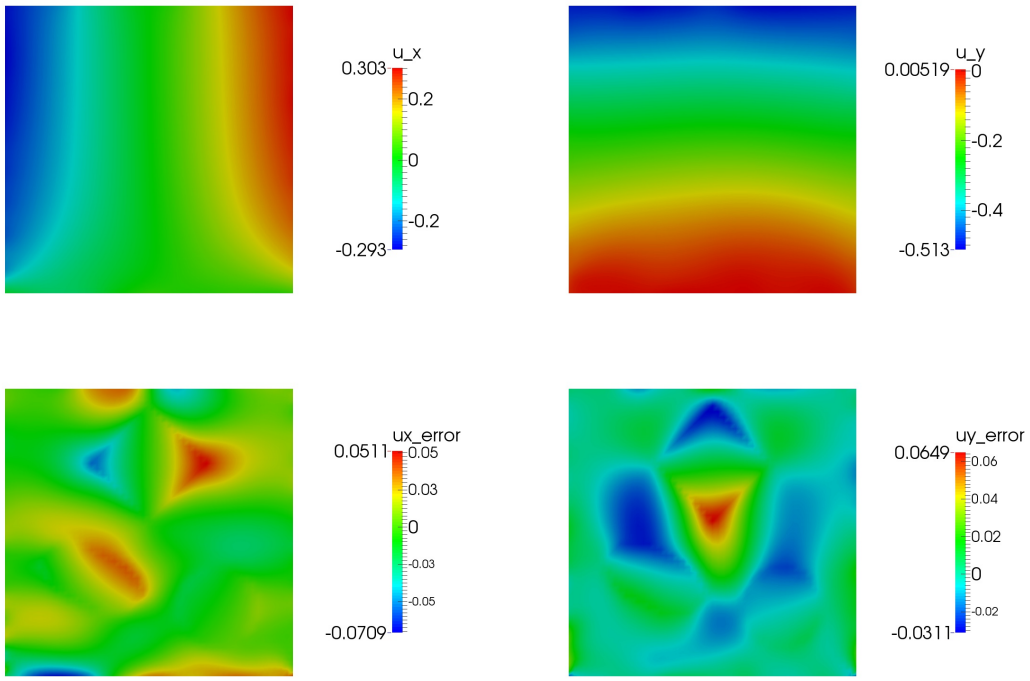

Figure 4·12: Forward plane strain CASE with weak stabilization, $\mu = 1$, and noisy $\boldsymbol{u}^m$ results

The reconstructed modulus fields are shown in Figure (4·16). The solution obtained using the weak stabilization approach contains artifacts not present in the other. Therefore, the strong stabilization method is preferred over the weak approach for plane strain inverse problems (as well as forward problems).

4.4 Incompatible Objective Functions

In this section we introduce an extension of the CASE formulation where the CASE approach is used to define the constraint equation, rather than provide the simultaneous solution of the inverse problem's state and adjoint variables. This formulation has the advantage of being able to use a data match term that differs from the CASE one in the inverse problem. We consider only the strong stabilization approach here.

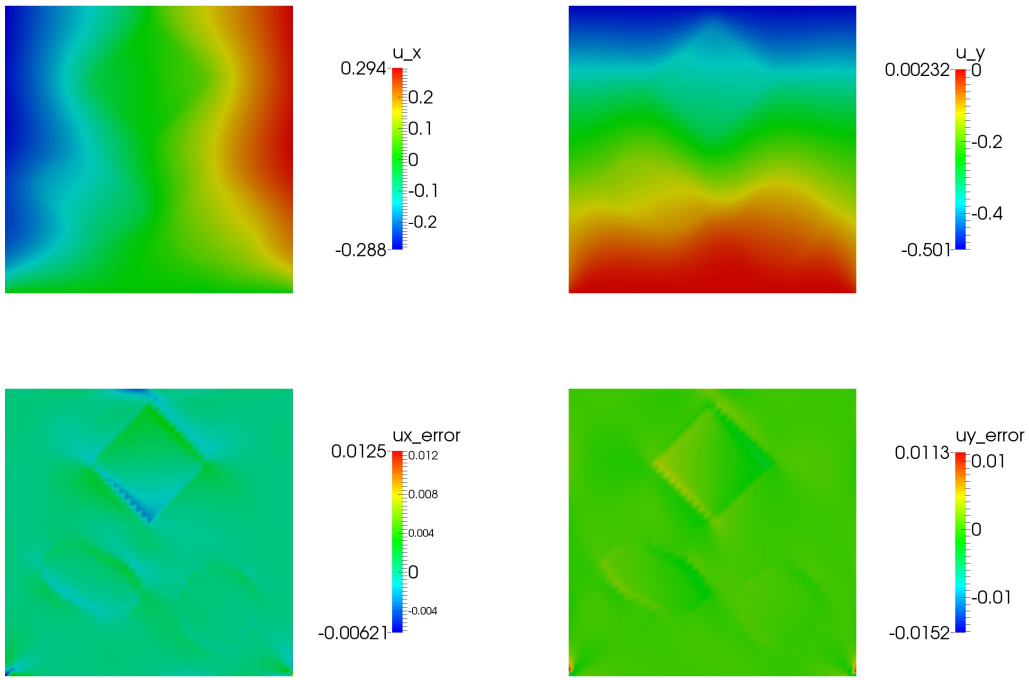

Figure 4·13: Forward plane strain CASE with strong stabilization, exact μ, and noiseless $\boldsymbol{u}^m$ results

$$\mathcal{L}^F[\boldsymbol{w},\boldsymbol{u}] = \frac{1}{2}\left(\boldsymbol{u}-\boldsymbol{u}^m, \boldsymbol{F}(\boldsymbol{u}-\boldsymbol{u}^m)\right)_\Omega + a(\boldsymbol{w},\boldsymbol{u};\mu) \tag{4.64}$$

The CASE Lagrangian (4.64) is used to derive the weak form associated with the constraint equation. This weak form defines a well-posed problem provided the weighting tensor $\boldsymbol{F}$ is positive definite, and in certain cases, for $\boldsymbol{F}$ positive semi-definite. The bilinear form $a(\boldsymbol{w},\boldsymbol{u};\mu)$ is the weak form of the equilibrium equation. We use Greek letters $\boldsymbol{\gamma}$ and $\boldsymbol{\lambda}$ for the adjoint variables. The function spaces for the state and adjoint variables and their weighting functions are

$$\boldsymbol{u}, \delta\boldsymbol{u}, \boldsymbol{\gamma}, \delta\boldsymbol{\gamma} \in \mathcal{S} \quad \equiv \quad \{\boldsymbol{u} \mid u_i \in H^1(\Omega)\} \tag{4.65}$$

$$\boldsymbol{w}, \delta\boldsymbol{w}, \boldsymbol{\lambda}, \delta\boldsymbol{\lambda} \in \mathcal{V} \quad \equiv \quad \{\boldsymbol{w} \mid w_i \in H^1(\Omega), w_i = 0 \text{ on } \Gamma\} \tag{4.66}$$

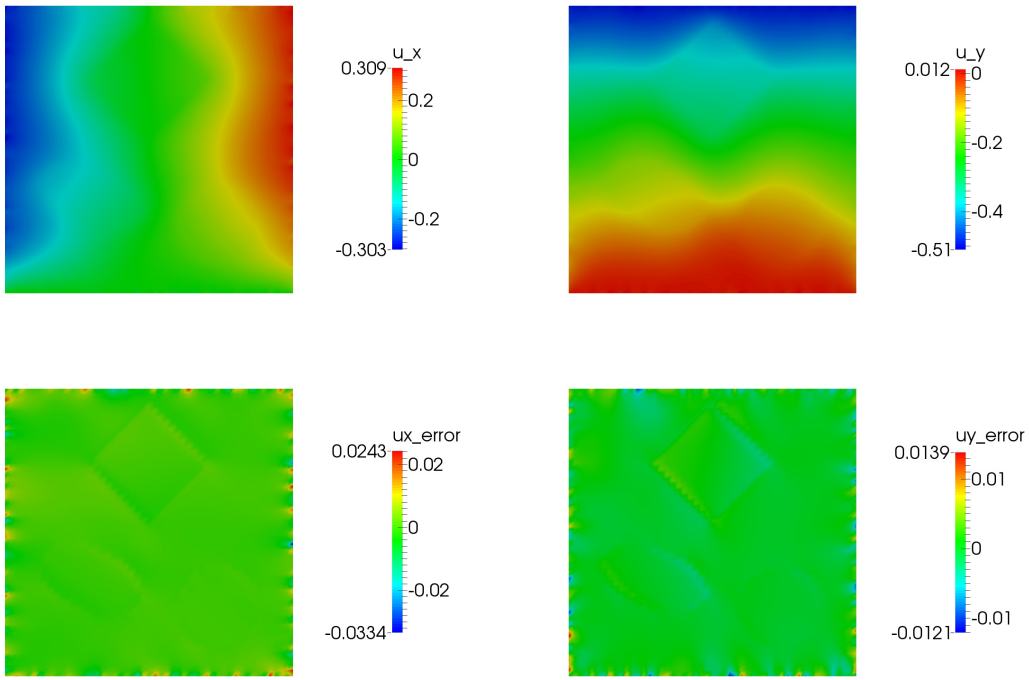

Figure 4·14: Forward plane strain CASE with strong stabilization, exact μ, and noisy $\boldsymbol{u}^m$ results

We take variations of (4.64) to arrive at the following weak forms:

$$D_{\boldsymbol{u}}\mathcal{L}^F \cdot \boldsymbol{\gamma} = (\boldsymbol{\gamma}, \boldsymbol{F}(\boldsymbol{u} - \boldsymbol{u}^m))_\Omega + a(\boldsymbol{w}, \boldsymbol{\gamma}; \mu) \stackrel{set}{=} 0 \;\forall\; \boldsymbol{\gamma} \in \mathcal{S} \tag{4.67}$$

$$D_{\boldsymbol{w}}\mathcal{L}^F \cdot \boldsymbol{\lambda} = a(\boldsymbol{\lambda}, \boldsymbol{u}; \mu) \stackrel{set}{=} 0 \;\forall\; \boldsymbol{\lambda} \in \mathcal{V} \tag{4.68}$$

Equations (4.67) and (4.68) motivate the introduction of the following tetralinear form:

$$b(\boldsymbol{\gamma}, \boldsymbol{\lambda}, \boldsymbol{u}, \boldsymbol{w}; \mu) \equiv (\boldsymbol{\gamma}, \boldsymbol{F}(\boldsymbol{u} - \boldsymbol{u}^m))_\Omega + a(\boldsymbol{w}, \boldsymbol{\gamma}; \mu) + a(\boldsymbol{\lambda}, \boldsymbol{u}; \mu) \tag{4.69}$$

The inverse problem can use an entirely different data match term from the one present in (4.64). For demonstration purposes we choose a least squares term with an arbitrary $\boldsymbol{D}$ weighting tensor.

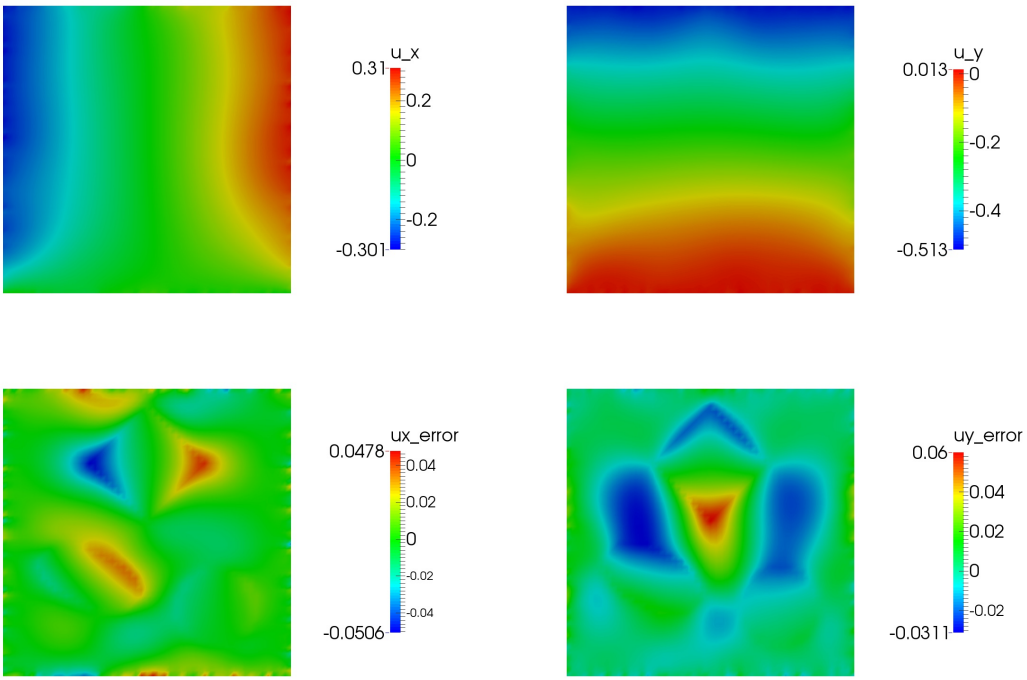

Figure 4·15: Forward plane strain CASE with strong stabilization, $\mu = 1$, and noisy $\boldsymbol{u}^m$ results

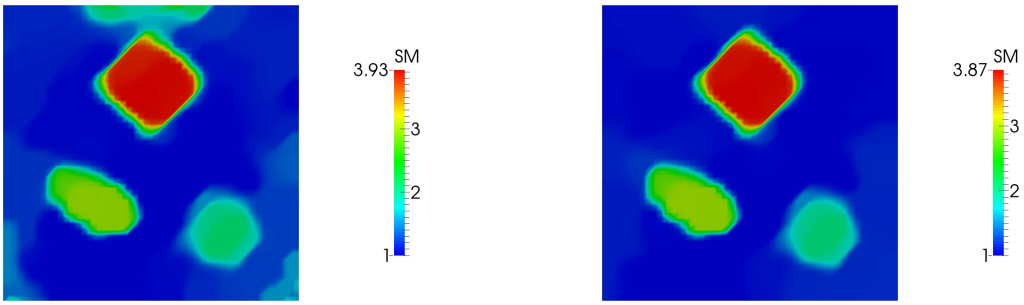

Weak stabilization Strong stabilization

Figure 4·16: Reconstructed μ for each plane strain CASE formulation

$$\mathcal{L}^D(\boldsymbol{\gamma}, \boldsymbol{\lambda}, \boldsymbol{u}, \boldsymbol{w}, \mu) = \frac{1}{2}\left(\boldsymbol{u} - \boldsymbol{u}^m, \boldsymbol{D}(\boldsymbol{u} - \boldsymbol{u}^m)\right) + \alpha\mathcal{R}[\mu] + b(\boldsymbol{\gamma}, \boldsymbol{\lambda}, \boldsymbol{u}, \boldsymbol{w}; \mu) \qquad (4.70)$$

The forward problem is determined by taking variations of (4.70) w.r.t the adjoint variables

$$D_{\boldsymbol{\gamma}}\mathcal{L}^D \cdot \delta\boldsymbol{\gamma} + D_{\boldsymbol{\lambda}}\mathcal{L}^D \cdot \delta\boldsymbol{\lambda} = b(\delta\boldsymbol{\gamma}, \delta\boldsymbol{\lambda}, \boldsymbol{u}, \boldsymbol{w}, \mu) \stackrel{set}{=} 0 \ \forall \ (\delta\boldsymbol{\gamma}, \delta\boldsymbol{\lambda}) \in \mathcal{S} \times \mathcal{V} \tag{4.71}$$

The discrete form of the forward problem (borrowing notation from the previous sections) is as follows. The vectors of nodal coefficients for $\{w\} \in \mathbb{R}^n$ is strictly smaller in length than that for $\{u\} \in \mathbb{R}^m$ due to the essential boundary conditions of $\mathcal{V}^h \subset \mathcal{V}$. Correspondingly, the K matrices are not square.

$$\begin{bmatrix} [M_F] & [K]^T \\ [K] & \mathbf{0} \end{bmatrix} \begin{Bmatrix} u \\ w \end{Bmatrix} = \begin{Bmatrix} [M_F]u^m \\ \mathbf{0} \end{Bmatrix} \tag{4.72}$$

The adjoint problem is obtained by taking variations of (4.70) w.r.t. the state equation variables

$$\begin{aligned} D_{\boldsymbol{u}}\mathcal{L}^D \cdot \delta\boldsymbol{u} &= (\delta\boldsymbol{u}, \boldsymbol{D}(\boldsymbol{u} - \boldsymbol{u}^m))_\Omega + (\boldsymbol{\gamma}, \boldsymbol{F}\delta\boldsymbol{u})_\Omega + a(\boldsymbol{\lambda}, \delta\boldsymbol{u}; \mu) && (4.73) \\ &\stackrel{set}{=} 0 \ \forall \ \delta\boldsymbol{u} \in \mathcal{S} \\ D_{\boldsymbol{w}}\mathcal{L}^D \cdot \delta\boldsymbol{w} &= a(\delta\boldsymbol{w}, \boldsymbol{\gamma}; \mu) \stackrel{set}{=} 0 \ \forall \ \delta\boldsymbol{w} \in \mathcal{V} && (4.74) \end{aligned}$$

The block matrix present in the discrete adjoint system is the transpose of the one in (4.72). The matrices are, however, identical because M_F is a symmetric matrix. Thus, the forward and adjoint systems differ only in their rhs.

$$\begin{bmatrix} [M_F]^T & [K]^T \\ [K] & \mathbf{0} \end{bmatrix} \begin{Bmatrix} \gamma \\ \lambda \end{Bmatrix} = \begin{Bmatrix} -[M_D](u - u^m) \\ \mathbf{0} \end{Bmatrix} \tag{4.75}$$

To determine the gradient, we examine the total differential of $\mathcal{L}^D$ and note that only the μ variation term is non-zero.

$$\delta\mathcal{L}^D = \cancel{D_{\boldsymbol{\gamma}}\mathcal{L}^D \cdot \delta\boldsymbol{\gamma}} + \cancel{D_{\boldsymbol{\lambda}}\mathcal{L}^D \cdot \delta\boldsymbol{\lambda}} \tag{4.76}$$
$$+ \cancel{D_{\boldsymbol{u}}\mathcal{L}^D \cdot \delta\boldsymbol{u}} + \cancel{D_{\boldsymbol{w}}\mathcal{L}^D \cdot \delta\boldsymbol{w}} + D_\mu\mathcal{L}^D \cdot \delta\mu$$
$$D_\mu\mathcal{L}^D \cdot \delta\mu = a(\boldsymbol{w}, \boldsymbol{\gamma}, \delta\mu) + a(\boldsymbol{\lambda}, \boldsymbol{u}, \delta\mu) + \alpha D_\mu\mathcal{R} \cdot \delta\mu \tag{4.77}$$

Summary - to perform an iteration of the inversion algorithm using this method, one first solves (4.72), evaluates the objective function, then solves (4.75), and lastly evaluates the gradient according to (4.77). Note that the size of the linear systems is nearly twice the size of those present in the assumed BCs or springs approaches to solving the inverse problem.

4.4.1 CASE as a Special Case

We now show that when $\boldsymbol{D} = \boldsymbol{F}$, this formulation will produce the same results as CASE. Recall the CASE gradient, and the forward and adjoint problems for this formulation (see equations (4.71), (4.73), and (4.74)).

$$D_\mu\mathcal{L}^{\text{CASE}} \cdot \delta\mu = a(\boldsymbol{w}, \boldsymbol{u}; \delta\mu) + \alpha D_\mu\mathcal{R} \cdot \delta\mu \tag{4.78}$$

Expanding (4.71) using (4.69) yields

$$(\delta\boldsymbol{\gamma}, \boldsymbol{F}(\boldsymbol{u} - \boldsymbol{u}^m))_\Omega + a(\boldsymbol{w}, \delta\boldsymbol{\gamma}, \mu) + a(\delta\boldsymbol{\lambda}, \boldsymbol{u}, \mu) = 0 \;\forall\; (\delta\boldsymbol{\gamma}, \delta\boldsymbol{\lambda}) \in \mathcal{S} \times \mathcal{V} \tag{4.79}$$

We combine equations (4.73) and (4.74) to produce

$$(\boldsymbol{\gamma}, \boldsymbol{F}\delta\boldsymbol{u})_\Omega + a(\boldsymbol{\lambda}, \delta\boldsymbol{u}, \mu) + (\delta\boldsymbol{u}, \boldsymbol{D}(\boldsymbol{u} - \boldsymbol{u}^m))_\Omega \tag{4.80}$$
$$+ a(\delta\boldsymbol{w}, \gamma, \mu) = 0 \;\forall\; (\delta\boldsymbol{u}, \delta\boldsymbol{w}) \in \mathcal{S} \times \mathcal{V}$$

We make the substitutions $\mathbf{0} \leftarrow (\delta\boldsymbol{\lambda}, \delta\boldsymbol{w})$ in (4.79) and (4.80), and $\delta\boldsymbol{u} \leftarrow \delta\boldsymbol{\gamma}$ in (4.79) to arrive at

$$(\delta\boldsymbol{u}, \boldsymbol{F}(\boldsymbol{u} - \boldsymbol{u}^m)_\Omega + a(\boldsymbol{w}, \delta\boldsymbol{u}; \mu) = 0 \;\forall\; \delta\boldsymbol{u} \in \mathcal{S} \tag{4.81}$$

$$(\boldsymbol{\gamma}, \boldsymbol{F}\delta\boldsymbol{u}) + a(\boldsymbol{\lambda}, \delta\boldsymbol{u}; \mu) + (\delta\boldsymbol{u}, \boldsymbol{D}(\boldsymbol{u} - \boldsymbol{u}^m))_\Omega = 0 \;\forall\; \delta\boldsymbol{u} \in \mathcal{S} \tag{4.82}$$

Now we choose $\boldsymbol{D} = \boldsymbol{F}$ and subtract (4.81) from (4.82)

$$(\boldsymbol{\gamma}, \boldsymbol{F}\delta\boldsymbol{u})_\Omega + a(\boldsymbol{\lambda} - \boldsymbol{w}, \delta\boldsymbol{u}; \mu) = 0 \;\forall\; \delta\boldsymbol{u} \in \mathcal{S} \tag{4.83}$$

We find that (4.83) is satisfied identically by the fields

$$\boldsymbol{\gamma} = \mathbf{0} \tag{4.84}$$

$$\boldsymbol{\lambda} = \boldsymbol{w} \tag{4.85}$$

We use equations (4.84) and (4.85) in (4.77) to obtain

$$\begin{aligned} D_\mu \mathcal{L}^D \cdot \delta\mu &= \cancel{a(\boldsymbol{w}, \boldsymbol{\gamma}, \delta\mu)} + a(\boldsymbol{w}, \boldsymbol{u}, \delta\mu) + \alpha D_\mu \mathcal{R} \cdot \delta\mu \\ &= D_\mu \mathcal{L}^{\mathrm{CASE}} \cdot \delta\mu \end{aligned} \tag{4.86}$$

Chapter 5

Applications

5.1 Introduction

In this chapter, we present several applications of BMI that were enabled by the formulations presented in earlier chapters. In the first section, we present results showing reconstructed material property distributions within a single cell. This work represents the first application of BMI at this length scale. This application utilized the Bayesian springs approach to fix rigid body displacements in the forward problem.

The second application is a validation study based on deformation of a tissue-mimicking phantom. The phantom was gently compressed, and the 2D displacement fields within the phantom were measured via US and image registration. This application uses the CASE approach and validates its use with plane models in similar contexts.

The third application described concerns deformation of a tissue mimicking phantom measured in 3D. The geometry of the measurements requires special treatment, and we demonstrate that both the Bayesian springs and CASE approaches provide substantial improvements over an approach based on assumed boundary conditions.

Finally, we demonstrate the application of the CASE method to a set of data collected clinically. The clinical data includes US-measured deformation fields in ten breast masses, five of which are benign fibroadenomas, and five of which are malignant invasive ductal carcinomas (the most common breast cancer). These results demonstrate the feasibility of using the methods and software framework presented

herein to problems of current clinical interest.

5.2 Cell BMI

The mechanical properties of cells are of interest in a number of biological processes, such as cell migration, wound healing, and growth. Several techniques have been invented to probe mechanical properties at the cellular scale. Some include micropipette aspiration, PDMS-based beams, optical tweezers, magneto-rheology, and AFM (Suresh, 2007). These techniques often make a trade between spatial and temporal resolution. For example, micropipette aspiration estimates a single value for the modulus of the entire cell and can be done quickly, while AFM is capable of producing spatial modulus maps but experiments require minutes to perform and the experiment is performed in an unnatural environment.

BMI can be applied to single cells and cell clusters provided measurements of deformation and forcing are available. This technique is capable of creating shear modulus maps with subcellular resolution, and the experiment can be performed in less than a minute. The cell data was collected by Michael Smith's group at Boston University. The approach and methods discussed in this section lead to the publications (Canović et al., 2014a) and (Canović et al., 2014b).

5.2.1 Experiment

In a cell BMI experiment (see Figure 5·1), a cell is placed on a polyacrylamide gel layer imprinted with a regular grid of flourescently-labeled fibronectin dots(B,G; green). The cell adheres to the dots and pulls them inwards while not attaching to the gel's surface. The Young's modulus and Poisson's ratio of the gel are known. The cell body is seeded with 500 nm florescent microbeads (B,G; blue). Brightfield (C,H) and florescent channel (D,I and E,J) images are acquired using a confocal microscope

(A). A uni-axial deformation of approximately 8-12 % strain is applied by pushing a parallel plate indenter into the gel (F). Post-deformation images are then acquired.

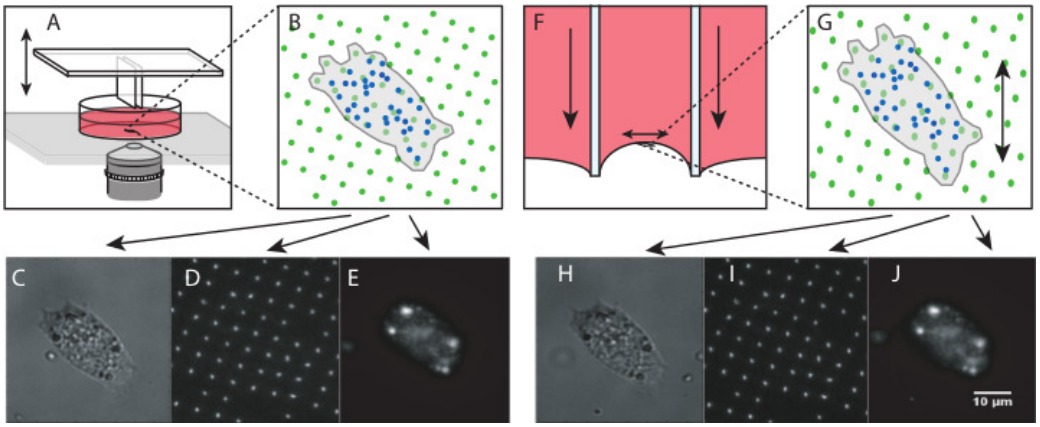

Figure 5·1: Cell BMI experiment (Canović et al., 2014b)

Point measurements of cell displacement are obtained by tracking beads in the pre and post deformation images. The motion of the fibronectin dots between images is also quantified and used in combination with the known mechanical properties of the gel substrate to estimate the force exerted by the cell on the substrate due to the applied deformation. The position of the dots prior to the cell pulling them inwards is also known, and thus the cellular traction force prior to deformation can be estimated.

Due to measurement noise, the cell's measured net force and moment are non-zero. A least squares balancing procedure is used to solve for the forces closest to the measurements that satisfy equilibrium. These balanced forces are used to drive the forward problem. The cell's boundary condition is traction-free. Lack of Dirichlet BCs motivates the use of lumped weak spring elements to constrain rigid body motion in the forward problem.

The cell is modeled using the linear incompressible plane stress formulation discussed in appendix A. The cellular traction forces are treated as a lumped body force term. A mesh of the cell (Figure 5·2) that contains the locations of the displacement

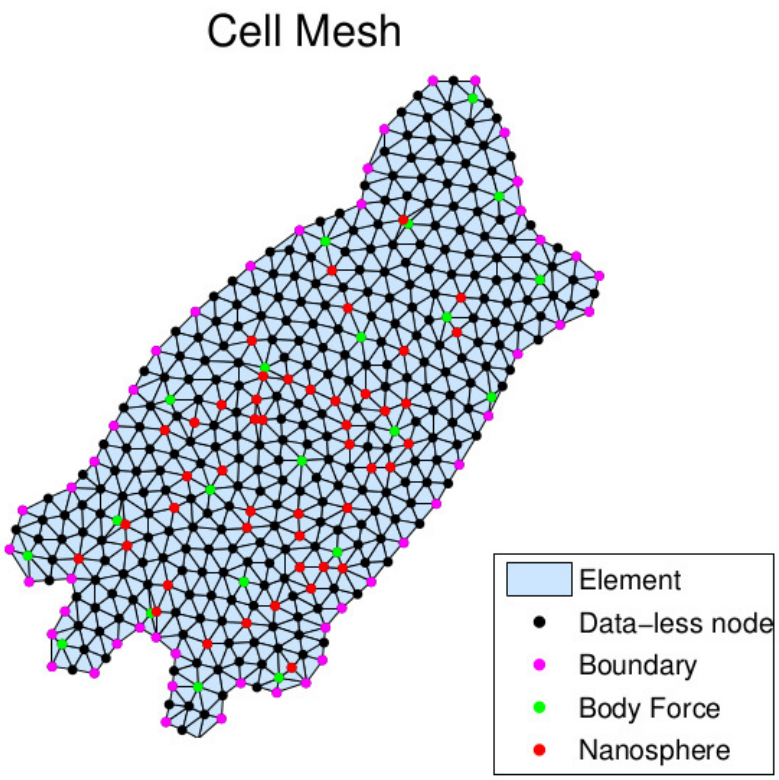

Figure 5·2: Distmesh generated FEM mesh

measurements and body forces is generated using the program Distmesh (Persson and Strang, 2004).

Cell height can be estimated using the height of the beads. The inversion process yields the shear modulus integrated through the cell thickness. The local shear modulus can be obtained by accounting for local cell thickness. The stress present in the cell prior to deformation (prestress) can be computed with a post-processing element that loads the cell with the forces measured prior to deformation.

5.2.2 Results

Heterogeneous shear modulus maps and prestress results for a single cell are shown in Figure (5·3). Both height-averaged (C,D) and height-corrected (F,G) reconstructions

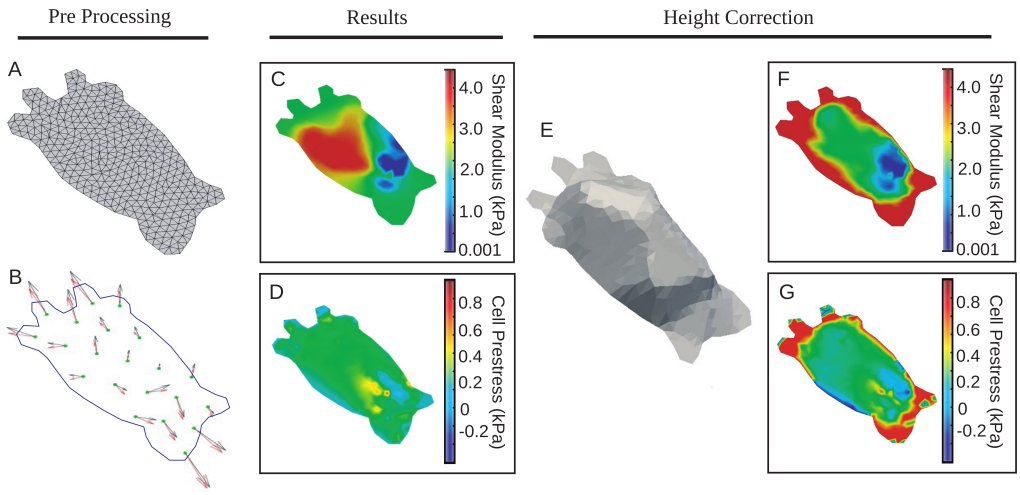

Figure 5·3: Cell BMI inputs and outputs (Canović et al., 2014b)

are given. Cell height is lowest at the boundary (E) due to lack of beads there. As a result, the height-corrected modulus is artificially stiff near the cell boundary.

5.2.3 Discussion

The cell BMI data is challenging to analyze for several reasons. First, the measured displacement field is known only at the location of the beads, and the beads themselves are not always firmly anchored to the cell. Second, the least squares force balancing procedure introduces error into the force measurements. Finally, there is no currently accepted gold standard of cellular modulus field estimation to compare our results to, and cell-sized imaging phantoms that are suitable for use in a cell BMI experiment do not exist. The publications (Canović et al., 2014a) and (Canović et al., 2014b) resulted from this study.

5.3 2D US Phantom

This section contains results from an ultrasound phantom study. 2D displacement fields were estimated from RF ultrasound images and analyzed using plane stress and

plane strain CASE approaches. This data was acquired by Timothy Hall's group at the University of Wisconsin, Madison.

5.3.1 Experiment

The experimental sample is a tissue-mimicking agar-gelatin 100 mm cube US phantom containing four coplanar 10mm diameter spherical inclusions (targets). The procedures used to create, characterize the mechanical properties, and measure the displacement due to compression of the phantom are documented in (Pavan et al., 2012) and (Dord et al., 2015).

The shear modulus of each inclusion and the background phantom material were controlled by varying the composition of agar and gelatin in each component. Formalin was added to to the gelatin to promote cross-linking and increase melting point and stiffness. Glass beads were also incorporated into the phantom material to act as acoustic scatters to enable the acquisition of US images.

Test cylinders were made of the material that constituted each inclusion and the background. These cylinders were subject to quasi-static mechanical compression tests where force vs load curves were measured. The data from these experiments was fit to a Veronda-Westmann model in order to characterize the linear elastic and nonlinear material properties of each component. The shear modulus relative to the background (set to 1) for each target is given in Table (5.1).

Table 5.1: 2D phantom measured contrast

Target	1	2	3	4
Reference Contrast	2.83	2.27	3.54	5.26

The phantom was compressed in increments of 1.5% strain up to $\approx$ 20% strain using a compression plate with dimensions much greater than those of the phantom

with the goal of imposing uniaxial compression loads. After each load step, RF data was acquired using a linear array US transducer.

A modified block-matching algorithm (Jiang and Hall, 2011) was used to determine the incremental displacement between each RF image. The data presented in this section is from the lowest strain level (1.5%), as the CASE approaches assume small deformation and reconstructs the shear modulus (a linear elastic material property). Margins were applied to the data to remove noisy regions near the boundaries of the measured displacement field. Finally, the data was downsampled by a factor of 4 in each direction to reduce the inversion algorithm's runtime. The measured displacement field for Target 1 is shown in Figure (5·4) to serve as a representative example of the input inverse problem data for this dataset.

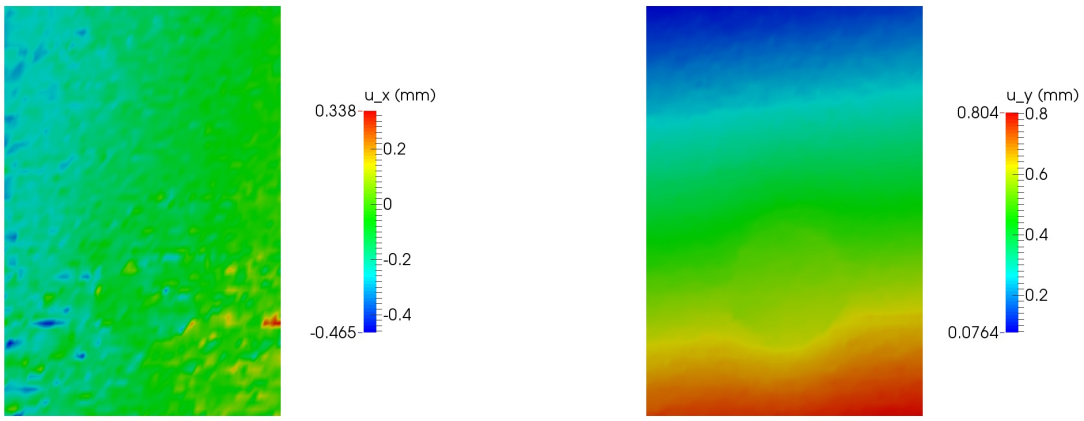

Figure 5·4: Target 1 measured displacement field $\boldsymbol{u}^m(\boldsymbol{x})$

5.3.2 Results

Here we present results obtained using plane stress and plane strain CASE approaches. The reconstructed shear moduli images are shown in Figures (5·5) and (5·7), respectively. The components of the $\boldsymbol{T}$ weighting tensor were chosen as follows: $T_{xx} = 0.1$, $T_{xy} = 0$, and $T_{yy} = 1$.

We found a different regularization constant α was required for each target, prob-

ably because the SNR for each phantom differed due to the unique stiffness of each inclusion. The regularization constants used are reported in Table (5.2).

Table 5.2: Regularization parameter used in 2D phantom study results

Target	1	2	3	4
α	5.0e-5	6.0e-5	4.0e-5	9.0e-6

Images of the predicted minus the measured lateral component of displacement (u_x) for each approach are displayed in Figures (5·6) and (5·8). These images have been scaled to $+/-$ 0.1 mm.

5.3.3 Discussion

Both the plane stress and plane strain results show a stiff circular inclusion embedded in a less stiff background. There are differences, however, in the reconstructed stiffness and shape of each Target. The background in each reconstruction is not totally homogeneous, but the degree of variation present is less than the level observed when a plane stress assumed BCs approach was used to analyze this data (Dord et al., 2015). The observed mechanical contrast is higher as well, likely due to the absence of BC influence and the use of a log μ approach.

The displacement mismatch figures suggest that plane stress is a more appropriate material model for this dataset. We note that the variation in Figure (5·8) is much more systematic than that present in Figure (5·6).

5.4 3D US Phantom

In this section we present results from a 3D ultrasound phantom compression experiment. Both the spring BCs and CASE approaches were applied to this dataset. This

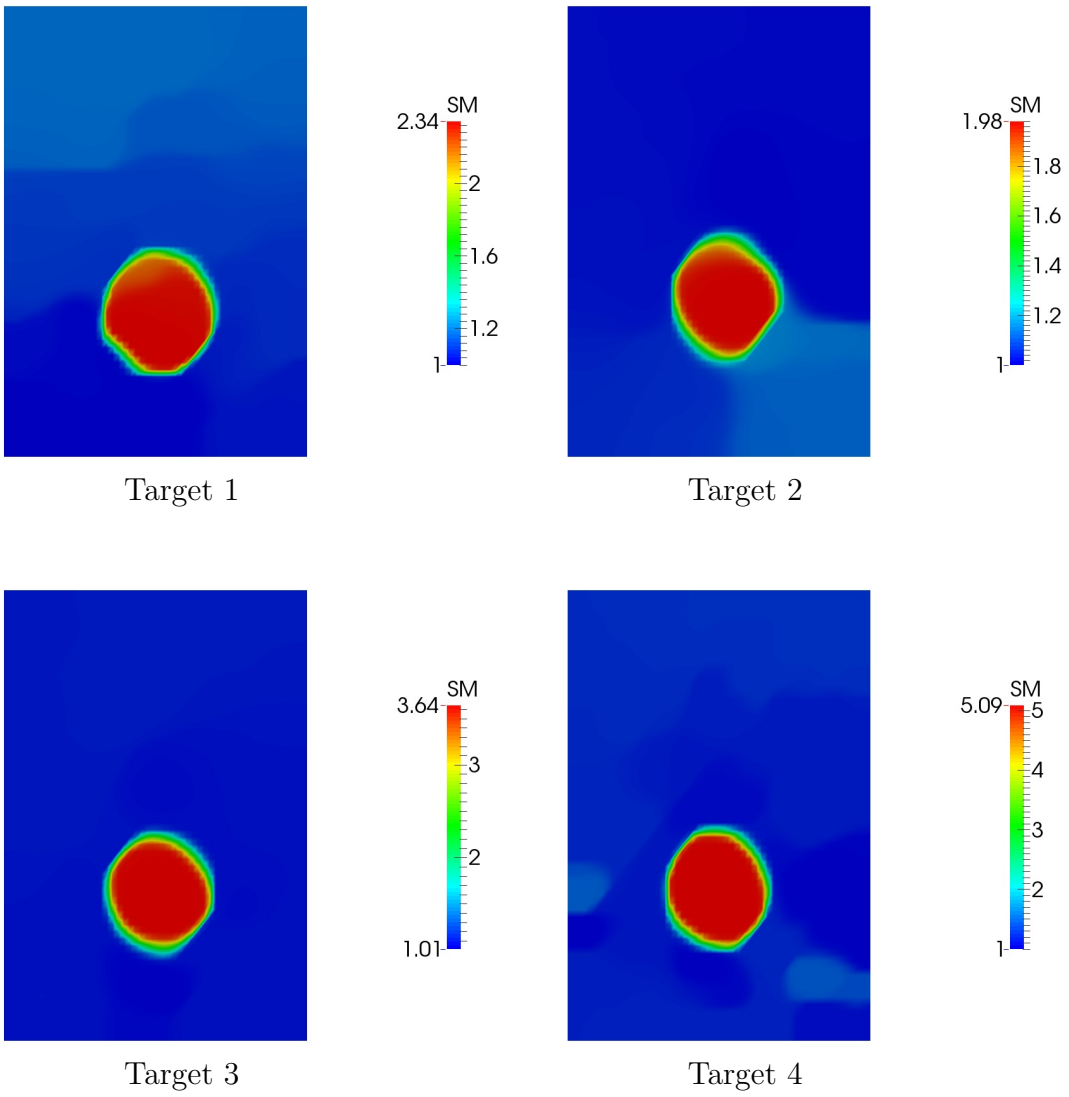

Figure 5·5: CASE plane stress phantom results

data was provided to us by Jeff Bamber's group at the Institute for Cancer Research, London, UK.

5.4.1 Slip Imaging

Characterization of the interface between a tumor and its surroundings is of interest to clinicians. Certain kinds of brain tumors have a slippery interface, and knowledge of such an interface could be useful in planning margins for surgical resection of the

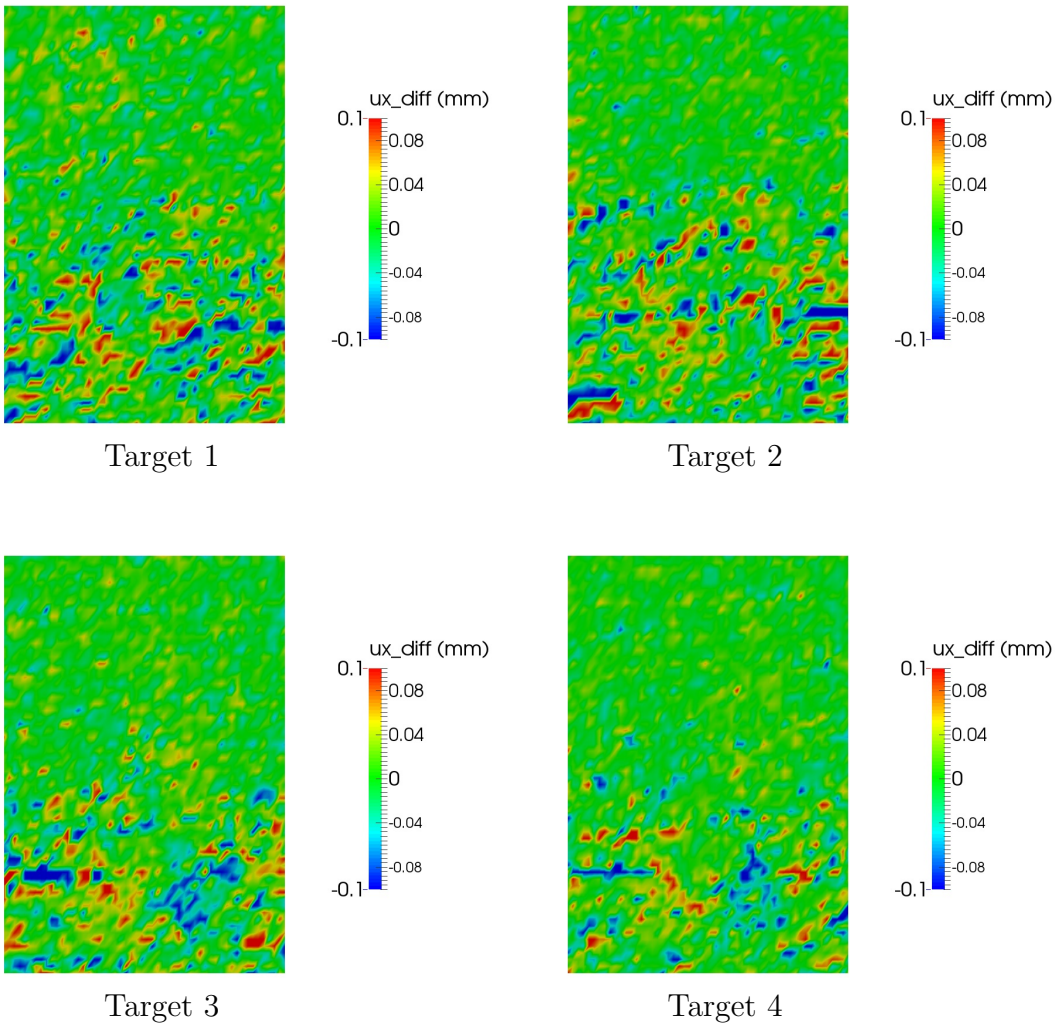

Figure 5·6: CASE plane stress u_x (scaled) mismatch

tumor. In the context of breast elasticity imaging, FAs tend to more mobile than malignant tumors such as IDCs, and thus the presence of slip layers could be used to diagnose tumor type.

Past studies of slip layers (Chakraborty et al., 2012), (Garcia et al., 2009), and (Konofagou et al., 2000) have focused on measuring shear strain or "axial shear strain" between inclusions and their background. It is hypothesized that a slip layer could manifest as a region of very low shear modulus. We present a result in this section that supports this hypothesis.

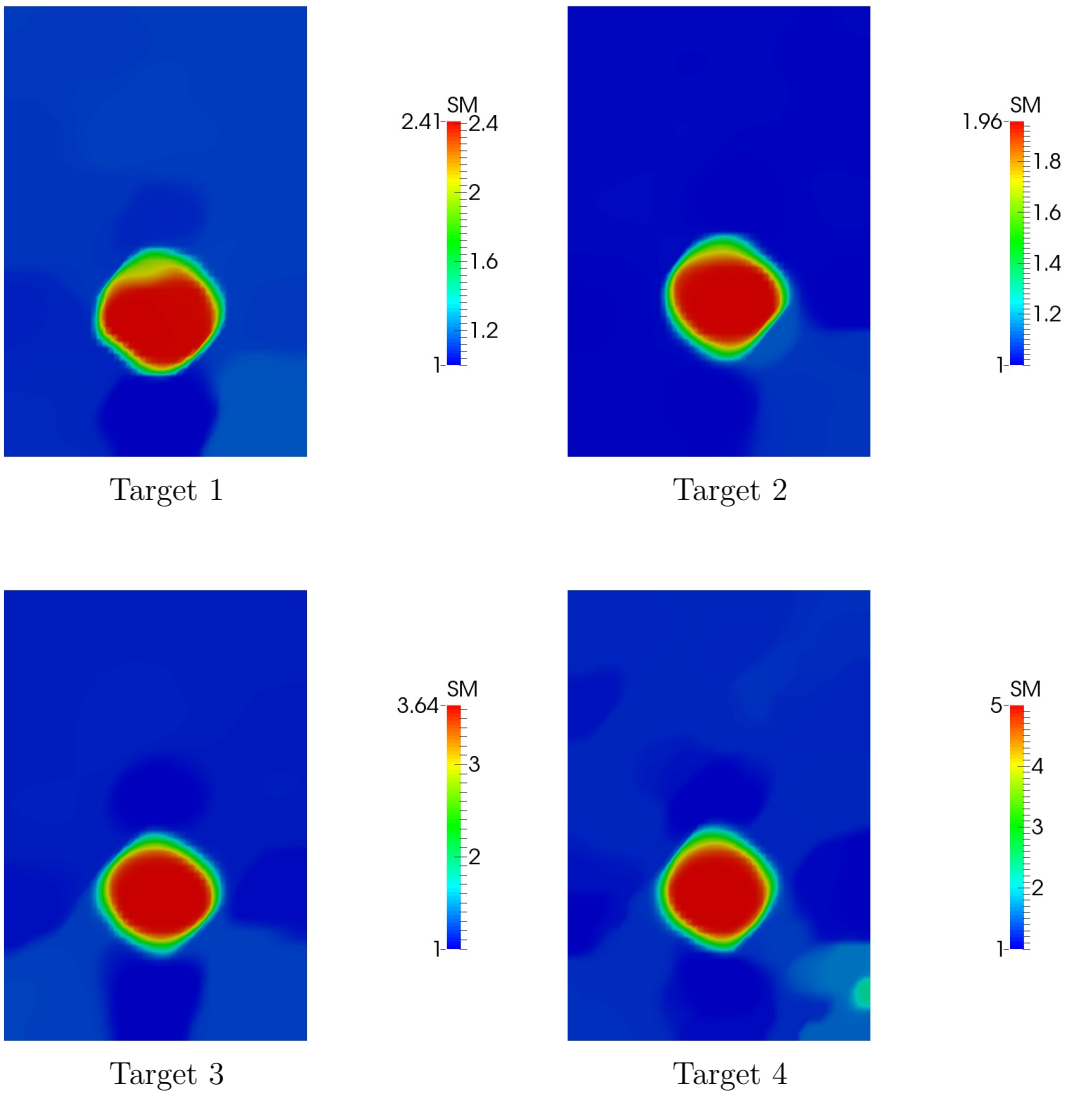

Target 1 Target 2

Target 3 Target 4

Figure 5·7: CASE plane strain phantom results

5.4.2 Experiment

The 3D phantom data was collected using a mechanically swept linear US transducer (sometimes referred to as a "wobbler"). As a result, the direction of sound propagation varies throughout the imaging volume and the computational domain is non-rectangular (see Figure (5·9)), unlike the rest of the data examined in this thesis.

The gelatin ultrasound phantom used in the experiment contained a spherical

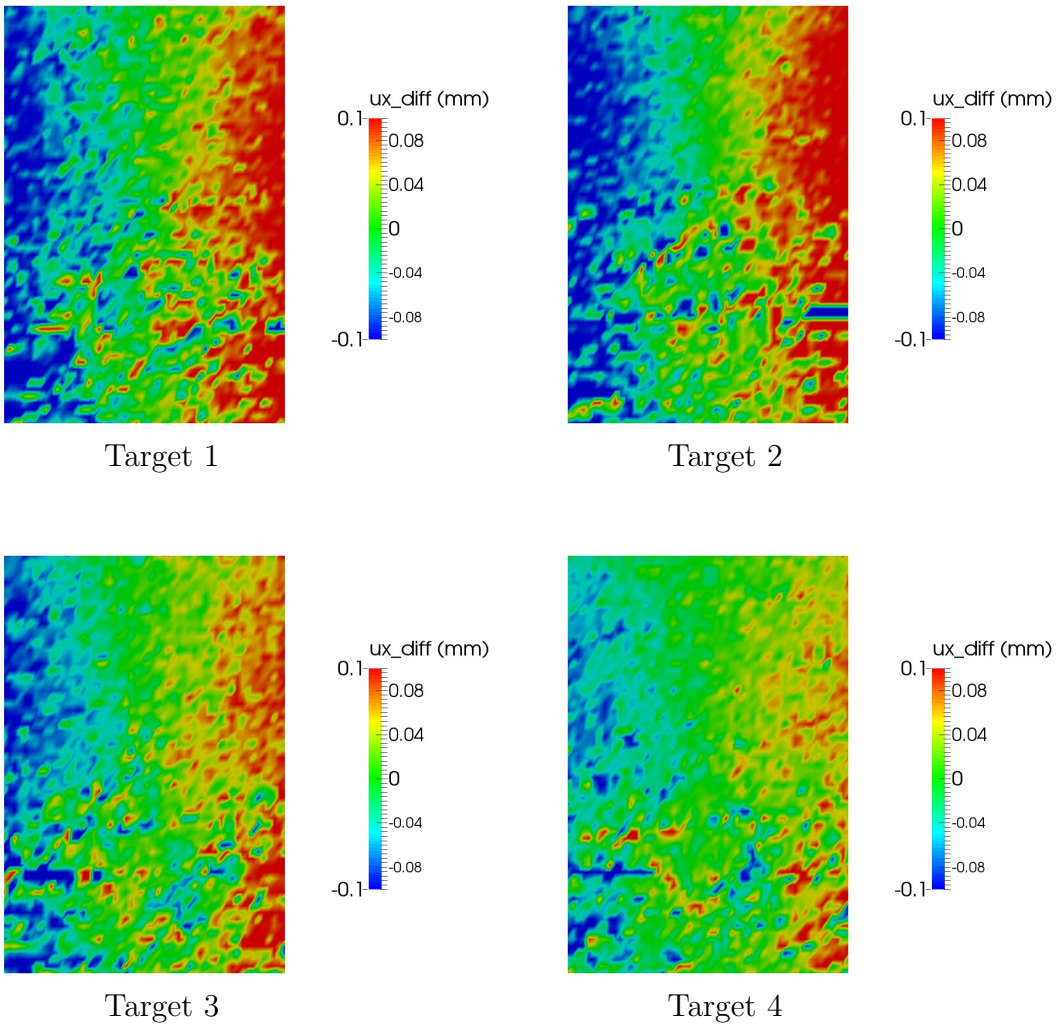

Figure 5·8: CASE plane strain u_x (scaled) mismatch

inclusion composed of 14% gelatin (by weight) embedded in a 6% gelatin background. Mechanical tests on the phantom estimated the Young's modulus of the inclusion and the background to be 4 and 1 kPa, respectively. Water was injected between the inclusion and the background to lubricate the interface between the two materials as to promote slip behavior.

In the experiment, the phantom was compressed in 5 1% strain increments. At each loading step, a RF image was acquired at a sampling rate of 66.6 MHz using a Gage Compuscope 14200 inside a PC running Stradwin 4.6 software (Housden et al.,

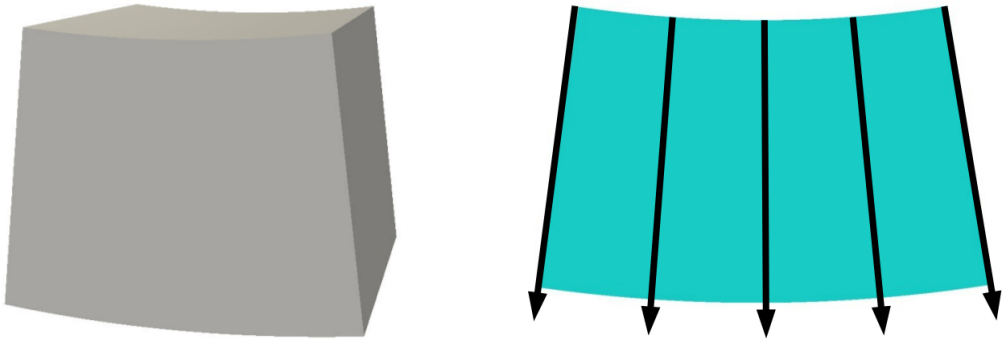

Image volume Directions of sound propagation

Figure 5·9: Axial direction depends on location in the computational domain

2010) interfaced to a Diasus ultrasound scanner (Dynamic Imaging, UK) and a GE RSP 6-12 MHz 4D probe. The results presented in Figures (5·10)-(5·13) used the displacement field from the first to second increment.

5.4.3 Methods

As mentioned previously, displacements measured using US imaging are most precise in the direction of sound propagation $\hat{\boldsymbol{e}}_{axial}(\boldsymbol{x})$. For displacement data collected using a linear array, this direction coincides with the y direction of the Cartesian coordinate system the inverse problem is solved in. When displacements are measured using a mechanically swept linear array, the direction of sound propagation varies throughout the volume, as illustrated in Figure (5·9).

There are two places in the formulation of the inverse problem where direction of sound propagation can be taken into account: The $\boldsymbol{T}$ tensor of the objective function and the spring tensor $\boldsymbol{K}$.

$$\boldsymbol{T}(\boldsymbol{x}) = \hat{\boldsymbol{e}}_{axial}(\boldsymbol{x}) \otimes \hat{\boldsymbol{e}}_{axial}(\boldsymbol{x}) \tag{5.1}$$

$$\boldsymbol{K}(\boldsymbol{x}) = \kappa \boldsymbol{T}(\boldsymbol{x}) \tag{5.2}$$

Two reconstructions were performed using the same displacement field and a $\boldsymbol{T}$ tensor computed according to (5.1). The first used the 3D analog of the assumed BCs approach used in the simulated data reconstructions (u_y Dirichlet, homogeneous Neumann in x and z) while the second used spring boundary conditions with a $\boldsymbol{K}$ given by equation (5.2) with κ equal to 100. The regularization constant used in all reconstructions for this section was equal to 4E-5.

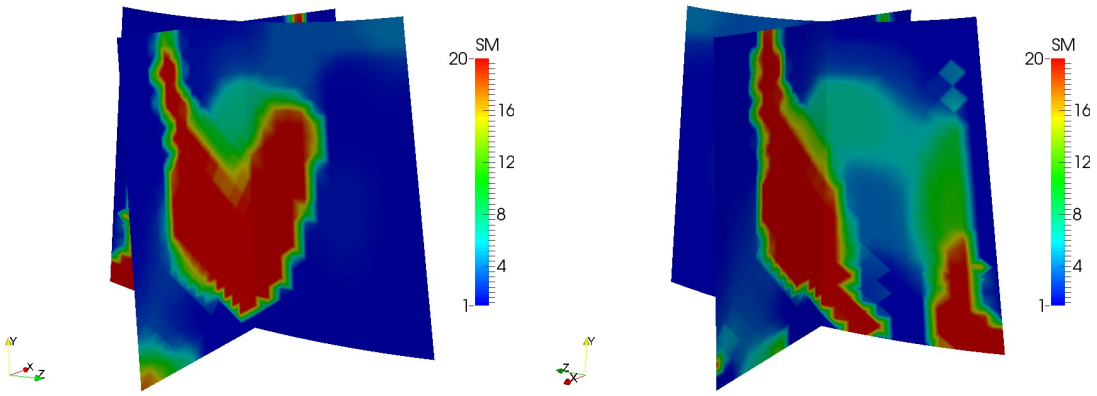

Figure 5·10: 3D phantom reconstruction obtained using assumed BCs

5.4.4 Results

The reconstruction shown in Figure (5·10) is dominated by stiff boundary artifacts. Although it was obtained using a $\boldsymbol{T}$ tensor correctly aligned with the direction of sound propagation, the assumed BCs approach is inappropriate for this data. The reason for this is u_y contains a mixture of precise and poorly characterized measurements, and thus prescribing it on the boundary yields poor results.

Spring elements were used in the reconstruction depicted in Figure (5·11). Boundary artifacts are still visible in the top of the domain, but they are significantly reduced in magnitude compared to the assumed BCs reconstruction. A spherical inclusion in a softer background is clearly visible, and its contrast is an under-estimate of the value obtained using mechanical testing, 4. The use of regularization generally leads

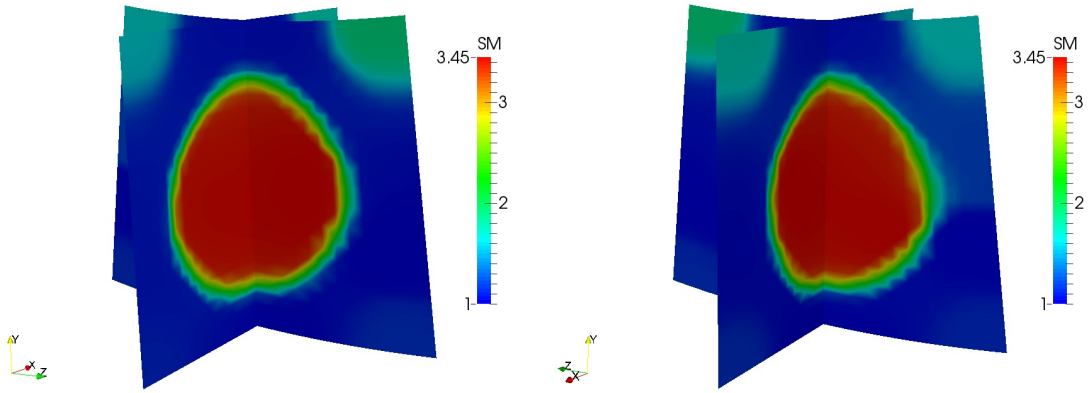

Figure 5·11: 3D phantom reconstruction obtained using spring BCs

to a bias towards lowers contrast.

Figure (5·12) shows a reconstruction obtained using the CASE approach. The $\boldsymbol{T}$ tensor was chosen to coincide with the spatially-varying axial, lateral, and elevational directions. The non-axial directions were weighted 100 times less than the axial component. This approach is also able to produce a reconstruction that is superior to the assumed BCs result. Figure (5·13) highlights the striking difference between the top layer of the springs and CASE reconstructions.

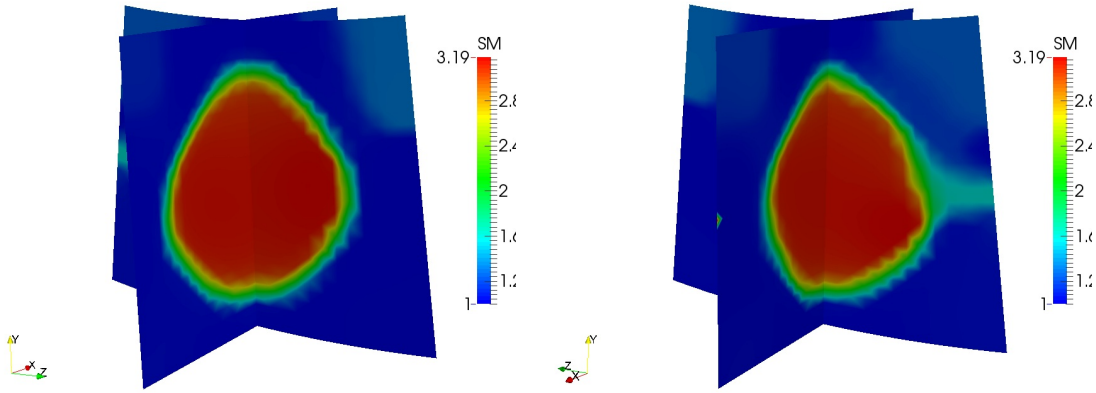

Figure 5·12: 3D phantom reconstruction obtained with the CASE approach

The panel of results in Figure (5·14) was used to determine which displacement frame was most likely to show a slip layer. These results were obtained using a

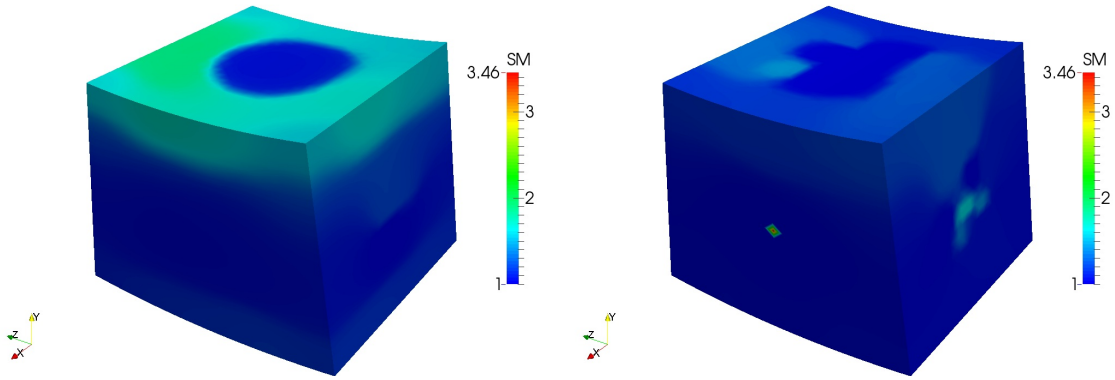

Figure 5·13: Surface view of phantom for springs and CASE reconstructions

coarse mesh (downsampled by 4 in each direction), boundary spring elements, and the optimization bounds were set far away from the initial guess of 1 (e.g $L = 0.001$, $U = 70$) to promote observation of slip layers. The Frame 4 inversion has a region of low modulus around the inclusion, so we preceded to perform an inversion at a higher resolution (no downsampling).

Slip layers were observed in the fine mesh reconstruction shown in Figure (5·15). The layers occur at specific locations along the interface, and were about two element widths across.

5.4.5 Discussion

The CASE and springs formulations were both able to produce reasonable results from this dataset, while the assumed BCs approach did not. The springs formulation reconstruction has inclusion contrast that is higher than in the CASE result, but also contains an artificially stiff layer at the top of the phantom.

The observation that a slip layer was not seen until the latest displacement frame suggests that inclusion and its background move together until the applied strain is sufficient for slipping to occur.

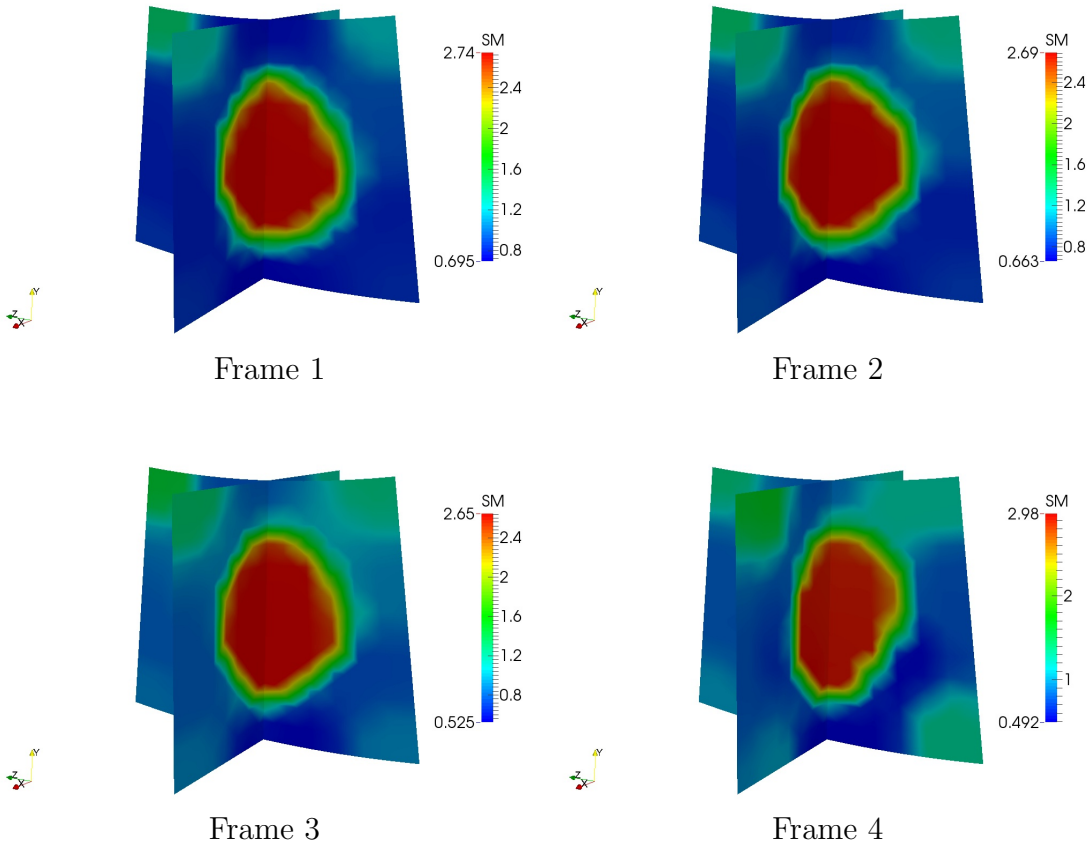

Figure 5·14: Coarse mesh slip results

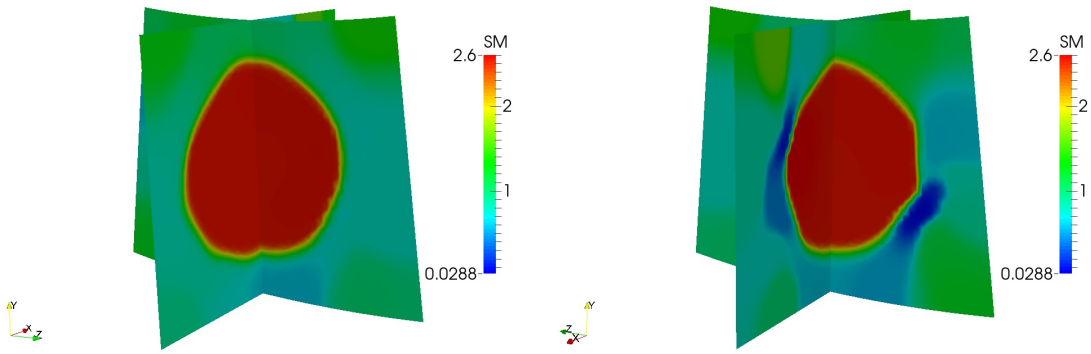

Figure 5·15: Frame 4 slip reconstruction

5.5 2D Clinical

In this section we present results from a clinical dataset that were analyzed using plane stress and plane strain CASE approaches. This dataset contains 5 fibroadenoma (FA)

and 5 invasive ductal carcinoma (IDC) breast tumors (as determined by biopsy). FAs are benign while IDCs are malignant. This data was collected and processed by Timothy Hall's group at the University of Wisconsin.

5.5.1 Experiment

The experimental protocol, acquisition of RF images, and processing of displacement data for this dataset are documented in (Goenezen et al., 2012), and are briefly summarized here.

In each experiment, several quasistatic compression load steps (each corresponding to about 1% overall strain) were imposed using an US transducer ("free-hand elastography") and RF images were acquired before/after the application of each load.

Incremental displacement fields were estimated using the block-matching algorithm described in (Jiang and Hall, 2009). We limit our attention here to the lowest level of applied strain (1%), as the CASE formulations assume small deformation.

5.5.2 Results

Results obtained from application of the plane stress CASE are shown in Figures (5·16) and (5·17). There are small regions of high stiffness present in some of the reconstructions. We present all the results on a logarithmic scale in order to compress the dynamic range and display more meaningful images that utilize the full range of the data. The regularization constant α used for each tumor is given in Table (5.3).

Table 5.3: Regularization parameter used in clinical study results

Tumor Type	1	2	3	4	5
FA	4.0e-5	3.0e-5	1.0e-5	2.0e-5	3.0e-5
IDC	4.0e-5	2.0e-5	4.0e-4	5.0e-5	3.0e-5

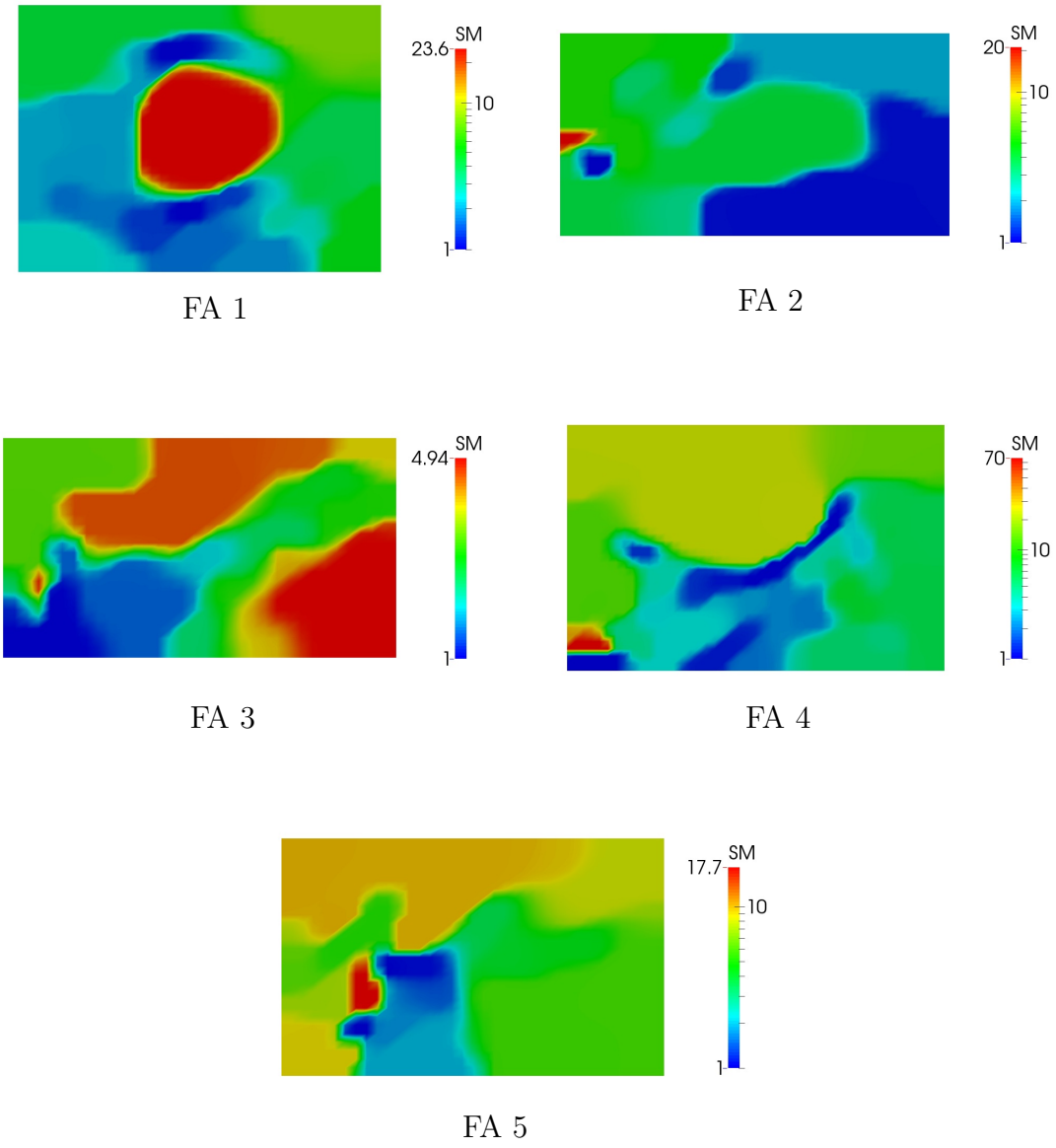

Figure 5·16: Clinical FA plane stress CASE results

The plane stress reconstructions are shown in Figures (5·16) and (5·17), and the plane strain reconstructions are displayed in Figures (5·18) and (5·19).

The entries of the $\boldsymbol{T}$ tensor used for all modulus inversions were $T_{xx} = 0.1$, $T_{xy} = 0$ $T_{yy} = 1$.

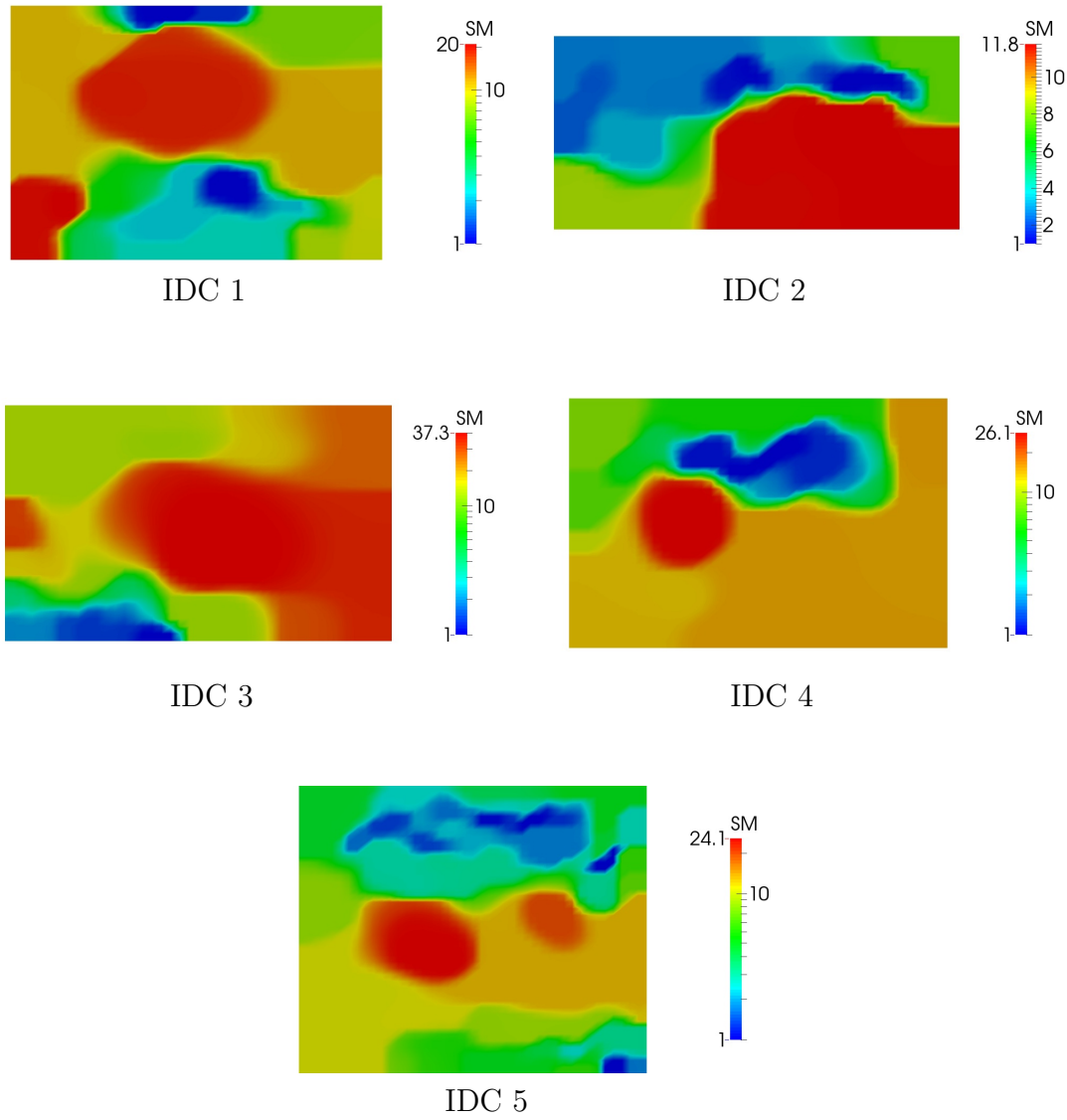

Figure 5·17: Clinical IDC plane stress CASE results

5.5.3 Discussion

First we note that although inclusions are visible in the clinical reconstructions, these images are considerably more heterogeneous than the phantom datasets presented in this chapter. Defining the border of the tumor is challenging in some cases (e.g. IDC 3).

The CASE approach assumes Gaussian measurement noise, and this assumption

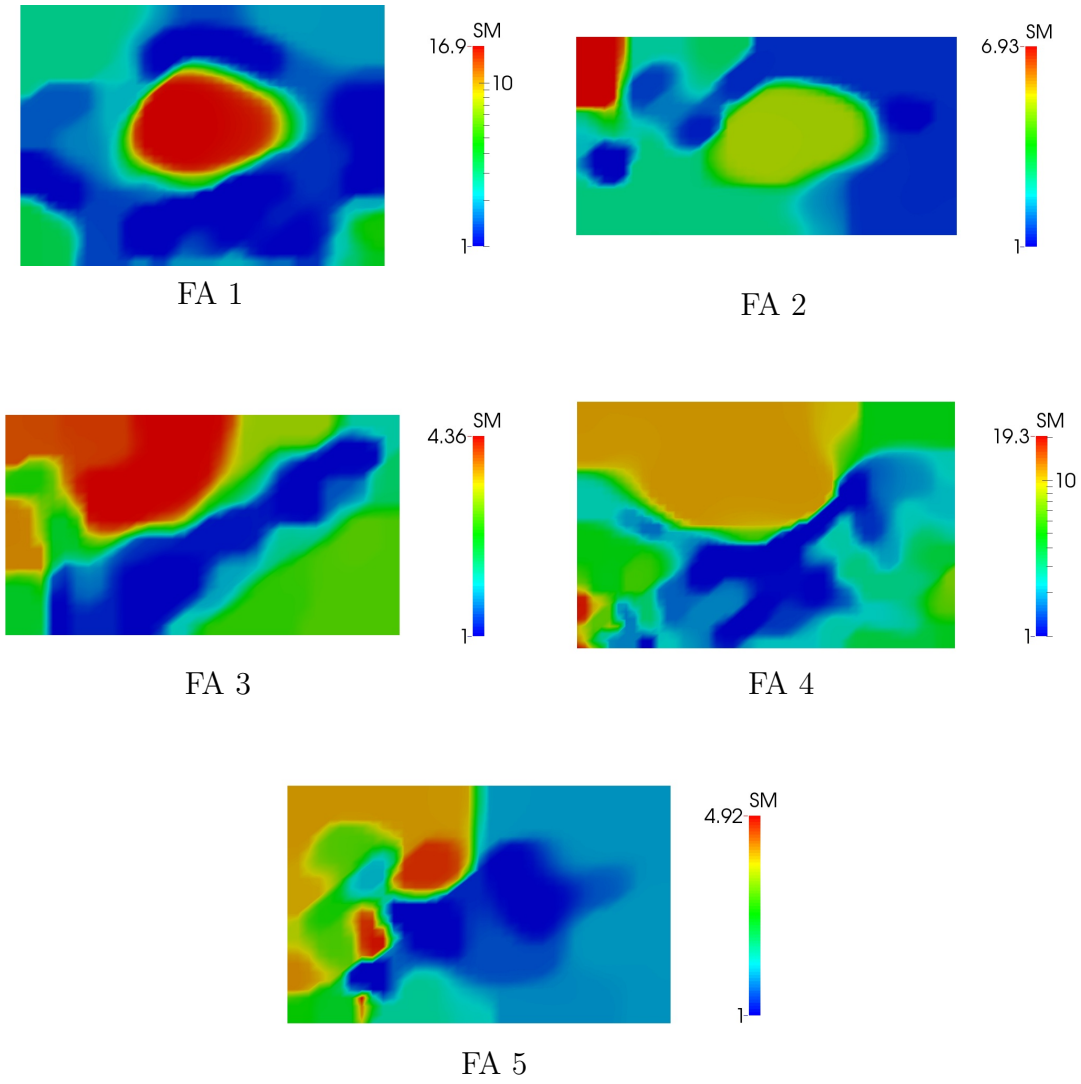

Figure 5·18: Clinical FA plane strain CASE results

is almost certainly violated (especially by the lateral displacement component) in this dataset. Localized regions of high stiffness are observed in some plane stress reconstructions (i.e. FA 2 and FA 4) and many of the IDC plane strain reconstructions, and are probably due to an incompatibility between the material model and measured data.

Fibroadenomas are known to be less bound to their surroundings than malignant breast tumors (Konofagou et al., 2000). Some, in fact, are highly mobile. The thin

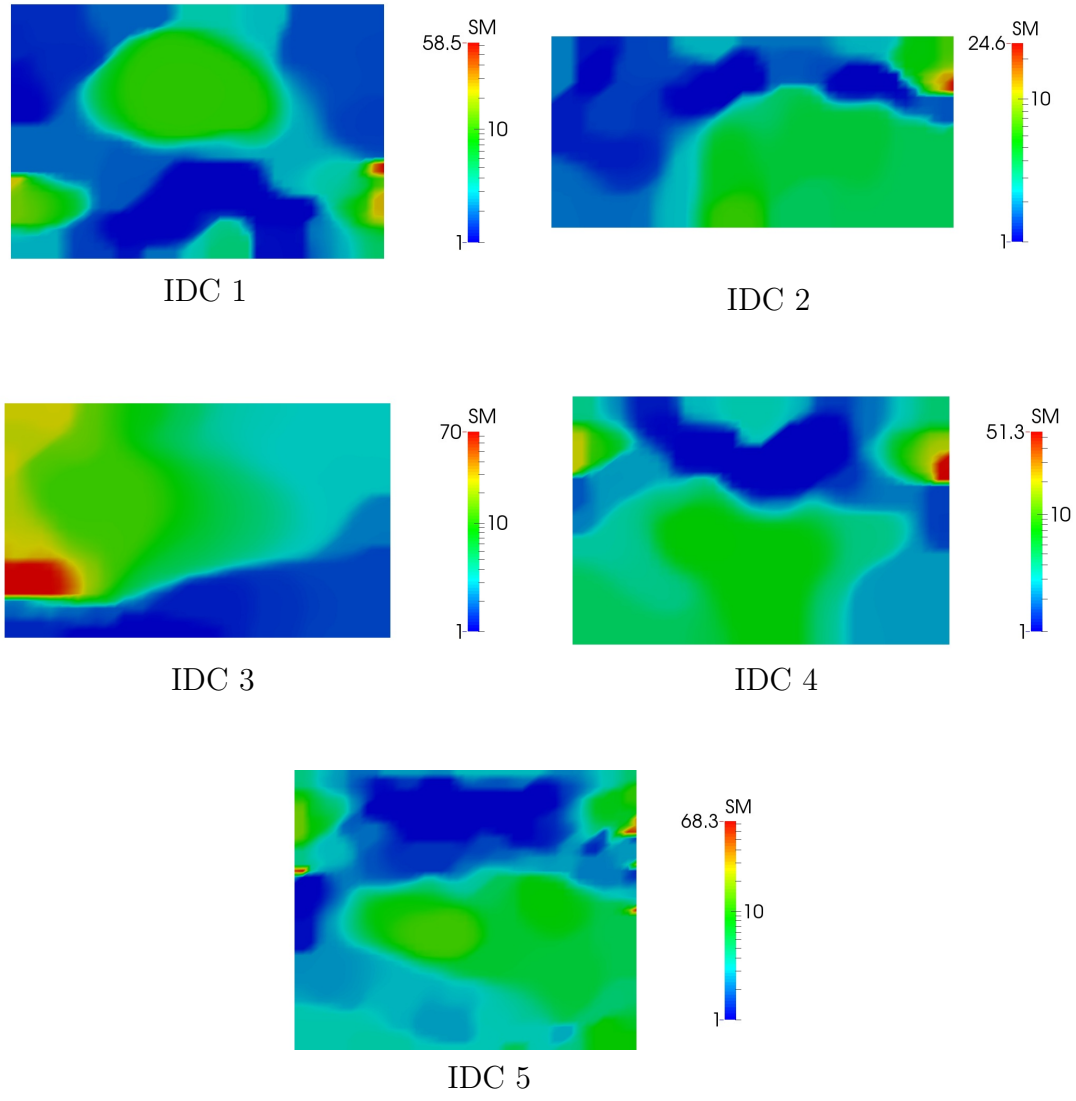

Figure 5·19: Clinical IDC plane strain CASE results

regions of low stiffness observed around the edge of the inclusions in the plane stress results for FA 1 and FA 4 could indicate slip layers around the tumor. These findings suggest that different results would be obtained by selecting optimization bounds that allow the modulus to drop to arbitrarily low values.

The plane stress and plane strain FA results look similar although tumor contrast is higher in the plane stress results. The plane strain IDC reconstructions all contain stiff boundary artifacts that are not present in the plane stress results.

Chapter 6

Discussion and Conclusion

6.1 Summary

In this thesis we used the finite element method to obtain approximate solutions of PDE-constrained optimization problems. Although our motivating application was the BMI problem, the methods discussed in this thesis are generally applicable to inverse problems constrained to satisfy an elliptic system of PDEs. We introduced a novel structure for the software implementation of the iterative inversion algorithm. We created two formulations capable of solving forward and inverse problems with uncertain BCs.

The key idea that defines the software framework is the separation of finite element implementations according to the operators that appear in the inverse problem. The application of this design philosophy can be interpreted as taking the traditional single element approach to FEM and breaking it into layers of specialized finite elements. We introduced material, forcing, data match, and regularization element layers and explained their functional roles.

The spring penalty formulation of the constraint equation was derived using a Bayesian approach to explicitly account for the presence of uncertainty in the BCs defining the forward problem. We found that the boundary springs approach produced better modulus reconstructions than the domain springs approach when applied to problems with full-field interior data. We showed how "weak" springs, a variant of the domain springs approach, can be used to constrain unknown rigid body motion

and used this approach to solve BMI problems at the cellular scale.

Finally, we introduced the CASE formulation for linear incompressible plane stress, plane strain, and 3D forward and inverse problems. The main advantage of this formulation is that it does not treat the boundary values of the displacement field differently than the interior values, and consequently avoids biasing the inverse problem solution. We introduced two approaches to stabilizing the discrete saddle point problem that we called "weak stabilization" and "strong stabilization." We found that only the strong stabilization approach was successful for all modeling situations. We applied the formulation to simulated, phantom, and clinical US BMI data and were able to produce accurate modulus reconstructions in the instances where the exact distribution was known.

6.2 Discussion

The layered finite elements concept could be used to solve inverse problems not considered in this thesis. Indeed, a similar approach has recently been described by (Walsh, 2015). In the BMI inverse problem the unknown quantity of interest is a material parameter. In other inverse problems one wishes to estimate unknown boundary conditions, body forces acting as source or sink terms, or natural frequencies. We focused on gradient-based optimization in this thesis, but this viewpoint is applicable to Newton-type optimization methods as well. Additional derivatives of the operators appear, but they could still be organized in the same manner.

An advantage of the spring penalty approach is that it is independent of the material model used in the inverse problem. Thus it can be used in inverse problems where the constraint equation is nonlinear. A disadvantage is the need to determine spring constants. They can, in principle, be found by examining the statistics of the noise. That process is easier said than done, however, and the degree to which

measurement noise can be approximated by a Gaussian distribution varies.

A BC-free approach much like the strong stabilization version of CASE has recently been developed in (Diaz et al., 2015) to solve a frequency-domain, viscoelastic inverse problem. While their formulation uses a different objective function, their motivation for developing a method of solving the inverse problem without assuming displacement or traction BCs is identical to ours as their data is collected using US image registration techniques as well.

We applied the CASE approach only to linear constraint equations in this thesis. As a result, the forward and adjoint variables could be obtained with a single linear solve. The extension of CASE to nonlinear material models will require an iterative approach.

The strong stabilization used in CASE produces fluctuations on the boundary of the predicted displacement fields that were not seen when weak stabilization was used. Although the strong approach clearly produced better inverse problem solutions and was computationally easier to implement, there is room for improvement (most likely through the use of novel stabilization terms).

Non-ultrasound based elastography (e.g. MRI) could stand to benefit from the use of a CASE-like approach. The choice of BCs to impose in the forward model, a crucial part of its definition, can be a challenging and time-consuming endeavor. Furthermore, as shown in this thesis, the accuracy of the inverse problem solution often depends strongly on this choice. The CASE formulation "automatically extracts" this component of the forward model from the measured data. This makes inverse approaches based on CASE less susceptible to operator/analyst error.

6.3 Conclusion

The software framework proposed in this thesis is suitable for application to the solution of several classes of inverse problems, and with modification could be applied to many more. We invented two formulations that account for uncertainty in the BCs of the constraint equation and applied them to a plethora of experimental data. The methods presented herein can be used to obtain inverse problem solutions superior to those obtained using the assumed BCs approach in situations where the assumptions are in conflict with the experimental conditions.

Appendix A

Incompressible Linear Elasticity

The field variables in a linear, isotropic, incompressible elasticity problem include a material parameter (the shear modulus μ), pressure (p), displacement ($\boldsymbol{u}$), strain ($\boldsymbol{\epsilon}$), and stress ($\boldsymbol{\sigma}$).The notation $\partial_j = \frac{\partial}{\partial x_j}$ is used in the following equations. The shear modulus and pressure are scalar fields, the displacement is a vector field, and the stress and strain fields are rank two symmetric tensor fields. Small deformation of soft tissue is often well approximated by a linear elastic, isotropic, incompressible material model. The incompressiblity constraint is

$$\nabla \cdot \boldsymbol{u} \;=\; \sum_k \partial_k u_k \;=\; \partial_k u_k \;=\; 0 \;,\; k = 1, 2, 3 \tag{A.1}$$

The summation convention (a repeated index in a term implies a sum over that index) has been used above, and will be used henceforth.

A.1 Plane Stress

The plane stress approximation is a simplification of the full 3D elasticity equations that can be applied to 2D displacement data. It is assumed that out of plane stresses are negligibly small, and all applied loads are within the plane. A thin material with no out of plane loadings satisfies these assumptions.

Mathematically, these assumptions lead to five of the components of the symmetric stress tensor $\boldsymbol{\sigma}$ being equal to zero. Let $\hat{\boldsymbol{e}}_i \;,\; i = 1, 2, 3$ denote the standard Cartesian

basis for $\mathbb{R}^3$ and $\hat{\boldsymbol{e}}_1$ and $\hat{\boldsymbol{e}}_2$ be the in-plane basis vectors. By assumption, all of the $\hat{\boldsymbol{e}}_3$ components of the stress tensor $(\sigma_{33}, \sigma_{13}, \sigma_{31}, \sigma_{23}, \sigma_{32})$ are zero, and therefore drop out of the equilibrium equations. Those zero stress components also lead to the conclusion that $\epsilon_{13} = \epsilon_{31} = \epsilon_{23} = \epsilon_{32} = 0$ is satisfied. In generalized plane stress, the field variables are averaged through the thickness to produce a truly planar problem. It is important to note that ϵ_{33} is non-zero. However, all of the strains are independent of x_3 so it is acceptable to consider the field variables as functions of their position in the plane. The constitutive equation for a linear elastic, isotropic, incompressible material $(i, j = 1, 2, 3)$ is

$$\begin{aligned} \boldsymbol{\sigma} &= -p\boldsymbol{I} + 2\mu\boldsymbol{\epsilon} \\ \sigma_{ij} &= -p\delta_{ij} + 2\mu\epsilon_{ij} \end{aligned} \tag{A.2}$$

The strain-displacement relation is

$$\begin{aligned} \boldsymbol{\epsilon} &= \nabla^s \boldsymbol{u} \equiv \frac{1}{2}(\nabla \boldsymbol{u} + \nabla \boldsymbol{u}^T) \\ \epsilon_{ij} &= \frac{1}{2}(\partial_i u_j + \partial_j u_i) \end{aligned} \tag{A.3}$$

From (A.1), (A.3), and $\sigma_{33} = 0$ $(\alpha, \beta, \gamma = 1, 2)$

$$\epsilon_{kk} = 0 : \qquad \epsilon_{\gamma\gamma} = -\epsilon_{33} \tag{A.4}$$

$$(A.3) : \qquad \sigma_{33} = -p + 2\mu\epsilon_{33} = 0 \tag{A.5}$$

$$(A.4, A.5) : \qquad p = 2\mu\epsilon_{33} = -2\mu\epsilon_{\gamma\gamma} \tag{A.6}$$

$$(A.3, A.6) : \qquad \sigma_{\alpha\beta} = 2\mu\epsilon_{\gamma\gamma}\delta_{\alpha\beta} + 2\mu\epsilon_{\alpha\beta} \tag{A.7}$$

Greek indices α, β, and γ are written to emphasize that the problem is now planar.

A convenient strain measure in applications of incompressible is $\boldsymbol{A}(\boldsymbol{u})$, defined so that

$$\begin{aligned} \sigma_{\alpha\beta} &\equiv 2\mu(\delta_{\alpha\beta}\epsilon_{\gamma\gamma} + \epsilon_{\alpha\beta}) \\ &= \mu(2\delta_{\alpha\beta}\partial_\gamma u_\gamma + \partial_\alpha u_\beta + \partial_\beta u_\alpha) \\ &\equiv \mu A_{\alpha\beta} \\ \text{i.e.} \qquad A_{\alpha\beta} &= (2\delta_{\alpha\beta}\partial_\gamma u_\gamma + \partial_\alpha u_\beta + \partial_\beta u_\alpha) \end{aligned} \tag{A.8}$$

In symbolic form

$$\begin{aligned} \boldsymbol{\sigma} &= 2\mu \mathrm{Tr}(\boldsymbol{\epsilon})\boldsymbol{I} + 2\mu\boldsymbol{\epsilon} \\ \boldsymbol{\sigma} &= 2\mu(\nabla \cdot \boldsymbol{u}) + \mu(\nabla\boldsymbol{u} + \nabla\boldsymbol{u}^T) \\ \boldsymbol{\sigma} &= \mu\boldsymbol{A}(\boldsymbol{u}) \end{aligned} \tag{A.9}$$

Finally, the traction vector $\boldsymbol{t}$ is defined to be ($\boldsymbol{n}$ is a unit vector that points in an outward direction normal to a given surface)

$$\begin{aligned} \boldsymbol{t} &= \boldsymbol{\sigma} \cdot \boldsymbol{n} \\ t_\alpha &= \sigma_{\alpha\beta} n_\beta \end{aligned} \tag{A.10}$$

The forward elasticity problem yields a displacement field given a modulus field and a combination of traction and displacement BCs. The principle of minimum potential energy states that of all displacement fields that satisfy the essential (displacement) BCs, the solution is that which minimizes the system's potential energy functional:

$$\begin{aligned} \pi^f[\boldsymbol{u}] &= \frac{1}{2}\int_\Omega \boldsymbol{\sigma}[\boldsymbol{u}] : \boldsymbol{\epsilon}[\boldsymbol{u}]\ d\Omega \ - \int_{\Gamma_t} \boldsymbol{u}\cdot\boldsymbol{t}\ d\Gamma \ - \int_\Omega \boldsymbol{u}\cdot\boldsymbol{b}\ d\Omega \\ &= \frac{1}{2}(\boldsymbol{\sigma}[\boldsymbol{u}], \boldsymbol{\epsilon}[\boldsymbol{u}])_\Omega \ - \ (\boldsymbol{u}, \boldsymbol{t})_{\Gamma_t} - (\boldsymbol{u}, \boldsymbol{b})_\Omega \end{aligned} \tag{A.11}$$

The last line above highlights the fact that these integrals are inner products over the domain Ω and the portion of the boundary with traction BCs Γ_t. Γ_u denotes the portion of the boundary with Dirichlet BCs g_i. (For simplicity of presentation, we assume $\Gamma_{g_1} = \Gamma_{g_2} \equiv \Gamma_u$ and $\Gamma = \partial\Omega = \overline{\Gamma_u \cup \Gamma_t}$; $\Gamma_u \cap \Gamma_t = \emptyset$) In plane stress, Ω is a two-dimensional region and Γ is one-dimensional.

The first term in the functional represents the strain energy of the material, while the other terms represent the work done by tractions and body forces, respectively. The double dot product used above is defined as

$$\boldsymbol{\sigma} : \boldsymbol{\epsilon} = \mathrm{Tr}(\boldsymbol{\sigma}\boldsymbol{\epsilon}^T) = \sigma_{\alpha\beta}\epsilon_{\alpha\beta} \tag{A.12}$$

The appropriate function spaces in which to formulate this problem are those for which (A.11) is finite. They are subspaces of $H^1(\Omega)$, chosen such that the field $\boldsymbol{u} + \alpha\boldsymbol{w}, \alpha \in \mathbb{R}$ satisfies the essential BCs.

$$\boldsymbol{u} \in \mathcal{S} \equiv \{\boldsymbol{u} \mid u_i \in H^1(\Omega), u_i = g_i \text{ on } \Gamma_u\} \tag{A.13}$$

$$\boldsymbol{w} \in \mathcal{V} \equiv \{\boldsymbol{w} \mid w_i \in H^1(\Omega), w_i = 0 \text{ on } \Gamma_u\} \tag{A.14}$$

The weak form of the elasticity equations is obtained by setting the Gâteaux derivative of (A.11) to zero.

$$D_{\boldsymbol{u}}\pi^f \cdot \boldsymbol{w} = \frac{d}{d\alpha}\pi^f[\boldsymbol{u} + \alpha\boldsymbol{w}]\Big|_{\alpha=0} \overset{set}{=} 0 \;\forall\; \boldsymbol{w} \in \mathcal{V} \tag{A.15}$$

$$D_{\boldsymbol{u}}\pi^f \cdot \boldsymbol{w} = \int_\Omega \nabla\boldsymbol{w} : \mu\boldsymbol{A}(\boldsymbol{u})\; d\Omega - \int_{\Gamma_t} \boldsymbol{w}\cdot\boldsymbol{t}\; d\Gamma - \int_\Omega \boldsymbol{w}\cdot\boldsymbol{b}\; d\Omega \tag{A.16}$$

Equation (A.16) can be used to define the specific linear and bilinear operators in an abstract weak BVP (A.17).

$$a(\boldsymbol{w}, \boldsymbol{u}; \mu) = l(\boldsymbol{w}) \ \forall \ \boldsymbol{w} \in \mathcal{V} \tag{A.17}$$

$$a(\boldsymbol{w}, \boldsymbol{u}; \mu) = \int_{\Omega} \nabla \boldsymbol{w} : \mu \boldsymbol{A}(\boldsymbol{u}) \ d\Omega \tag{A.18}$$

$$l(\boldsymbol{w}) = \int_{\Gamma_t} \boldsymbol{w} \cdot \boldsymbol{t} \ d\Gamma + \int_{\Omega} \boldsymbol{w} \cdot \boldsymbol{b} \ d\Omega \tag{A.19}$$

Integrating (A.17) by parts and accounting for the essential boundary conditions produces the strong form (A.20) - (A.22) of the BVP. The strong form is called so because it contains second order derivatives of the displacement and must be satisfied pointwise in the domain, while the highest order derivatives present in the weak form (A.17) are first order and the equations are satisfied only in an integral sense.

$$\nabla \cdot (\mu \boldsymbol{A}(\boldsymbol{u})) + \boldsymbol{b} = \boldsymbol{0}, \ \boldsymbol{x} \in \Omega \tag{A.20}$$

$$\boldsymbol{\sigma} \cdot \boldsymbol{n} = \boldsymbol{t}, \ \boldsymbol{x} \in \Gamma_t \tag{A.21}$$

$$\boldsymbol{u} = \boldsymbol{g}, \ \boldsymbol{x} \in \Gamma_u \tag{A.22}$$

We have shown that the displacement field may be obtained in three distinct but equivalent ways: As the solution of the strong form (A.20)-(A.22), the weak form (A.17)-(A.19), or as the minimizer of the functional (A.11).

A.2 Plane Strain and 3D

In incompressible plane strain and 3D the pressure term cannot be eliminated as was done in plane stress, and must be solved for along with the displacement field. The plane strain assumption approximates materials that are confined in the out of plane direction and have loadings that do not vary along that direction. The governing

equations for both plane strain and 3D are identical except for the range of indices: 1-2 for plane strain and 1-3 for 3D.

The constitutive and strain-displacement relations are

$$\boldsymbol{\sigma} = -p\boldsymbol{I} + 2\mu\boldsymbol{\epsilon} \tag{A.23}$$

$$\boldsymbol{\epsilon} = \nabla^s \boldsymbol{u} \equiv \frac{1}{2}(\nabla \boldsymbol{u} + \nabla \boldsymbol{u}^T) \tag{A.24}$$

The strong form of this BVP includes the equilibrium equation along with its BCs and the incompressibility condition:

$$\nabla \cdot \boldsymbol{\sigma} + \boldsymbol{b} = \boldsymbol{0},\ \boldsymbol{x} \in \Omega \tag{A.25}$$

$$\nabla \cdot \boldsymbol{u} = 0,\ \boldsymbol{x} \in \Omega \tag{A.26}$$

$$\boldsymbol{\sigma} \cdot \boldsymbol{n} = \boldsymbol{t},\ \boldsymbol{x} \in \Gamma_t \tag{A.27}$$

$$\boldsymbol{u} = \boldsymbol{g},\ \boldsymbol{x} \in \Gamma_u \tag{A.28}$$

The function spaces for the solution variables are defined below. If $\Gamma_u = \Gamma$ (a pure Dirichlet problem), the pressure field and its variation are unique up to a constant.

$$\boldsymbol{u} \in \mathcal{S} \equiv \{\boldsymbol{u} \mid u_i \in H^1(\Omega), u_i = g_i \text{ on } \Gamma_u\} \tag{A.29}$$

$$\boldsymbol{w} \in \mathcal{V} \equiv \{\boldsymbol{w} \mid w_i \in H^1(\Omega), w_i = 0 \text{ on } \Gamma_u\} \tag{A.30}$$

$$p, q \in \mathcal{P} \subseteq L^2(\Omega) \tag{A.31}$$

The weak form is obtained in two steps. First, equation (A.25) is multiplied by a test function $-\boldsymbol{w} \in \mathcal{V}$ and integrated by parts. Application of the BC (A.27) and the vanishing of $\boldsymbol{w}$ on Γ_u yields the first piece. Second, equation (A.26) is multiplied by a test function $-q \in \mathcal{P}$. The abstract variational problem is

$$a(\boldsymbol{w}, \boldsymbol{u}; \mu) + b(p, \boldsymbol{w}) = l(\boldsymbol{w}) \ \forall \ \boldsymbol{w} \in \mathcal{V} \tag{A.32}$$

$$b(q, \boldsymbol{u}) = 0 \ \forall \ q \in \mathcal{P} \tag{A.33}$$

where

$$a(\boldsymbol{w}, \boldsymbol{u}; \mu) = \int_{\Omega} \nabla \boldsymbol{w} : 2\mu \nabla^s \boldsymbol{u} \ d\Omega \tag{A.34}$$

$$l(\boldsymbol{w}) = \int_{\Gamma_t} \boldsymbol{w} \cdot \boldsymbol{t} \ d\Gamma + \int_{\Omega} \boldsymbol{w} \cdot \boldsymbol{b} \ d\Omega \tag{A.35}$$

$$b(q, \boldsymbol{u}) = -\int_{\Omega} q \nabla \cdot \boldsymbol{u} \ d\Omega \tag{A.36}$$

The system represented by (A.32) and (A.33) is an example of a saddle point problem (Strang, 2007). The q variable acts as a Lagrange multiplier for the incompressibility constraint. The inf-sup condition (Johnson, 2012) provides a means of determining whether this variational problem is well-posed.

Appendix B

Simulated Examples

The results presented in this appendix serve two purposes. First, they highlight the sensitivity of the inverse problem to assumed BCs in two modeling contexts. Second, they serve as references to be compared to results obtained using the formulations proposed in Chapters 3 and 4.

B.1 Simulated Data Generation

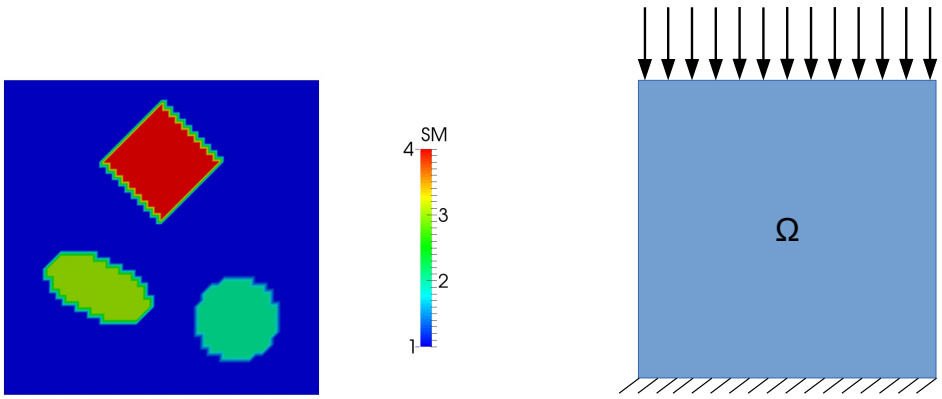

Figure B·1: 2D simulated experiment

The examples in this section are motivated by BMI quasi-static compression experiments. The normalized 2D shear modulus distribution and applied loading are shown in Figure (B·1). The normalized shear moduli of the diamond, ellipse, and circle-shaped inclusions are 4, 3, and 2, respectively, and the value of the background is normalized to 1. The size of the domain is 50×50 units.

The loading was designed to loosely emulate conditions encountered in ultrasound elasticity imaging. A constant downward displacement of 0.5 units (corresponding to about 1% axial compressive strain) is applied at the top of the domain and the bottom is "stuck", i.e. both components of the displacement field are fixed to zero. The sides of the domain are free to expand. In breast elasticity imaging, the ultrasound transducer compresses the tissue, and the chest wall prevents displacement at a greater depth.

Noiseless displacement fields were obtained by solving a forward problem using the described loading and reference shear modulus distribution as the input to incompressible linear plane stress and plane strain finite element models. These displacement fields can then be used as input data to the inverse problem. Inversion algorithms tend to perform unrealistically well (i.e. commit an "inverse crime"), however, when the same discrete model that was used to generate the data is used to solve the inverse problem. We avoid committing an inverse crime by corrupting the displacements with noise.

Additive, independent Gaussian noise $n_i(\boldsymbol{x})$ was added to each displacement component to create simulated "measured" displacement fields $\boldsymbol{u}^m(\boldsymbol{x})$ for the inverse problem. To simulate what is encountered in ultrasound elasticity imaging, 2% noise was added to the y component while 10% noise was added to the x component, as the lateral displacements are often considerably more uncertain than the axial. The formula for % noise is given by equation (B.2).

$$u_i^m(\boldsymbol{x}) = u_i(\boldsymbol{x}) + n_i(\boldsymbol{x}) \ , \ i = 1, 2 \tag{B.1}$$

$$\%\text{ noise} = \sqrt{\frac{\int_\Omega n_i^2 \ d\Omega}{\int_\Omega u_i^2 \ d\Omega}} \times 100 \ , \ i = 1, 2 \tag{B.2}$$

The simulated measured displacement fields for the plane stress and plane strain

example problems are shown in Figures (B·2) and (B·3) The stiffest, diamond-shaped inclusion is visible in the u_y displacement field.

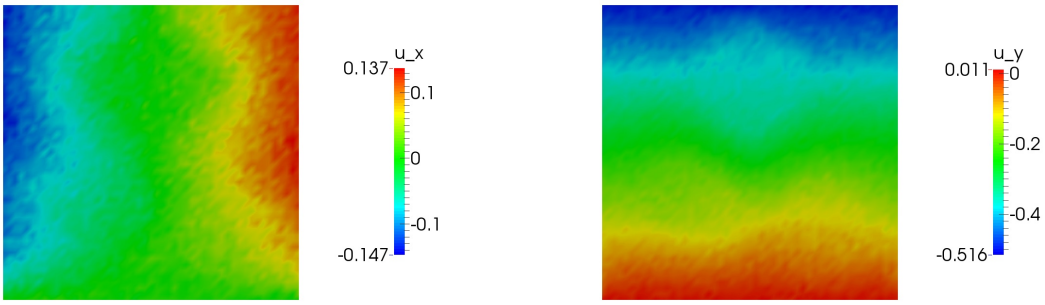

Figure B·2: Plane stress simulation measured displacement fields

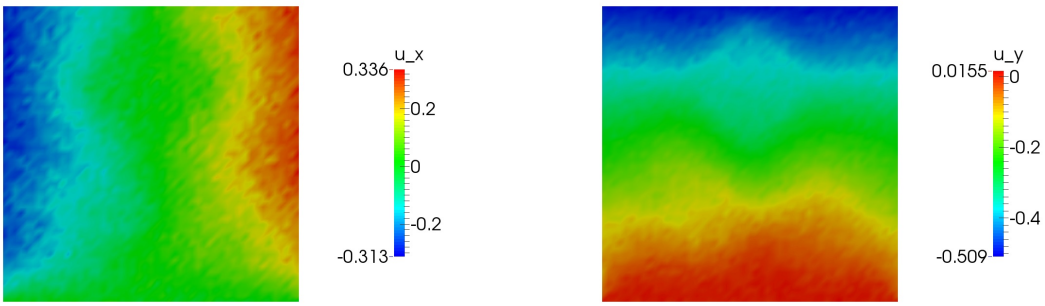

Figure B·3: Plane strain simulation measured displacement fields

B.2 Inverse Problem Formulation

- General Inverse Problem Statement: Given $\boldsymbol{u}^m(\boldsymbol{x})$, $\boldsymbol{x} \in \Omega$, find $\mu(\boldsymbol{x})$ that minimizes

$$\begin{aligned} \pi[\mu] &= \mathcal{D}[\boldsymbol{u}(\mu(\boldsymbol{x})) - \boldsymbol{u}^m] + \alpha \mathcal{R}[\mu(\boldsymbol{x})] \\ \text{s.t.} \quad & \mathcal{A}(\boldsymbol{w}, \boldsymbol{u}; \mu) = l(\boldsymbol{w}) \; \forall \; \boldsymbol{w} \in \mathcal{V} \\ & L \leq \mu \leq U \end{aligned} \tag{B.3}$$

$$\boldsymbol{u} \in \mathcal{S} \equiv \{\boldsymbol{u} \mid u_i \in H^1(\Omega), u_i = g_i \text{ on } \Gamma_u\} \tag{B.4}$$

$$\boldsymbol{w} \in \mathcal{V} \equiv \{\boldsymbol{w} \mid w_i \in H^1(\Omega), w_i = 0 \text{ on } \Gamma_u\} \tag{B.5}$$

$$\mu \in \mathcal{M} \equiv L^\infty(\Omega) \tag{B.6}$$

We now introduce the specific forms of the terms in (B.3) for the simulated example problems. We choose to use a least squares type $\mathcal{D}$ weighted by a symmetric, positive semi-definite tensor $\boldsymbol{T}$ to account for the difference in precision of the measured displacement components. The use of TV regularization for $\mathcal{R}$ biases the reconstructed modulus toward piecewise constant. The loading enters this inverse problem solely through the function space definitions for $\boldsymbol{u}$ (and $\boldsymbol{w}$) via $\boldsymbol{g}$, as $\boldsymbol{b}$ and $\boldsymbol{t}$ are zero. The optimization bounds are $L = 1$ (the value of the background) and $U = 20$.

$$\mathcal{D}[\boldsymbol{u} - \boldsymbol{u}^m] = \frac{1}{2}\int_\Omega \boldsymbol{T}(\boldsymbol{u} - \boldsymbol{u}^m) \cdot \boldsymbol{T}(\boldsymbol{u} - \boldsymbol{u}^m)\, d\Omega \tag{B.7}$$

$$\mathcal{R}[\mu] = \alpha \int_\Omega \sqrt{(\nabla\mu)^2 + \beta^2}\, d\Omega \tag{B.8}$$

$$l(\boldsymbol{w}) = \int_{\Gamma_t} \boldsymbol{w} \cdot \boldsymbol{t}\, d\Gamma + \int_\Omega \boldsymbol{w} \cdot \boldsymbol{b}\, d\Omega \quad (= \boldsymbol{0}) \tag{B.9}$$

The only term in (B.3) that is model dependent is the $\mathcal{A}(\cdot,\cdot)$ operator. Its definition for plane stress and plane strain can be found in Appendix A. The plane strain inverse problem contains additional unknowns p and q that we have omitted from the problem statement for simplicity of presentation.

Only the u_y component of displacement was included in the inverse problem objective function, in correspondence to what is commonly done in practice with ultrasound

elasticity imaging data, resulting in the $\boldsymbol{T}$ tensor given by (B.10). For all simulations, the regularization constant α was 8.5E-5 and TV offset constant β was set to 1.0E-3 (μ and h are $O(1)$).

$$T_{ij} = \begin{bmatrix} 0 & 0 \\ 0 & 1 \end{bmatrix} \tag{B.10}$$

We present two modulus reconstructions for each modeling scenario, the difference between them being the BCs used in the forward problem. First, as a reference solution, the BCs used to generate the noiseless displacement field were applied (perfect BCs). This reconstruction represents the "best" solution one could hope to find. Second, a choice of boundary conditions commonly assumed in practice was used (assumed BCs); namely we imposed the y component of the measured displacement field $u_y^m(\boldsymbol{x})$ as a Dirichlet boundary condition, while the remaining x direction BC was assumed to be homogeneous Neumann (i.e. traction-free).

B.3 Plane Stress Results

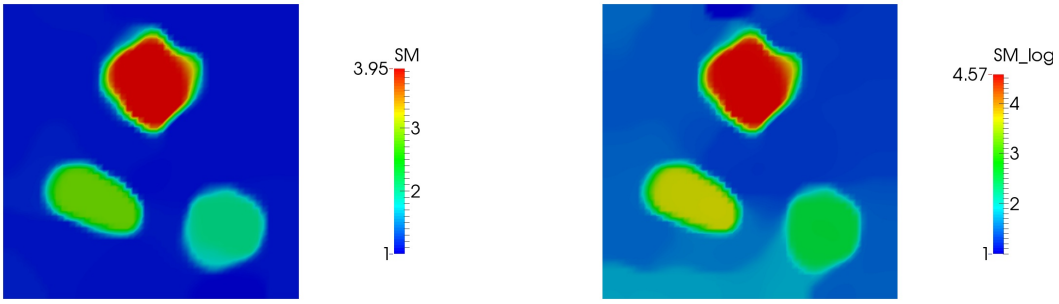

Perfect BCs Assumed BCs

Figure B·4: Plane stress simulation reconstructions

The plane stress assumed BCs result resembles the perfect BCs reconstruction. The background, however, is heterogeneous and too high near the bottom of the domain. The contrast between the inclusions and the background is further from

that of the exact solution's as well.

B.4 Plane Strain Results

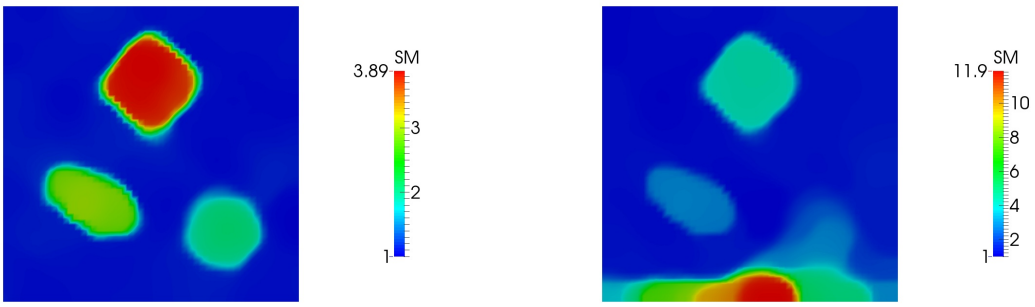

Perfect BCs Assumed BCs

Figure B·5: Plane strain simulation reconstructions

The plane strain (and 3D) inverse problem exhibits a greater sensitivity to assumed boundary conditions than plane stress. An artificially stiff (almost three times stiffer than the diamond inclusion) is present at the bottom of the domain due to an incompatibility between the assumed BCs, measured displacement, and pressure term in the plane strain model.

References

Albocher, U., Oberai, A. A., Barbone, P. E., and Harari, I. (2009). Adjoint-weighted equation for inverse problems of incompressible plane-stress elasticity. *Computer Methods in Applied Mechanics and Engineering*, 198(30):2412–2420.

Barr, R. G. (2015). *Breast Elastography*. Thieme.

Barr, R. G., Destounis, S., Lackey, L. B., Svensson, W. E., Balleyguier, C., and Smith, C. (2012). Evaluation of breast lesions using sonographic elasticity imaging a multicenter trial. *Journal of Ultrasound in Medicine*, 31(2):281–287.

Berry, G. P., Bamber, J. C., Armstrong, C. G., Miller, N. R., and Barbone, P. E. (2006). Towards an acoustic model-based poroelastic imaging method: I. theoretical foundation. *Ultrasound in Medicine & Biology*, 32(4):547–567.

Bonnet, M. and Aquino, W. (2015). Three-dimensional transient elastodynamic inversion using an error in constitutive relation functional. *Inverse Problems*, 31(3):035010.

Burnside, E. S., Hall, T. J., Sommer, A. M., Hesley, G. K., Sisney, G. A., Svensson, W. E., Fine, J. P., Jiang, J., and Hangiandreou, N. J. (2007). Differentiating benign from malignant solid breast masses with us strain imaging. *Radiology*, 245(2):401–410.

Byrd, R. H., Lu, P., Nocedal, J., and Zhu, C. (1995). A limited memory algorithm for bound constrained optimization. *SIAM Journal on Scientific and Statistical Computing*, 16(5):1190–1208.

Canović, E. P., Seidl, D. T., Barbone, P. E., Smith, M. L., and Stamenović, D. (2014a). Stiffness versus prestress relationship at subcellular length scale. *Journal of Biomechanics*, 47(12):3222–3225.

Canović, E. P., Seidl, D. T., Polio, S. R., Oberai, A. A., Barbone, P. E., Stamenović, D., and Smith, M. L. (2014b). Biomechanical imaging of cell stiffness and prestress with subcellular resolution. *Biomechanics and Modeling in Mechanobiology*, 13(3):665–678.

Chakraborty, A., Bamber, J. C., and Dorward, N. L. (2012). Slip elastography: a novel method for visualising and characterizing adherence between two surfaces in contact. *Ultrasonics*, 52(3):364–376.

Diaz, M. I., Aquino, W., and Bonnet, M. (2015). A modified error in constitutive equation approach for frequency-domain viscoelasticity imaging using interior data. Submitted for publication, 2015.

Dord, J., Goenezen, S., Oberai, A., Barbone, P., Jiang, J., Hall, T., and Pavan, T. (2015). Linear and nonlinear elastic imaging: a tissue-phantom study. Submitted for publication, 2015.

Garcia, L. J., Uff, C., Fromageau, J., and Bamber, J. C. (2009). On the imaging of slip boundaries using 3d elastography. In *IEEE International Ultrasonics Symposium*, pages 2426–2428. IEEE.

Goenezen, S., Barbone, P., and Oberai, A. A. (2011). Solution of the nonlinear elasticity imaging inverse problem: The incompressible case. *Computer Methods in Applied Mechanics and Engineering*, 200(13):1406–1420.

Goenezen, S., Dord, J.-F., Sink, Z., Barbone, P. E., Jiang, J., Hall, T. J., and Oberai, A. A. (2012). Linear and nonlinear elastic modulus imaging: an application to breast cancer diagnosis. *IEEE Transactions on Medical Imaging*, 31(8):1628–1637.

Hadamard, J. (1902). Sur les problèmes aux dérivées partielles et leur signification physique. *Princeton University Bulletin*, 13(49-52):28.

Housden, R. J., Gee, A. H., Treece, G. M., and Prager, R. W. (2010). 3-d ultrasonic strain imaging using freehand scanning and a mechanically-swept probe. *IEEE Transactions on Ultrasonics, Ferroelectrics, and Frequency Control*, 57(2):501.

Hughes, T. J., Franca, L. P., and Balestra, M. (1986). A new finite element formulation for computational fluid dynamics: V. circumventing the babu***v***ska-brezzi condition: A stable petrov-galerkin formulation of the stokes problem accommodating equal-order interpolations. *Computer Methods in Applied Mechanics and Engineering*, 59(1):85–99.

Jiang, J. and Hall, T. J. (2009). A generalized speckle tracking algorithm for ultrasonic strain imaging using dynamic programming. *Ultrasound in Medicine & Biology*, 35(11):1863–1879.

Jiang, J. and Hall, T. J. (2011). A fast hybrid algorithm combining regularized motion tracking and predictive search for reducing the occurrence of large displacement errors. *IEEE Transactions on Ultrasonics, Ferroelectrics, and Frequency Control*, 58(4):730–736.

Johnson, C. (2012). *Numerical Solution of Partial Differential Equations by the Finite Element Method*. Courier Corporation.

Konofagou, E. E., Harrigan, T., and Ophir, J. (2000). Shear strain estimation and lesion mobility assessment in elastography. *Ultrasonics*, 38(1):400–404.

Nocedal, J. and Wright, S. (2006). *Numerical Optimization*. Springer Science & Business Media.

Oberai, A. A., Gokhale, N. H., Doyley, M. M., and Bamber, J. C. (2004). Evaluation of the adjoint equation based algorithm for elasticity imaging. *Physics in Medicine and Biology*, 49(13):2955.

Oberai, A. A., Gokhale, N. H., and Feijo, G. R. (2003). Solution of inverse problems in elasticity imaging using the adjoint method. *Inverse Problems*, 19(2):297.

Oberai, A. A., Gokhale, N. H., Goenezen, S., Barbone, P. E., Hall, T. J., Sommer, A. M., and Jiang, J. (2009). Linear and nonlinear elasticity imaging of soft tissue in vivo: demonstration of feasibility. *Physics in Medicine and Biology*, 54(5):1191.

Ophir, J., Cspedes, I., Ponnekanti, H., Yazdi, Y., and Li, X. (1991). Elastography: A quantitative method for imaging the elasticity of biological tissues. *Ultrasonic Imaging*, 13(2):111 – 134.

Pavan, T. Z., Madsen, E. L., Frank, G. R., Jiang, J., Carneiro, A. A., and Hall, T. J. (2012). A nonlinear elasticity phantom containing spherical inclusions. *Physics in Medicine and Biology*, 57(15):4787.

Persson, P.-O. and Strang, G. (2004). A simple mesh generator in matlab. *SIAM Review*, 46(2):329–345.

Richards, M. (2007). *Quantitative Three Dimensional Elasticity Imaging*. Ph.D. Dissertation, Boston University.

Shore, S. W., Barbone, P. E., Oberai, A. A., and Morgan, E. F. (2011). Transversely isotropic elasticity imaging of cancellous bone. *Journal of Biomechanical Engineering*, 133(6):061002.

Strang, G. (2007). *Computational Science and Engineering*. Wellesley-Cambridge Press Wellesley.

Suresh, S. (2007). Biomechanics and biophysics of cancer cells. *Acta Materialia*, 55(12):3989 – 4014.

Tarantola, A. (2002). *Inverse Problem Theory: Methods for Data Fitting and Model Parameter Estimation*. Elsevier Science.

Vogel, C. R. (2002). *Computational Methods for Inverse Problems*, volume 23. Philadelphia: Society for Industrial and Applied Mathematics.

Walsh, T. (2015). An operator-based framework for inverse problems. 13th United States National Congress on Computational Mechanics.

CURRICULUM VITAE